The influence of dopant distribution on the optoelectronic properties of tin-doped indium oxide nanocrystals and nanocrystal films

By

Sebastien Dahmane Lounis

A dissertation submitted in partial satisfaction of the

Requirements for the degree of

Doctor of Philosophy

in

Engineering - Applied Science & Technology

in the

Graduate Division

of the

University of California, Berkeley

Committee in charge:

Professor Ali Javey, Chair
Professor Oscar Dubon
Professor Tanja Cuk
Professor Delia Milliron, University of Texas, Austin (Research Adviser)

Fall 2014

UMI Number: 3686398

UMI

Dissertation Publishing

UMI 3686398

ProQuest®

Abstract

The Influence of Radial Dopant Distribution on the Optoelectronic Properties of Tin-Doped Indium Oxide Nanocrystals

By Sebastien D. Lounis

Doctor of Philosophy in Applied Science and Technology

University of California, Berkeley

Professor Ali Javey, Chair

Colloidally prepared nanocrystals of transparent conducting oxide (TCO) semiconductors have emerged in the past decade as an exciting new class of plasmonic materials. In recent years, there has been tremendous progress in developing synthetic methods for the growth of these nanocrystals, basic characterization of their properties, and their successful integration into optoelectronic and electrochemical devices. However, many fundamental questions remain about the physics of localized surface plasmon resonance (LSPR) in these materials, and how their optoelectronic properties derive from their underlying structural properties. In particular, the influence of the concentration and distribution of dopant ions and compensating defects on the optoelectronic properties of TCO nanocrystals has seen little investigation.

Indium tin oxide (ITO) is the most widely studied and commercially deployed TCO. Herein we investigate the role of the distribution of tin dopants on the optoelectronic properties of colloidally prepared ITO nanocrystals. Owing to a high free electron density, ITO nanocrystals display strong LSPR absorption in the near infrared. Depending on the particular organic ligands used, they are soluble in various solvents and can readily be integrated into densely packed nanocrystal films with high conductivities. Using a combination of spectroscopic techniques, modeling and simulation of the optical properties of the nanocrystals using the Drude model, and transport measurements, it is demonstrated herein that the radial distribution of tin dopants has a strong effect on the optoelectronic properties of ITO nanocrystals.

ITO nanocrystals were synthesized in both surface-segregated and uniformly distributed dopant profiles. Temperature dependent measurements of optical absorbance were first combined with Drude modeling to extract the internal electrical properties of the ITO nanocrystals, demonstrating that they are well-behaved degenerately doped semiconductors displaying finite conductivity at low

temperature and room temperature conductivity reduced by one order of magnitude from that of high-quality thin film ITO.

Synchrotron based x-ray photoelectron spectroscopy (XPS) was then employed to perform detailed depth profiling of the elemental composition of ITO nanocrystals, confirming the degree of dopant surface-segregation. Based on free carrier concentrations extracted from Drude fitting of LSPR absorbance, an inverse correlation was found between surface segregation of tin and overall dopant activation. Furthermore, radial distribution of dopants was found to significantly affect the lineshape and quality factor of the LSPR absorbance. ITO nanocrystals with highly surface segregated dopants displayed symmetric LSPRs with high quality factors, while uniformly doped ITO nanocrystals displayed asymmetric LSPRs with reduced quality factors. These effects are attributed to damping of the plasmon by Coulombic scattering off ionized dopant impurities.

Finally, the distribution of dopants is also found to influence the conductivity of ITO nanocrystal films. Films made from nanocrystals with a high degree of surface segregation demonstrated one order of magnitude higher conductivity than those based on uniformly doped crystals. However, no evidence was found for differences in the surface electronic structure from one type of crystal to the other based on XPS and the exact mechanism for this difference is still not understood.

Several future studies to further illuminate the influence of dopant distribution on ITO nanocrystals are suggested. Using synchrotron radiation, detailed photoelectron spectroscopy on clean ITO nanocrystal surfaces, single-nanoparticle optical measurements, and hard x-ray structural studies will all be instructive in elucidating the interaction between oscillating free electrons and defect scattering centers when a plasmon is excited. In addition, measurements of temperature and surface treatment-dependent conductivity with carefully controlled atmosphere and surface chemistry will be needed in order to better understand the transport properties of ITO nanocrystal films. Each of these studies will enable better fundamental knowledge of the plasmonic properties of nanostructures and improve the development of nanocrystal based plasmonic devices.

Für mein Opa, Eugen Bodendörfer, der mich immer zum erforschen inspiriert hat

Table of Contents

Acknowledgements

First and foremost, I would like to acknowledge and thank my research adviser for the past two and a half years, Delia Milliron, who took a chance on a 4th year grad student and has mentored me and pushed me to become a better scientist ever since. Switching to your group was the best decision I made in grad school. Your honesty, approachability, and sense of humor were always appreciated. Thanks for keeping me motivated even when it seemed the results would never come.

I would also like to acknowledge the entire Milliron research group, who were always a pleasure to spend time with, both in the lab and outside. I have never worked with a more committed, talented, and humble group of people and will always remember how great a work environment can be when everyone cares about each other. I would especially like to thank Memo for showing me the ropes when I first joined the group, Raffa for always responding with a smile, no matter how basic the chemistry question I asked, Evan, Anna, and Amy for being such fantastic teammates on our papers, and Rob for asking tough questions and being the best beamline buddy a guy could ask for.

This work would not have been possible without the help of my hard-working collaborators. In particular, I would like to thank Georgetta Mason for teaching me about polymer chemistry and Dennis Nordlund for his tireless efforts in making sure we got terrific data at the synchrotron and his crucial insights in helping us understand them.

I would like to thank my qualifying exam and thesis committee members, Professors Javey, Dubon, Wu, and Cuk for their helpful feedback and support throughout my graduate career.

I would like to acknowledge Professor Alessandra Lanzara, my research adviser for the first three and a half years of graduate school for guiding me through my first few research projects and advocating for me when it was time to find a better fit for my interests. I would also like to acknowledge the rest of the Lanzara research group, who are still the smartest and friendliest bunch of people I know. I would especially like to thank Chris Jozwiak and David Siegel, who were great mentors when I first got to Berkeley and continue to be great friends, and Chris Smallwood for sharing the ride through grad school with me from start to finish.

One thing is certain: I would never have finished this degree without the immense support – moral, academic, and financial – from the Graduate Group in Applied

Science and Technology. In particular, Pat Berumen and Professor Dave Attwood were always available at the drop of a hat to answer questions, offer encouragement, provide advice, and, all in all, make sure I, and the other AS&T students, had everything we needed, even when resources were scarce.

Finally, I would like to thank the people that make it all worth it at the end of the day: my wonderful family and friends. Your support, encouragement, and patience kept me going along this six-year adventure. Caydie, Denia, Vitaly, Jose, and Santi, thanks for always being there to laugh, cry, commiserate, and celebrate. Mom, Dad, and Julien, I wouldn't be where I am today without your unconditional love and support. I hope to always make you proud and be there with you through thick and thin.

1. Introduction

1.1 Colloidal nanocrystals of transparent conducting oxides

1.1.1 Transparent conductors and transparent conducting oxides (TCOs)

Transparent conductors are a special class of materials that defy the empirical observations of our everyday experience. Consider metals, which are nearly always excellent conductors of electricity, but are decidedly not transparent. Owing to the interaction of a high density of free electrons with electromagnetic radiation, most metals look shiny and opaque. On the other hand, most transparent materials are terribly poor conductors of electricity due to their wide electronic band gaps. The glass found in most windows, for example, has an electrical conductivity that is more than 18 orders of magnitude lower than the most conductive metals, making it a phenomenal insulator.

Transparent conductors are remarkable because they bridge this enormous gap between the properties of metals and insulators, opening pathways to several important applications. Specifically, any application in which light must pass through a component of an electronic device without a break in the ability of current to flow is a candidate for use of a transparent conductor. Among these, photovoltaic cells, displays, and electrochromic "smart" windows are some of the most prevalent examples. In each of these applications, the ability of light to pass into or through the device is central to its functionality.

For this reason, transparent conducting materials have seen significant scientific study and commercial development over the last several decades as optoelectronic technology has burgeoned and matured (Figure 1.1.1).[1] The most extensively studied and widely employed of these materials are the transparent conducting oxides (TCOs), of which tin-doped indium oxide (ITO) is the most prolific (See Section 2.2). In the TCOs, high conductivity in a transparent host material is most-often achieved by controlled doping with impurities. If an atom in the lattice is replaced by an impurity atom of higher valency, this aliovalent doping leads to an increase in the number of free electrons, allowing tunable conductivity approaching that seen in metals. In ITO, doping is achieved by substituting $Sn(IV)$ ions for $In(III)$ ions and can lead to conductivities within one order of magnitude of those found in metals while maintaining ~90% optical transparency.
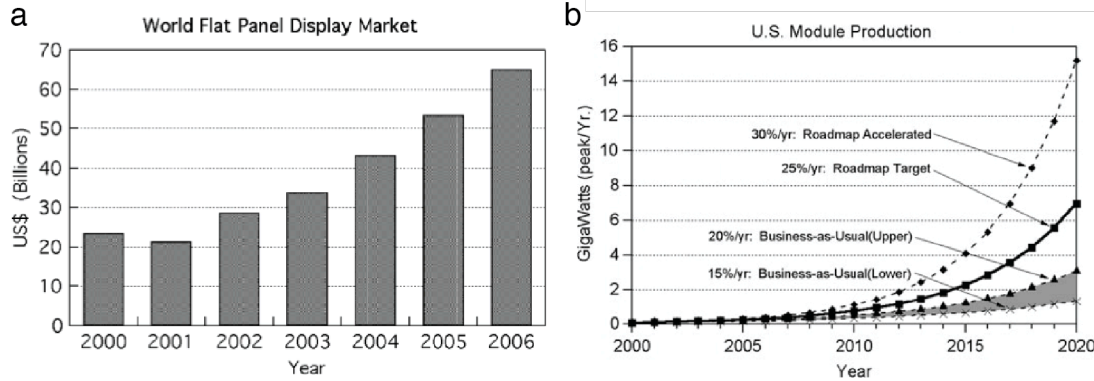
Figure 1.1.1. (a) Growth in the market for flat panel displays and (b) projected increases in U.S. photovoltaic module production signal burgeoning demand for low cost transparent conductors like TCOs. Adapted from ref [1]

1.1.2 LSPRs in Nanomaterials of TCOs

Over the past two decades, researchers have developed the ability to manufacture nanoscale versions of many common material systems, including TCOs, through numerous fabrication and synthetic techniques. Taking materials to the nanoscale often imparts them with optical and electronic properties that diverge strongly from those that are characteristic of the bulk material. In particular, the interaction of nanomaterials with visible and infrared light is often enhanced because these materials have features that are smaller than the corresponding wavelength.

Among these enhanced interactions, the observation of localized surface plasmon resonances (LSPR) in metal and semiconductor nanocrystals has seen increasing interest in recent years.[2–6] LSPRs involve the collective oscillation of the free electron cloud upon excitation by incident light and lead to dramatically enhanced scattering and absorption of light for sub-wavelength nanostructures. LSPRs also generate strong near-field enhancement of electric fields near the surface of the nanostructure due to the polarization of the electron cloud relative to the positively charged ions in the lattice of the material. Owing to their high electron concentrations, several TCO materials are known to display LSPRs, including ITO, which is the focus of this work.

Nanocrystals of many materials can now be produced using the methods of colloidal chemistry and straightforward colloidal syntheses have been developed for several TCO's including ITO. Colloidal synthesis is performed in solution and typically results in a reaction product suspended as an ink in a common solvent. Thus, in addition to the novel optoelectronic properties that arise at the nanoscale, colloidally manufactured nanocrystals have a potential cost advantage over traditional bulk materials. Solution processing of nanocrystal inks using techniques like inkjet printing, spray coating, blade coating, *etc.* opens the opportunity for low cost deposition of TCOs for electronic devices. Since most

3

colloidal nanocrystals are rendered soluble by the use of organic capping ligands, which can be readily removed by ligand exchange, ligand stripping, or low temperature annealing, devices based on these materials are also more compatible with flexible substrates.

1.2 Fundamental questions about plasmonic semiconductor nanocrystals

While there is growing knowledge about synthetic methods to manufacture doped semiconductor nanocrystals that display LSPRs, many fundamental questions about the physics of LSPRs in these materials remain unanswered and are active research questions in the field today. These include, but are not limited to:

1. The validity of describing the optical properties of plamonic nanocrystals using classical electrodynamics in the Drude model (Sections 2.3.2 and 2.4.3), in particular the size regimes at which this description breaks down.[7]
2. The relationship between the optoelectronic properties of bulk crystals and those of nanocrystals made from the same material.
3. The mechanisms and timescales of carrier scattering and dephasing of the LSPR oscillation and how these differ from plasmonic metal nanocrystals.
4. The effect of internal structural details, including dopant and defect types, distributions, and densities, as well as nanocrystal size and shape on the extrinsic optoelectronic properties of the nanocrystals and the behavior of the LSPR in particular.

Each of these questions will be explored in this thesis and in future work based on that presented herein. In particular, Chapters 4 through 6 will focus largely on (2) and (4).

In addition to these fundamental physics questions, questions about the chemistry of doping in TCO nanocrystals also continue to intrigue researchers. The chemical strategies leading to effective nanocrystal doping are clearly differentiated from the well-understood doping regimes found in bulk materials. As such, the correlation between synthetic conditions and final properties, as well as the mechanism of dopant incorporation (thermodynamic vs. kinetic[8–11]), lattice positioning (substitutional vs. interstitial[12,13]) and solubility (vs. bulk materials[13]) are not well understood for doped MO NCs like ITO. Furthermore, investigation of the dopant's fate upon solution aging or during post thin-film deposition processes like annealing could be used to directly compare the synthetic method and dopant positioning in the lattice to device performance. For this reason, specific knowledge of structural details like the dopant coordination environment,

4

lattice positioning and concentration depth profile in metal oxide nanocrystals is crucial to better understanding the doping mechanisms at hand and inspiring the design of new plasmonic nanomaterials and devices.

1.3 Motivation for exploring radial dopant distribution in ITO

In many ways, ITO nanocrystals are an ideal system for exploring plasmonic optoelectronics in semiconductor nanomaterials. Having been extensively studied in its thin film and bulk phases, there is a tremendous wealth of knowledge about ITO in the literature, upon which hypotheses and experimental benchmarks can be founded in exploring its properties at the nanoscale. Furthermore, being conductive, transparent, easily processed in a number of solvents, and well-behaved in densely packed thin films, ITO nanocrystals are compatible with many commonly used optical and x-ray spectroscopies and transport measurement techniques. Finally, as is discussed in detail in Section 2.4.3 below, ITO possesses rich doping and defect chemistry that leads to fundamentally different free electron properties than those found in metals. Thus, ITO nanocrystals present a unique opportunity to study a material system with both tremendous practical potential, with active pursuit of several technological applications underway, and host of unanswered fundamental questions.

Over the course of the work that went into this thesis, our group discovered reliable and distinct synthetic approaches to producing ITO nanocrystals with surface segregated dopants and uniformly distributed dopants. While the chemical reasons underlying these different dopant distributions are still mysterious, this discovery opened the possibility of studying the influence of a simple but drastic radial anisotropy in defect distribution on the optoelectronic properties of the material. The work presented in this thesis largely revolves around this anisotropy, which was found to dramatically impact the plasmonic and electronic properties of ITO nanocrystals and nanocrystal films.

2. Background

2.1 Colloidal synthesis of doped semiconductor nanocrystals

Adapted from ref [14]:

E.L. Runnerstrom, A. Llordes, S.D. Lounis, D.J. Milliron. "Nanostructured electrochromic smart windows: traditional materials and NIR-selective plasmonic nanocrystals." *Chem. Commun* (2014) Advance Article. DOI: 10.1039/C4CC03109A

2.1.1 Overview of colloidal synthesis

To achieve changes in nanocrystal doping, size, or to utilize new plasmonic materials, our group has turned to organic phase colloidal nanocrystal synthesis. The well-established surfactant-mediated method for colloidal synthesis allows one to grow nanocrystals from molecular precursors in solution phase at moderate temperatures between 150°C and 400°C (Figure 2.1.1). Surfactant-assisted colloidal synthesis offers excellent control over nanocrystal size and shape, as well as preventing their aggregation and precipitation from solution,[15–18] which enables stable colloidal dispersions (Figure 2.1.1c). Such dispersions can serve as inks for solution deposition of nanocrystal films using potentially low cost and industrially scalable techniques such us spray coating or slot die coating, as well as laboratory-scale techniques like spin coating. More recently, it has become possible to finely control nanocrystal composition, providing enhanced tunability of dopant concentrations and hence LSPR frequency.[13,19,20] These advances have been critical for the development of plamonic semiconductor nanocrystals, and have also contributed momentum to new research on plasmonic optoelectronics.[5,21]

2.1.2 Doping colloidal semiconductor nanocrystals

While the field of colloidal synthesis is well developed and small-diameter nanocrystals on the order of 1 nm can be obtained, achieving high doping levels has been more elusive and challenging.[10,12,22,23] The emergence of plasmonic semiconductor nanocrystals has done much to motivate research on doping strategies. Today, chemists have achieved far better control over the incorporation of dopants into colloidal nanocrystals, and can now do so with a high degree of control over the dopant content (Figure 2.1.1e).[11]

Growing colloidal nanocrystals from solution phase is a kinetically controlled process; introducing dopants within the lattice (Figure 2.1.1d) therefore requires a fine balance of the host nanocrystal growth rate and the dopant incorporation rate. A variety of doping strategies have been reported for several nanocrystal compositions, and they have been recently reviewed and discussed in depth.[11] For the particular case of binary metal oxides, the most popular doping strategy

is based on tuning the relative chemical reactivity of the molecular precursors for the host nanocrystal and for the dopant atom. Typical precursors are metal-organic salts comprising the metal of interest and a ligand (e.g. an alkyl carboxylate). By selecting a ligand with the appropriate steric hindrance and negative charge delocalization properties, it is possible to tune the ligand-metal bond strength to balance the reactivity of both precursors. By developing this strategy, our group was able to demonstrate the first synthesis of plasmonic, monodisperse Al-doped ZnO nanocrystals of controlled sizes and dopant levels.[13,24] Substitutional doping strategies have been also proven successful for other TCO nanocrystals, such as Sn-doped In_2O_3[19,25] Nb-doped TiO_2,[26] and In-doped CdO.[20]

Understanding the role of size, doping on the plasmonic properties of nanocrystals is of tremendous importance to generate fundamental knowledge about the LSPR behavior. The fine control over size and composition offered by colloidal synthesis has enabled our group to pioneer these systematic studies by synthesizing colloidal plasmonic nanocrystals (ITO and AZO) over broad size ranges (4 nm up to 16 nm) (Figure 2.1.2), with narrow size distributions (<15% std. deviation in diameter), a high degree of crystallinity, and well-controlled dopant concentrations.[13,24]
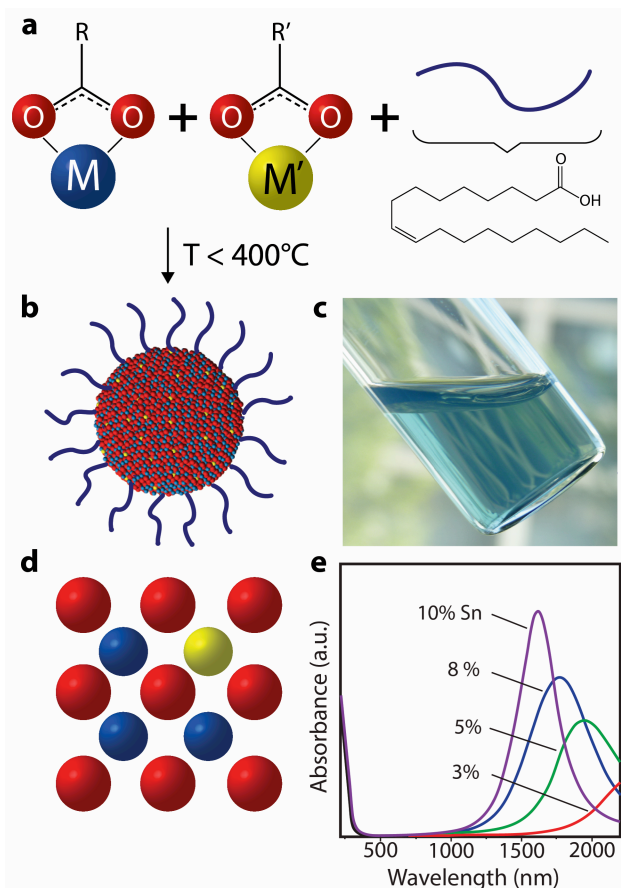
Figure 2.1.1 Colloidal synthesis of doped metal oxide nanocrystals. (a) Molecular precursors (depicted here as metal carboxylates) are combined with ligands (oleic acid depicted) in a non-polar solvent and heated to moderate temperatures. (b) After the precursors decompose and react, inorganic colloidal nanocrystals are formed, which are stabilized in solution by the ligands coordinated to the surface. (c) Optically clear dispersion of colloidal ITO nanocrystals in hexane. (d) Substitutional doping mechanism whereby a donor atom (i.e. Sn) occupies a metal (i.e. In) site in the nanocrystal, thereby introducing electrons into the conduction band. (e) Absorbance spectra of ITO nanocrystals, showing a blueshift, narrowing, and enhanced intensity of the plasmon peak as doping increases. Part (e) adapted from ref. 54.
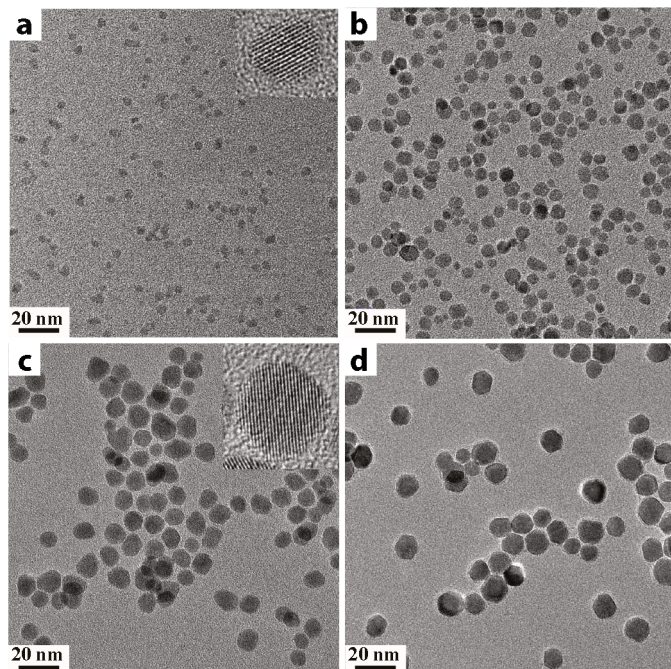
Figure 2.1.2. Transmission electron microscopy images of ITO nanocrystals with sizes (nm): (a) 4.1 ± 0.6, (b) 7.4 ± 1.4, (c) 10.2 ± 1.7, and (d) 12.1 ± 1.5.

2.2 Tin doped indium oxide

2.2.1 Technological importance

Tin-doped indium oxide (ITO) is a degenerately doped semiconductor that displays high electronic conductivity and visible transparency, making it an excellent candidate as an electrode material for optoelectronic applications. For this reason, efforts to understand its optoelectronic and material properties have garnered much attention in the scientific literature, as well as industrial research and development laboratories. Today, transparent electrodes based on ITO, along with other related materials based on doped indium and tin oxide, are used for applications in display technology, organic light-emitting diodes, solar cells, and energy saving smart windows, to name only a few. In academic research labs, ITO has also seen a recent resurgence as a plasmonic material in its nanocrystalline form, as discussed throughout this thesis.

This degree of attention has also led to a profusion of growth and deposition methods for thin films of ITO. The most common among these are thermal evaporation, sputtering, and sol-gel techniques.[27] The overall optoelectronic properties of the ITO film depend strongly on both the deposition technique used and the specific details of the deposition conditions. This is due largely to the complicated defect chemistry of ITO and its dependence on oxygen activity (See section 2.2.3 and 2.4.2).

10

2.2.2 Bulk/Thin Film optoelectronic properties

Pure indium oxide is an insulator with a bandgap of ~3.5 eV, making it transparent for wavelengths in the visible and above. Electrons are introduced into the conduction band of In2O3 primarily by two mechanisms, the formation of oxygen vacancies in lattice and the introduction of substitutional dopant ions of valency IV on indium sites, the most common of which being Sn (IV). Uncompensated oxygen vacancies contribute two electrons to the conduction band, while uncompensated tin dopants contribute one electron (See section 2.4.2 for more details). Based on these doping mechanisms, thin film ITO can have electron densities on the order of 10^{20} cm^{-3}, well above the minimum density of ~10^{18} cm^{-3} required for degeneracy by the Mott condition. Electronic mobility in ITO ranges from ~10 – 80 depending on the growth technique and conditions.

Due to scattering from ionized impurities, electronic mobility in ITO depends strongly on the degree of tin doping (See sections 2.2.3 and 2.4.2) and will tend to decrease as doping increases. For this reason there is an optimum level of doping – with high electron density and low mobility – that corresponds to maximum conductivity for ITO. Most ITO thin films achieve conductivities on the order of 10^3 – 10^4 S/cm, which is only about one order of magnitude lower than most metals.

In addition to being highly transparent in the visible region of the spectrum, with typical thin films achieving ~90% transmittance, ITO is also typically highly reflective in the near infrared (NIR) (Figure 2.2.1 a and b). This is due to the high free electron density in ITO, which leads to a plasma frequency in the NIR that can be tuned by changing the relative activation of tin dopants based on the oxygen activity in the environment around film (e.g. by annealing in oxidizing or reducing conditions). In plasmonic ITO nanocrystals, the absorbance can also be tuned electrochemically, forming the basis for the operation of plasmonic smart windows (Figure 2.2.1 b and d).
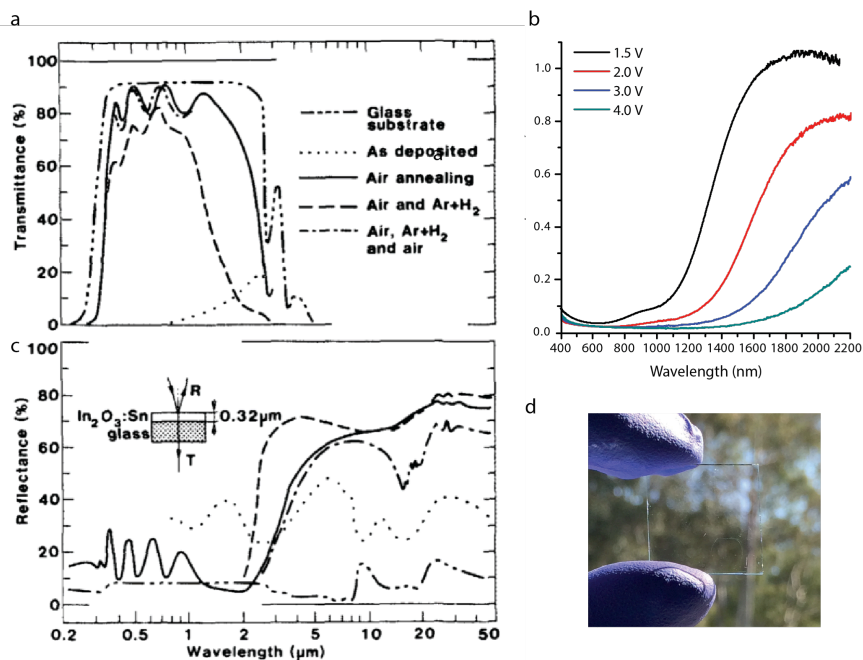
2.2.1 Optical properties of ITO thin films and nanocrystal films. (a)Transmitance and (c) reflectance of ITO thin films show visible transparency and NIR reflectivity. (b) LSPR in ITO nanocrystals can be tuned electrochemically through the NIR, (d) making possible NIR-selective but visibly transparent smart windows. Reprinted from refs [28,29]

Many reviews and research papers treat the electronic and optical properties of ITO thin films in great detail,[27,28,30] to which I refer the reader for more information.

2.2.3 Defect chemistry and optimization of conductivity

The predominant model for the defect chemistry of ITO was developed by Frank and Köstlin,[31] who investigated the electronic properties of ITO films as functions of doping and oxygen partial pressure. In particular, they observed that the total electron density does not scale linearly with the density of tin dopants, indicating the influence of a compensation mechanism acting as a free-electron sink. Both the electron density and mobility were also observed to depend on partial oxygen pressure. Based on these observations Frank and Köstlin proposed the formation of complexes between tin dopants and oxygen interstitial atoms occupying empty interstitial sites in the In_2O_3 lattice (Figure 2.2.2). As more tin is added to the system, aggregates of such complexes become non-reducible, compensating the tin dopants. The interplay of tin doping and oxygen interstitials is discussed further in Section 2.2.4. In the years since Frank and Köstlin's results, more detailed theoretical and experimental structural studies of ITO have supported to important role of oxygen interstitials in compensating tin dopant, though the exact nature of the defect clusters is still actively debated.[32–37]
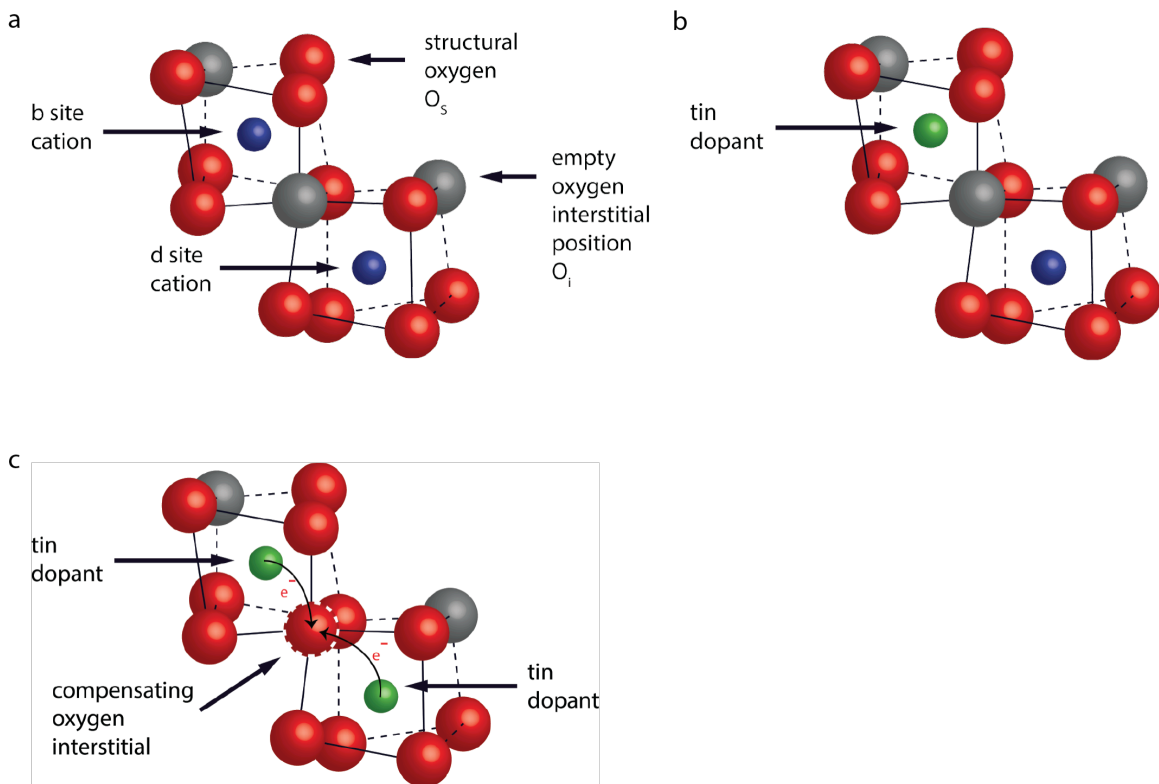
Figure 2.2.2 Doping and compensation mechanisms in ITO. Adapted from ref. [36]

Due to compensation by oxygen interstitials, the maximum free carrier concentration achievable by tin doping is limited. In fact, above a certain level of doping, the carrier concentration will begin to decrease with increasing tin doping. This effect must also be considered in optimizing the overall conductivity of ITO films. Furthermore, since neutral (i.e. compensated) defects act as weaker scattering centers than ionized defects, the degree and nature of dopant activation in ITO plays an important role in determining the carrier mobility and, for plasmonic nanocrystals, the lineshape of the LSPR (See Section 5.3).

2.3 The optical properties of metals and degenerate semiconductors

2.3.1 Complex dielectric function

The electromagnetic interaction of light with matter is fundamentally dictated by the phenomenon of polarization. The strength and mechanisms by which electromagnetic radiation can perturb charge in a solid determine its optical properties including its ability to reflect, transmit, or absorb light at a given frequency.   The complex dielectric function, $\varepsilon = \varepsilon_1 + i\varepsilon_2$, which relates the strength of an electric field to the electric displacement within a medium, is a powerful handle for understanding the optical properties of a solid. The complex

13

dielectric function relates the optical properties of a solid to the underlying electronic structure, allowing the use of optical measurements to understand the underlying electronic properties of materials.[38]

2.3.2 The Drude model

In metals and degenerately doped semiconductors like ITO, free electrons in the conduction band are a major contributor to the dielectric function. While it fails in correctly describing several quantum phenomena, most notably the heat capacity of metals, the dielectric behavior of free electrons can be well understood by the Drude model, developed in the year 1900 by Paul Drude. By treating the electrons in a metal as a non-interacting gas of charged particles and applying the classical equation of motion for a charged particle in an external electric field, one can straightforwardly derive the frequency-dependent Drude dielectric function:

$$\varepsilon(\omega) = \epsilon_\infty + \frac{4\pi i}{\omega} \frac{ne^2\tau}{m(1 - i\omega\tau)} \qquad (2.3.1)$$

where ε_∞ is the dielectric background due to the polarizability of the ionic background, n is the free electron concentration, m is the mass of the electron, and τ is the average time between elastic collisions of electrons with ions in the lattice.[38]

An important feature of the Drude dielectric function is its dramatically different behavior at low and high frequencies. At low frequencies, the free electron contribution dominates over that of the ionic background and leads to near perfect reflection of light. At high frequencies the ionic background dominated and leads to near perfect transmission of light. The threshold frequency between these regimes is known as the plasma frequency (See section 2.4.3).[38]

2.4 Localized surface plasmon resonance in metal oxide nanocrystals

Reprinted from ref [39]:

S.D. Lounis, E.L. Runnerstrom, A. Llordes, D.J. Milliron. "Defect chemistry and plasmon physics of colloidal metal oxide nanocrystals." *J. Phys. Chem. Lett.* **5** (2014) 1564 - 1574

2.4.1 Introduction

Nanocrystals of metal oxides have recently emerged as a compelling route toward tunable plasmonics. The advancement of colloidal synthesis of highly-

14

doped semiconductor nanomaterials[10–12] has enabled the production of a host of oxide materials demonstrating localized surface plasmon resonances (LSPRs). In metals, these collective oscillations of free electrons or holes lead to enhanced optical absorption and scattering, as well as strong near field enhancement at the nanoparticle surface, and are sensitive to particle size, shape, and the dielectric environment surrounding the particle. In semiconductors, LSPRs are additionally inherently tunable by varying doping level and electrochemical potential, allowing observations of plasmonic effects across visible, near-infrared (NIR), and mid-infrared wavelengths (Figure 2.4.1) and enabling new classes of devices with functionalities in these regions of the spectrum. This tunability has already led to the development of a new class of smart windows[29,40] and has generated interest around metal oxide nanocrystals for applications including chemical sensing and bio-sensing, telecommunications, and advanced optics and photonics.[6,41,42] At the same time, the complex interplay between the structural and electronic properties introduced by doping in these materials and the physics underlying the behavior of LSPRs has opened a host of fundamental questions within the rich and growing field of plasmonic optoelectronics.

The surfaces of metals and highly doped semiconductors can maintain surface plasmon resonances, which oscillate and propagate within a thin surface layer defined by the skin depth of the material.[43] LSPRs, by contrast, involve the oscillation of all of the conduction electrons in a nanoparticle, and emerge under the confluence of critical requirements for free carrier concentration and particle size.[4,5,43] A doped semiconductor must have a negative real part of its dielectric function in order to display metallic optical properties. This condition is achieved above a critical free carrier concentration that depends on the electronic structure of the material, including the effect of defect states. Several wide bandgap oxide semiconductors can be routinely doped above the threshold for metallic optical behavior.

Metal NCs: WO₃ NCs: ITO NCs: ICO NCs: AZO NCs:
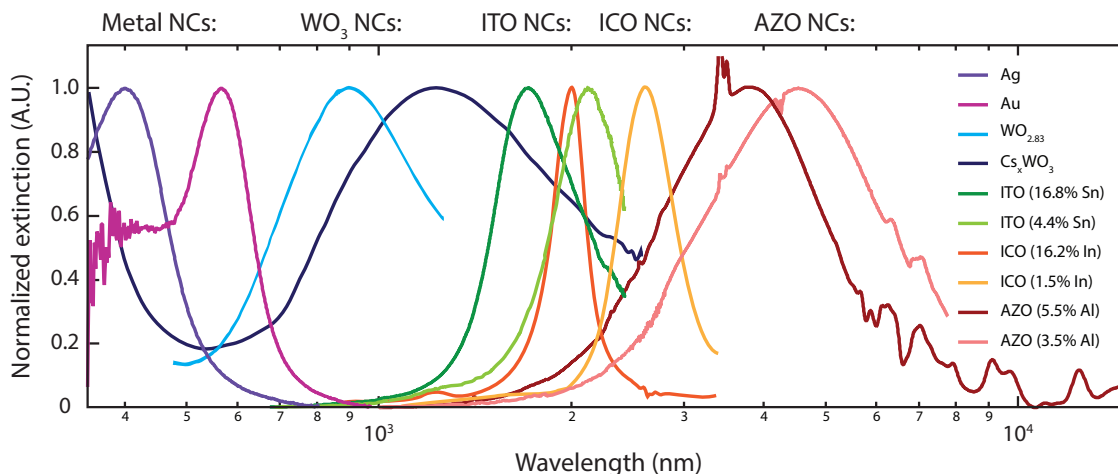
Figure 2.4.1. Normalized optical extinction due to localized surface plasmon resonances in solutions and films of metal and metal oxide nanocrystals. Oxide LSPR spectra adapted left to right from refs [13,20,29,44,45].

To support a dipolar LSPR, the diameter of a nanoparticle whose composition has the proper dielectric properties must be less than approximately one-fifth of the corresponding LSPR wavelength. Thus, particles less than 100 nm in diameter can have LSPRs in the visible to infrared range, leading to strong optical extinction in these frequency ranges. In this regime, the electric field felt by the particle under optical excitation can be reasonably approximated as uniform across its entire volume. The LSPRs can thus be understood as arising from the *electrostatic* interaction of the exciting radiation with the free electron gas. The optical linewidth of the plasmon resonance is determined by the scattering of electrons in the bulk and at the surface of the crystal, which damps the harmonic oscillation. For this reason, a common figure of merit for plasmons is the quality factor, $Q = E/\Delta E$, which compares the energy of the LSPR to its linewidth.

This Perspective examines the emergence of LSPR phenomena in metal oxide nanocrystals doped to induce metallic optical behavior. The defect chemistry underlying doping and compensation is addressed and implications for the plasmon physics of these materials are elaborated. Key fundamental differences that distinguish materials reported in the literature are explained, culminating in an outlook toward emerging directions as we deepen our understanding of plasmonic phenomena in metal oxide nanocrystals.

2.4.2 Doping Mechanisms in Metal Oxide Materials

While the doping of colloidal semiconductor nanocrystals is rife with synthetic challenges,[11] the underlying defect chemistry can be largely understood by reference to that found in bulk materials. In metal oxides, it is instructive to

16

consider the doping properties as a function of oxygen activity as it demonstrates the important interrelationships between the most common doping and compensation mechanisms. The introduction of free charge carriers in these materials is generally achieved by some combination of three mechanisms (Figure 2.4.2): 1) intrinsic doping by lattice vacancies, 2) extrinsic aliovalent substitutional doping, and, less commonly, 3) extrinsic interstitial doping. The electron or hole donation activity of these defects will depend strongly on the oxygen activity. Aliovalent defects, in particular, may be stoichiometrically compensated by other ionic defects that maintain charge-neutrality. In all cases, when the oxygen activity shifts away from equilibrium, free electrons or holes populate the material to maintain charge neutrality as the concentrations of charged defects change.[46] This dynamic balance between activation and compensation of defects via oxidation and reduction determines the properties of free electrons in metal oxides and is therefore central in understanding LSPRs in metal oxide nanocrystals. As ionized and neutral defects serve as obstacles to electron motion with distinct scattering cross sections, their relative concentration are important in determining the damping of the LSPR, and its corresponding optical linewidth and quality factor.

Several metal oxide materials can exhibit significant doping by way of oxygen vacancy defects (Figure 2.4.2b), including indium oxide (In_2O_3), tungsten oxide (WO_3), and molybdenum oxide (MoO_3). Because of the strong electron affinity of oxygen, the filled valence band of a metal oxide is largely derived from oxygen orbitals. Oxygen being a dianion, an oxygen vacancy thus creates a shallow donor level that is readily thermally ionized, introducing two "extra" electrons to the conduction band and leaving a doubly ionized point defect (V_O) in the lattice. The equilibrium concentration of oxygen vacancies in a given metal oxide will be governed by the thermodynamics of defect formation and can be varied by adjusting the partial pressure of oxygen gas in the system, while nonequilibrium defect concentrations may be kinetically stabilized. In nanocrystals of WO_3 and MoO_3, this so-called "self-doping" can be sufficient to increase the electron concentration to levels at which LSPRs in the visible and NIR are observed.[5,44,47]
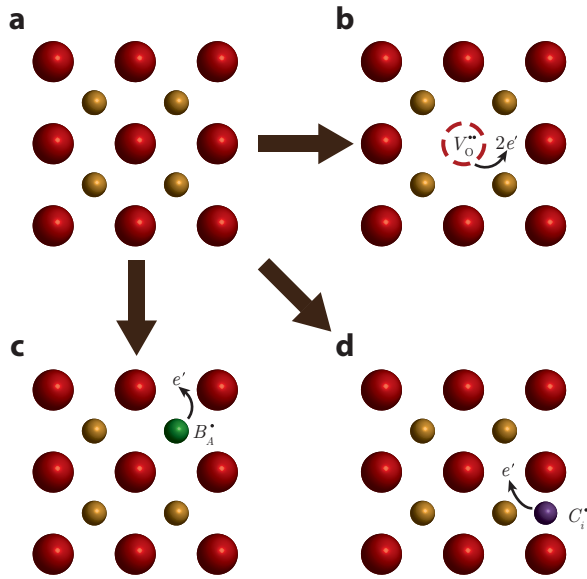
Figure 2.4.2. Schematic representation of the common doping mechanisms in metal oxides relative to (a) a basic lattice containing metal cations (orange spheres) and oxygen anions (red spheres). (b) Oxygen vacancies act as double electron donors, while (c) aliovalent substitutional impurities, and (d) interstitial impurities typically contribute one free electron. In each case, a charged defect is also introduced in the lattice, serving as a Coulombic scattering site for electron motion.

Being foundational in microelectronic technology, aliovalent substitutional doping (Figure 2.4.2c) is a commonly used and well-understood mechanism for tuning the properties of semiconductors. In metal oxides, aliovalent doping is widely employed to produce highly doped transparent conductors with metallic conductivity, including tin-doped indium oxide (ITO), fluorine-doped tin oxide (FTO), aluminum-doped zinc oxide (AZO), antimony-doped tin oxide (ATO), and indium-doped cadmium oxide (ICO). In this approach, a lattice atom is substituted with one of higher or lower valence, introducing shallow electron or hole states into the band structure. In metal oxides, this is usually accomplished by substituting for the metal cation to *n* or *p*-dope the system. Since the conduction band in metal oxides is largely derived from the valence orbitals of metal cations, substituting a higher oxidation state cation can create a shallow donor level and introduce "extra" electrons to the conduction band. As mentioned above, such defects can be compensated by other ionic defects including cation vacancies and oxygen interstitials for n-type doping and cationic interstitials and oxygen vacancies for p-type doping. Oxygen vacancies are often the dominant ionic defect for reasonably attainable oxygen activities, and compensation mechanisms are highly efficient for the case of hole doping, so that p-type metal oxides are rarely realized.
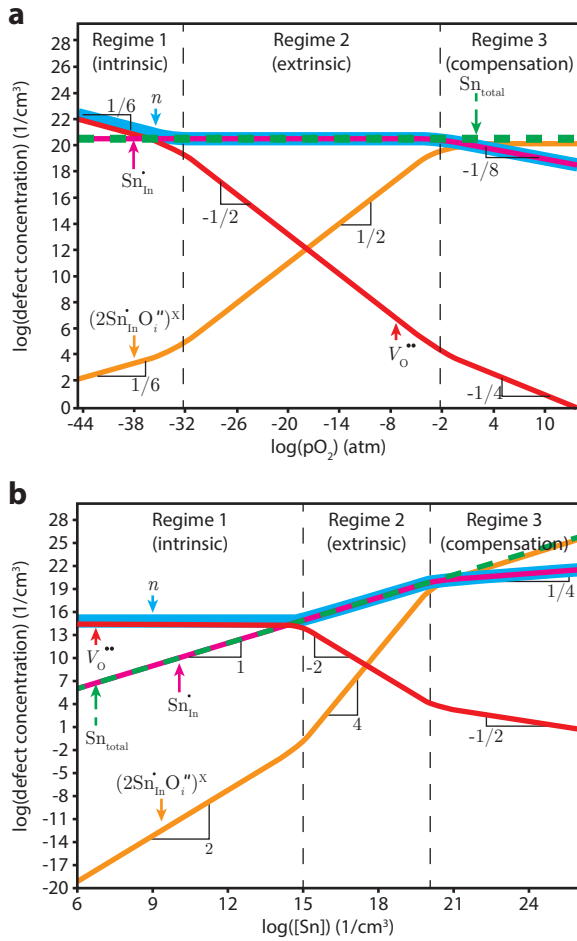
Figure 2.4.3. Brouwer diagram for common defects in ITO (a) relative to partial oxygen pressure (pO₂) at fixed Sn doping level ([Sn]) and (b) [Sn] at fixed pO₂. In both cases, the free electron concentration, n, depends on the relative concentration of substitutional tin atoms, Sn_{In} , oxygen vacancies, V_O , and oxygen interstitial atoms, which compensate Sn by forming neutral complexes, $(2Sn_{In} - O_i'')$. This complex relationship leads to intrinsic, extrinsic, and compensating regimes as pO₂ or [Sn] is increased. Reprinted with permission from Ref [48]. Copyright 2000 Elsevier.

Among metal oxides, ITO is an excellent model system for understanding the complex interplay between doping and compensation. Free electrons in ITO are primarily introduced by aliovalent substitution In^{3+} by Sn^{4+} and, to a lesser extent, by oxygen vacancies in the In_2O_3 lattice. Because it crystallizes in the bixbyite structure, in which ¼ of the oxygen sites in the cubic lattice are stoichiometrically vacant, the ITO lattice is also able to readily accommodate oxygen interstitial defects, which can compensate n-type aliovalent donors. Detailed theoretical and structural studies have established that neutral defect clusters of tin with oxygen interstitial atoms play an important role in the defect chemistry of ITO.[31,36] Complexes between substitutional tin and oxygen interstitials $(2Sn_{In} - O_i'')$ are in

some cases non-reducible and these act as sinks for electrons. As a result, the free electron and structural defect concentrations together depend strongly on both the oxygen activity and cation doping level (Figure 2.4.3). An important consequence of this dependence is the balance between free-carrier concentration and mobility in determining doping levels to optimize targeted optoelectronic properties.[27] In plasmonic semiconductor nanocrystals optimization of the LSPR quality factor is subject to this trade-off, highlighting the important connection between plasmon dynamics and the transport properties of a corresponding bulk crystal.

In certain oxides, conduction band electrons can also be introduced via doping by interstitial atoms (Figure 2.4.2d), which form shallow defect states in the oxide band structure. This type of doping is most-often encountered in metal oxides with crystal structures able to easily accommodate interstitial atoms in their lattice. Tungsten bronze, for example, which has the formula M_xWO_3, allows interstitial doping up to x=1 by large alkali metal cations because of the open tunnel structures of the partially complete perovskite lattice,[49,50] leading to strong NIR absorption in bulk[51] and nanoparticulate[45,52] forms of these materials.

Recent advances allow colloidal synthesis of nanocrystals of many doped semiconductor materials, including several metal oxides exhibiting LSPR phenomena.[11] This surfactant-assisted approach offers excellent control over nanocrystal size and shape,[15–18] and, more recently, composition, allowing fine-tuning of LSPRs by changing dopant concentrations.[13,19,20] In general, colloidal synthesis requires carefully balanced reaction conditions to establish reaction kinetics that favor the incorporation of dopants into the lattice of the host crystal.[11] For the particular case of metal oxides, we have developed a strategy that involves tuning the relative chemical reactivity of molecular precursors for the host nanocrystal and dopant atom. Typical precursors are metal-organic salts, comprising the metal of interest and a ligand. The thermodynamics of doping nanocrystals involves additional considerations, beyond the fundamental defect chemistry derived from the corresponding bulk materials. For example, free charge carriers introduced by aliovalent and photochemical doping can be readily compensated by localized surface charges, a non-negligible effect in sufficiently small nanocrystals with a high surface to volume ratio.[53] In addition, detailed structural information about the incorporation of dopants in colloidal nanocrystals is still missing[11] and could be influenced by the increased formation energy of defects in nanocrystals.[54] The distribution of dopants within individual crystals and variances in dopant incorporation across nanocrystal ensembles are of particular interest in understanding LSPRs in plasmonic nanocrystals, as they could play a role in determining homogenous and inhomogeneous broadening of the plasmon linewidth, respectively.[55]

2.4.3 LSPR Theory in Doped Metal Oxides

The free electron properties of metallic nanocrystals are conventionally treated within the classical Drude model for a free electron gas.[43] This theory has been effectively applied to understand the plasmonic properties of both metal[4,56] and semiconductor nanostructures,[57] including metal oxide nanocrystals.[55,58,59]

The optical properties of a solid are determined by its complex dielectric function, which describes the polarization response of the valence and conduction electrons to an externally applied electromagnetic field. The Drude contribution to the frequency-dependent complex dielectric constant, $\varepsilon(\omega)$, takes the form,

$$\varepsilon(\omega) = \varepsilon_\infty - \frac{\omega_p^2}{\omega^2 + i\omega\Gamma} \qquad (2.4.1)$$

where the constant ε_∞ represents the high frequency dielectric response of the bound valence electrons, Γ is a damping parameter due to the scattering of electrons, related to the average scattering time (τ) by $\Gamma = 1/\tau$, and ω_p is the plasma frequency given by,

$$\omega_p^2 = \frac{ne^2}{\varepsilon_0 m^*} \qquad (2.4.2)$$

where n is the free electron concentration, e is the elementary electronic charge, ε_0 is the permittivity of free space, and m^* is the effective mass of the electron within the crystal. The plasma frequency can be understood as the resonant frequency of a harmonic oscillator defined by the negatively charged sea of electrons oscillating against the positively charged lattice of ions in a bulk crystal.

From the equations above it is clear that the optical properties of the free electron gas will depend strongly on both the free carrier concentration and the damping of electron motion in this model. As semiconductors, the metal oxides differ from metals in important ways related to both of these parameters. While metals generally have a fixed n due to near-perfect screening of external electric fields, this value can be tuned widely in metal oxides, allowing variation of the absorption and scattering of light by changing the bulk plasma frequency. In addition, the damping parameter, which determines the width and lineshape of the LSPR, is generally frequency-independent in metals, resulting from electron-phonon scattering, electron-electron scattering, radiative energy loss, and surface scattering for sufficiently small nanocrystals,[60] though some metals, like gold, have frequency-dependent damping due to interband electron-electron scattering.[61,62] Here, again, semiconductor nanocrystals must be treated differently due to the effect of ionized impurity scattering arising from dopant ions or ionized vacancies. Because the charge on ionized impurities is screened by the electron cloud, scattering takes on fundamentally different character below

the bulk plasma frequency, where electrons can respond efficiently to the changing electric field and above the bulk plasma frequency, where the field changes too quickly for the electrons to respond. Thus, in addition to frequency-independent scattering due to the mechanisms listed above, frequency-dependent scattering from ionized impurities must be considered in understanding the optical response of semiconductors, including metal oxides.
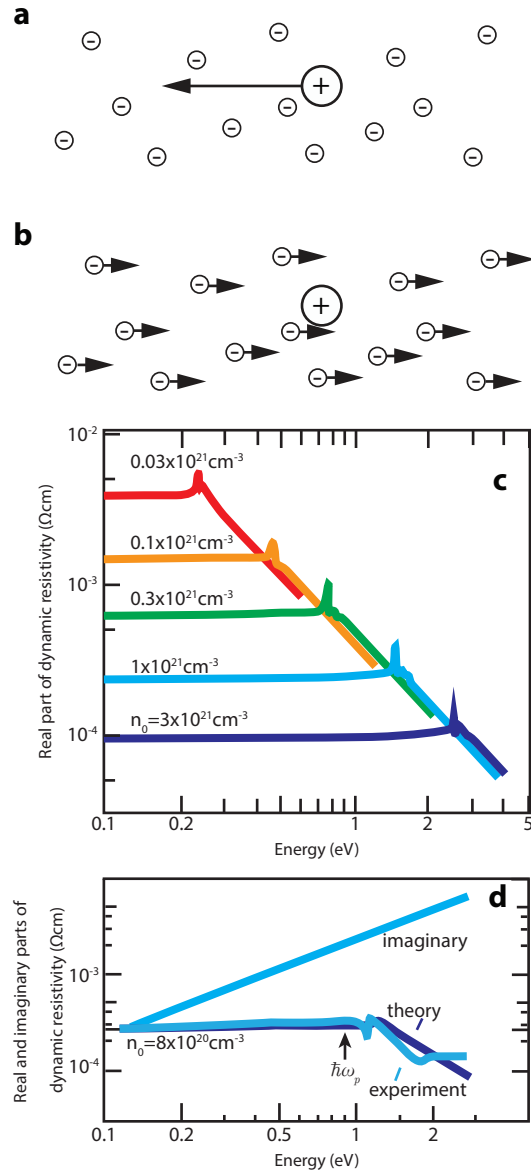

Figure 2.4.4. (a) Energy-loss reference frame compared to (b) transport reference frame. (c) Theoretical calculations of the dynamical resistivity for ITO. (d) Comparison of theory to experiment. (a),(b) Adapted from ref [63]. (c),(d) Reprinted with permission from ref [28]. Copyright 1986 AIP Publishing LLC.

The theory of ionized impurity scattering has been developed in detail within the framework of the complex dynamical resistivity, in which scattering mechanisms due to different types of defects can be treated additively. The real part of the dynamical resistivity corresponds to scattering of electrons. Gerlach and Grosse employed an energy-loss method to calculate the dynamical resistivity for several types of scattering centers, including ionized impurities.[63,64] In this method, the scattering center is taken to oscillate relative to a stationary sea of electrons in order to calculate the scattering interaction, reversing the usual Drude reference frame (Figure 2.4.4a).

Hamberg and Granqvist applied this theory to ITO and compared their calculations to measurements of the real and imaginary parts of the dynamical resistivity (Figure 2.4.4c,d).[28,30] For $\omega < \omega_p$, the real part takes a constant value due to screening of the ionized impurities by the electron cloud. In this regime, an oscillating electron feels effectively the same screened scattering as an electron moving under the influence of a DC electric field. For this reason, the low frequency dynamical resistivity under optical excitation is roughly equivalent to the DC electrical resistivity of the crystal. For $\omega \geq \omega_p$ the screening effect breaks down, as the electron cloud is no longer able to coherently respond to changes in the local electric field at the frequency of oscillation. In this regime, ionized impurities behave as bare Coulomb scattering centers and the dynamical resistivity drops off according to a power-law with an exponent of -3/2 (Figure 2.4.4b).[63] This can be understood intuitively by a reduced scattering probability as higher and higher frequencies correspond to smaller and smaller oscillation amplitudes for a given applied field. In measured ITO thin films, the real part of the dynamical resistivity was found to level off to a constant value for $\omega \gg \omega_p$ due to residual scattering mechanisms other than the ionized impurities (Figure 2.4.4c).

When using the Drude theory to model plasmon resonances in the presence of ionized impurities, the frequency-dependence of the dynamical resistivity can be captured by employing a frequency-dependent damping constant, $\Gamma(\omega)$, in equation (2.4.1). The damping constant is inversely related to the electronic mobility, and thus can be related to the resistivity by the formula,

$$\rho(\omega) = \frac{m^* \Gamma(\omega)}{ne^2} \tag{2.4.2}$$

Both empirical[65] and semi-empirical[28,66–69] models have been used to apply a frequency-dependent damping parameter in modeling metal oxide films, generally taking the form of low-frequency and high-frequency damping

constants that are bridged by a cross-over region corresponding to the power-law regime described above (Figure 2.4.5a). The difference between the low-frequency and high-frequency damping leads to an anisotropy in the lineshape of the LSPR, with the peak being broadened more strongly below the LSPR frequency than above (Figure 2.4.5b).

The bulk free-electron framework described above has been used to model LSPRs in metal nanocrystals[70] and, more recently, extended to study LSPRs metal oxide nanocrystals.[55,58] The optical properties of spherical or spheroidal particles are conventionally described using the Mie-Gans solution to Maxwell's equations.[71] This approach determines the polarizability of a spherical particle by calculating the electric fields inside and outside of the particle under the influence of an externally applied electric field. The polarizability can then be used to calculate absorption and scattering cross sections under electromagnetic radiation. Because of the boundary conditions imposed on the electric fields at the particle surface by Maxwell's equations, the dielectric properties of the medium surrounding the particle directly influence its optical properties. In the quasistatic limit, when the particle diameter is much smaller than the wavelength of light and the applied electric field can be approximated as constant in space across its volume, the Mie solution is greatly simplified and, in the case of scattering, reduces to the Rayleigh description for small particles.
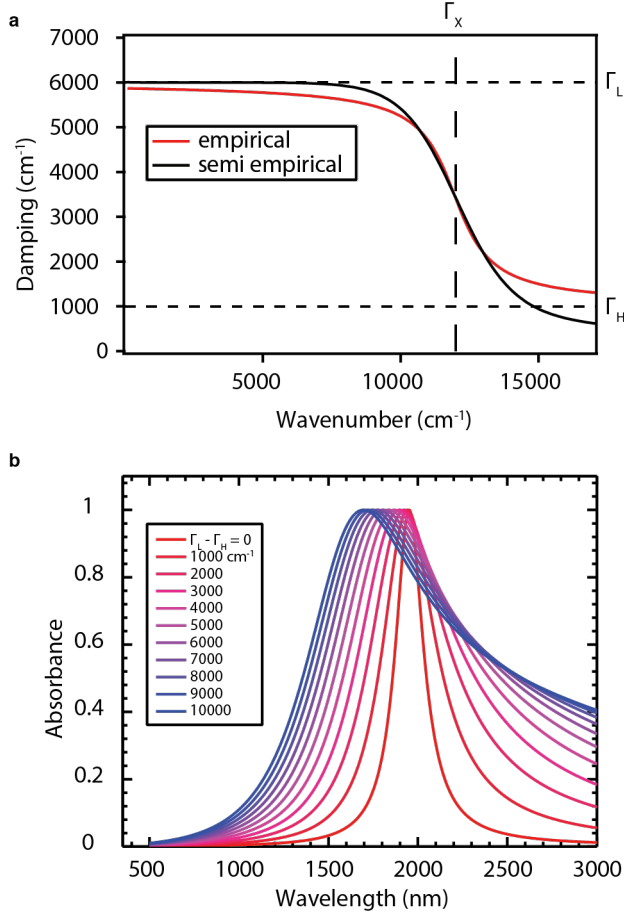
Figure 2.4.5. (a) Empirical and semi-empirical models for frequency dependent damping. Γ_L is the low frequency damping constant, Γ_H is the high frequency dielectric constant, and Γ_X is the crossover frequency (b) Simulated LSPRs for increasing damping anisotropy. As the difference between Γ_L and Γ_H grows, the peak blue shifts and becomes highly asymmetric.

For LSPRs, which occur in the quasistatic limit, the Mie absorption cross section for spherical particles is thus,

$$\sigma_A(\omega) = 4\pi k R^3 Im\left\{\frac{\varepsilon_P(\omega)-\varepsilon_H}{\varepsilon_P(\omega)+2\varepsilon_H}\right\} \tag{2.4.3}$$

where $k = 2\pi\sqrt{\varepsilon_H}\omega/c$, ε_P is the particle dielectric function, including the Drude term for the free electron gas, ε_H is the dielectric constant of the host medium, R

is the particle radius, and c is the speed of light. The total absorbance and scattering can then be calculated using the Beer-Lambert law, taking into account the optical path length and particle volume fraction.

Because it calculates the optical response of a single sphere in a dielectric medium, the Mie solution is only valid in the dilute limit, *i.e.* the solution breaks down when particle volume fractions are high enough for far-field interactions between individual particles to be significant. In this situation, an effective medium approximation (EMA) can be used to understand the overall optical response of the system. Rather than calculating the polarizability of a single particle, EMAs absorb the dielectric properties of the particles and medium into an effective dielectric function for the system as a whole. In this approach, the particle volume fraction is explicitly used to determine the effective dielectric function, capturing far field interactions between particles in concentrated dispersions and dense films. In the dilute limit EMAs are equivalent to the Mie solution.

In the small size limit, where quantum confinement of electrons and holes becomes significant, the classical Drude model breaks down and the LSPR must be treated quantum mechanically. This can be accomplished with a semiclassical extension of the Drude model by treating the plasmon as the sum of single electron quantum states.[72,73] These states are modeled as Lorentz oscillators in an infinite potential well defined at the particle diameter,[72,73] as has been successfully demonstrated in Ag nanocystals[74]. Recently, this method was applied to photodoped ZnO nanocrystals with diameters between 1.75 nm and 6 nm, illuminating the transition from the classical to the quantum regime.[7] The free electron concentration in each batch of nanocrystals was independently verified by titration against mild redox agents and then compared to the values extracted from IR absorbance using a classical and semiclassical Drude approach. Below 6 nm, the classical and semiclassical approaches diverged dramatically, the former grossly miscalculating the free electron concentration and the latter giving accurate predictions.

The Drude approach can also be extended to shapes beyond spheroids using finite element methods like the discrete dipole approximation (DDA).[75–77] In this method, the solid is divided into discrete spherical elements, each with their own individual polarizability. The overall dielectric function is then determined by summing over these individual dipoles within the specified geometry. To date, this approach has mostly been applied to metal nanostructures[4,78,79] and copper chalcogenides,[80] but it also represents an exciting frontier for investigating structure-property relationships in the plasmonic oxides. As was recently demonstrated for silicon nanowires,[81] the DDA method can be used to model nanocrystals with non-uniform structural properties like the distribution of dopants or impurities within the crystal, providing insight into the effect of such non-uniformities on the optoelectronic properties of these systems.

2.4.4 ITO and ICO: A tale of two damping regimes

New methods have been developed in recent years to controllably synthesize nanocrystals of several common doped metal oxides, including ITO,[19,25,82] AZO,[13] ATO,[83] and ICO.[20] In addition, recent work has also demonstrated colloidal synthesis of doped transition metal oxides like Cs_xWO_3[45] and $Nb-TiO_2$.[26] Here we focus on comparing damping of the LSPR in ITO and ICO because they illustrate two contrasting damping regimes that lead to distinctive differences in the shape of the plasmon resonance peak.

Colloidally synthesized nanocrystals of ITO demonstrate effective aliovalent doping as well as the importance of compensating defects. While doping can be varied between 0 and ~20 cat. % Sn, typically less than 70% of Sn atoms incorporated in the lattice are activated to contribute a free electron. For higher doping levels this activation level drops due to the increasing formation of stable compensating defects. Nonetheless, free electron concentrations over 1×10^{21} cm^{-3} have been reported in ITO nanocrystals, leading to strong LSPR absorption in the NIR (See Figure 2.4.

6a). When considered alongside the relatively low dielectric background of ITO ($\varepsilon_\infty = 4$)[84] the rich doping chemistry in these ITO nanocrystals has facilitated detailed study of frequency dependent damping in LSPRs. Free electron concentration can also be modulated electrochemically in ITO nanocrystals, allowing the LSPR to be actively tuned across the NIR.[29]
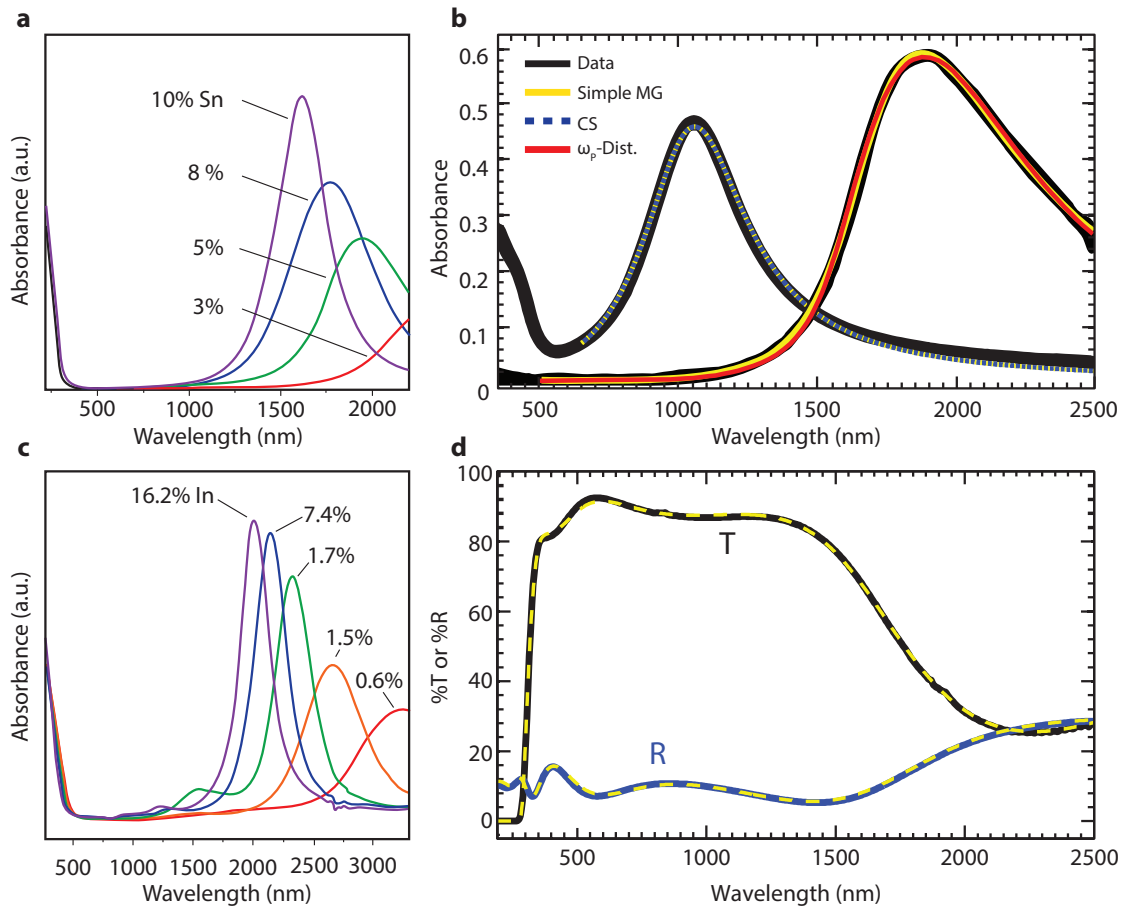
Figure 2.4.6. (a) Absorbance spectra for nanocrystals of ITO with increasing doping levels, (b) Drude modeling of ITO and Cu₁.₈₅Se nanocrystal dispersions with the MG-EMA, including extensions to account for capping ligands and a Gaussian distribution of doping levels, (c) absorbance spectra for nanocrystals of ICO with increasing doping levels, and (d) transmittance and reflectance spectra and Drude model fits for ITO nanocrystal thin films. (a-c) Reprinted with permission from refs [19,20,55]. Copyright 2009, 2012, 2013 American Chemical Society. (d) Reprinted with permission from ref [58]. Copyright 2012 AIP Publishing LLC.

Mendelsberg, et al. applied the Drude model to study dispersions and films of ITO nanocrystals.[58,85] The Maxwell-Garnett EMA (MG-EMA),[86] which is valid for particle dispersions that do not experience near-field electronic interaction, was used to fit extinction spectra collected from dilute dispersions of ITO nanocrystals, as well as nanocrystals of $Cu_{1.85}Se$, another important plasmonic semiconductor (Figure 2.4.6b).

Due to a high dielectric background ($\varepsilon_\infty = 10$), ionized Cu vacancies in $Cu_{1.85}Se$ are effectively screened even above ω_P. This leads to frequency-independent

damping and, as a result, a highly symmetric LSPR. By contrast, ITO typically displays an obvious asymmetry in its LSPR lineshape due to frequency-dependent damping by ionized impurities, though some papers have reported more symmetric LSPRs (Figure 2.4.6a). This inconsistency between different syntheses of the same material suggests that underlying differences in defect chemistry and distribution may play an important role in determining the physics of plasmon damping in doped semiconductor nanocrystals.

Excellent fits to the LSPR spectra of ITO and $Cu_{1.85}Se$ were achieved and used to extract free-carrier concentration (from ω_P), optically derived DC mobility (from Γ), and volume fraction.[85] For both materials, the ligand shell was found to influence the LSPR only weakly due to the similarity of the dielectric constant between the particular ligands used and the solvent. This is not always the case and the ligand-shell should be accounted for when the ligand dielectric constant is appreciably different from that of the solvent. The ensemble variance in the plasma frequency was also calculated from the fits and found to be *σ = 1500 cm^{-1}* for ITO, more than 10 times the theoretical minimum derived from ideal Poissonian statistics for the distribution of Sn doping levels. Similarly, broad distributions of dopant populations have also been observed among individual AZO nanocrystals using energy dispersive spectroscopy.[13] Ensemble dopant inhomogeneity of this kind can lead to a small blueshift of the LSPR resonance as well as asymmetric broadening of the peak,[85] complicating the quantitative interpretation of asymmetric broadening due to frequency-dependent damping in the Drude model. Further study is needed to understand this variance, how it arises from the nanocrystal synthesis process, and how it correlates to the optical and structural properties of the nanocrystals themselves, motivating the need for single-particle optical measurements in the near infrared.

The MG-EMA was also used to extract detailed electronic properties from transmittance and reflectance spectra taken of dense films of ITO nanocrystals (Figure 2.4.6d).[58] The LSPR redshifts and broadens upon deposition in a densely packed film, as the far field interaction between nanocrystals becomes a relevant property of the dielectric medium. By fitting these spectra using a detailed optical model that accounted for the optical properties of the layer stack under illumination – *i.e.* both the glass substrate and the ITO film – and using several initial guesses for the fitting parameters, the Drude model was shown to give reliable results that were in good quantitative agreement with those extracted from spectroscopic ellipsometry (SE) data. The success of the MG-EMA in modeling dense films of ITO nanocrystals is particularly remarkable because near-field electronic coupling is not incorporated into this model. Such dense films, in which the volume fraction is above a threshold of $f_V = 0.33$, must normally be treated using an alternate EMA developed by Bruggeman[87] that accounts for exchange of electrons between particles. However, the Bruggeman EMA was unsuccessful in fitting spectra of ITO nanocrystal films, indicating that the nanocrystals are not strongly electronically coupled and suggesting the

presence of insulating barriers between adjacent nanocrystals. This observation has further implications for understanding hopping conductivity in ITO nanocrystals films, which is crucial for their application in devices, and how it relates to the underlying structural properties of the individual nanocrystals. It also serves as an excellent example of the rich information that can be gleaned from Drude analysis of the optical properties of semiconductor nanocrystals and nanocrystal films.

In contrast to NCs of ITO, indium-doped cadmium oxide (ICO) does not show the influence of ionized impurity scattering in its plasmon oscillation, even at high doping levels. Much like in $Cu_{1.85}Se$, cadmium oxide (CdO) has a high dielectric background ($\varepsilon_\infty = 10$), which leads to screening that is strong enough to hide ionized impurities even above ω_P. This has been demonstrated by application of the Drude model with a constant damping parameter to thin films of CdO and ICO.[59] Recent work has demonstrated the synthesis of ICO nanocrystals with doping between 0.6 cat. % In and 16.2 cat. % In.[20] For spherical particles, these nanocrystals show LSPRs that are symmetric, even for the most highly doped samples, consistent with the expectation of a constant damping parameter (Figure 2.4.6d). The strong screening of ionized impurities plays an important role in determining the quality factor of these nanocrystals, which lies between Q = 3.5 and 8.2, higher than values typically achieved in other semiconductors.

2.4.5 Conclusion and Outlook

While the chemistry and physics of colloidal plasmonic metal oxide nanocrystals have advanced markedly in recent years, many materials challenges and fundamental questions remain. In particular, the development of new materials that break fundamental performance limits and introduce shape effects in the LSPR represents an exciting new frontier. Furthermore, deeper understanding of the relationship between local structural details of nanocrystal lattices and surfaces and their optoelectronic properties will be crucial to the future advancement of both fundamental and applied aspects of this field.

The strong interplay between doping and compensation places an upper limit on the quality factor of LSPRs in ITO and the other common oxides that rely on aliovalent substitutional doping to achieve high carrier concentrations, including ICO and AZO. By contrast, materials that can achieve high carrier concentrations by alternative approaches to doping could provide an opportunity to break these performance limits. For example, recent work has demonstrated colloidal synthesis of cesium tungsten oxide (Cs_xWO_3) with strong, shape-dependent LSPR absorption in the NIR. For pseudospheres, the LSPR is found at ~1400 nm, significantly to the blue of LSPRs in other extrinsically doped oxide nanocrystal materials.[45] In highly faceted particles, multiple absorption peaks are resolved falling at wavelengths as short as ~900 nm. Defect chemistry and compensation mechanisms in doped transition metal oxides such as Cs_xWO_3

30

and Nb-TiO$_2$ have seen little investigation when compared to their main group counterparts, even in the bulk, motivating the pursuit of more fundamental studies. The further development of nanocrystals employing interstitial doping, especially in high dielectric background materials, could lead to dramatic enhancement of semiconductor nanocrystal LSPR quality factors.

Recent work on colloidal ICO nanocrystals[20] has demonstrated the prospect of exploring plasmonic shape-effects in metal oxide nanocrystals, a topic that has primarily been studied in metals[78,79] and copper chalcogenide semiconductors.[5,80,88–90] Spherical and small octahedral ICO crystals were observed to have a single LSPR peak while larger octahedral crystals showed two peaks. Shape effects were also recently observed in Cs$_x$WO$_3$ nanocrystals. Psuedospheres of Cs$_x$WO$_3$ showed a single LSPR resonance, while hexagonal prisms and truncated cubes showed clear evidence of multiple LSPR peaks.[45] Further experimental and theoretical investigation of these new nanocrystals and the dependence of their optical properties on shape and aspect ratio, as well as external factors like dielectric environment and applied electrochemical potential, will be important to fully understanding the influence of particle shape and anisotropy of the crystal lattice on plasmonic properties. For example, tungsten bronzes like Cs$_x$WO$_3$ are known to show anisotropic dielectric properties for different crystal orientations.[91] Further experimental and theoretical studies to understand the effects of such anisotropy on LSPRs in Cs$_x$WO$_3$ nanocrystals and other similarly anisotropic systems will be instructive.
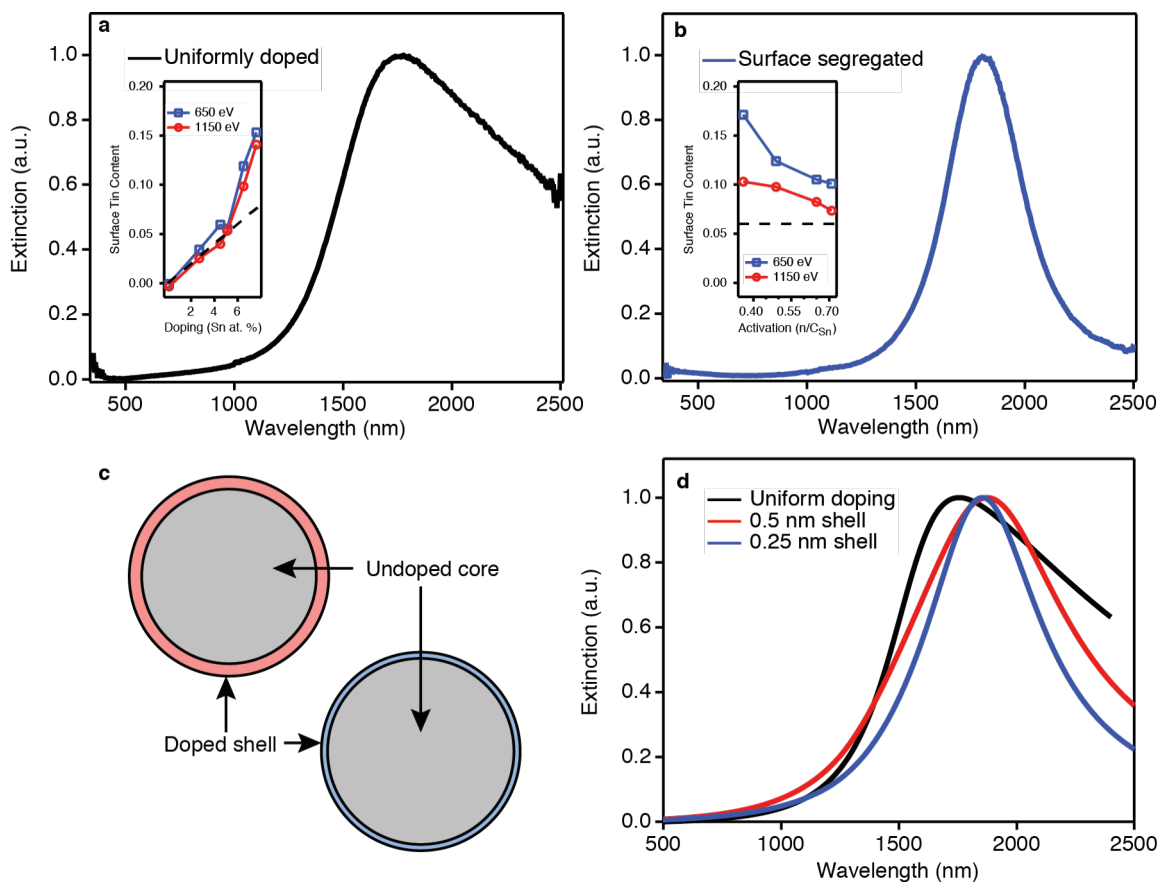
Figure 2.4.7. The influence of surface segregation on ITO LSPR lineshape. (a) Uniformly doped ITO shows asymmetry about the LSPR peak (inset: surface tin content determined by energy-dependent XPS). (b) ITO with surface segregated tin shows a symmetric LSPR peak (inset: measured surface tin content is above the average doping level indicated by the dotted line). (c-d) Simulated LSPR based on a core shell model reproduces the symmetry of the peak in (b). Figure adapted from ref [92]

The further investigation of structure-property relationships, particularly around doping, represents a frontier in fundamental understanding of semiconductor plasmonic nanocrystals, and will serve to inform both future synthetic directions and device development for plasmonic metal oxides. Because of the central role dopants play in determining the frequency dependent properties of LSPRs in metal oxides, dopant distribution, including radial distribution and clustering of dopants, should be a significant factor in the overall optoelectronic response. For example, in our recent work we demonstrated a strong correlation between surface segregation of tin dopants in ITO nanocrystals and the asymmetry the LSPR resonance.[92] Using energy-dependent x-ray photoelectron spectroscopy (XPS) (Figure 2.4.7 insets), it was demonstrated that nanocrystals with uniformly distributed dopants have asymmetric LSPRs, (Figure 2.4.7a) while those with surface segregated dopants have more symmetric LSPRs (Figure 2.4.7b). This

difference is justified by simulating the optical absorbance using a core shell structure in the Mie-Gans theory (Figure 2.4.7c-d). Moving beyond the current level of understanding in these areas will require further application of detailed structural analysis and sophisticated simulation and modeling techniques. Additional techniques with elementally specific physiochemical and structural resolution, like x-ray absorption spectroscopy, anomalous x-ray scattering, and neutron scattering, which have each been applied in detailed structural studies of bulk metal oxides, could be powerful probes of structure-property relationships in metal oxide nanocrystals. The development of new theoretical approaches to relate optical properties to atomic-level structural and electronic details, especially near nanocrystal surfaces, will be essential to complement these experimental approaches and inform synthetic routes to manipulating properties at the atomic scale.

The field of plasmonic metal oxide nanocrystals has experienced accelerating progress in the last five years, including a rapid growth in the number of colloidal syntheses of relevant oxide nanomaterials, the integration of these nanocrystals into devices, and preliminary explorations of the unique physics that becomes relevant at the nanoscale in this class of materials. Moving forward, the challenge will be extending these explorations to map the nuanced optoelectronic properties of these nanocrystals onto the details of their underlying physical and electronic structure. Doing so is likely to lead to further advances in fundamental understanding and will inform continuing development of new materials and applications for plasmonic metal oxide nanocrystals.

2.5 Transport in nanocrystal solids

2.5.1 Physical principles of conduction in nanocrystal solids

When discrete nanoparticles are assembled into a solid array, the electronic transport properties of the array differ fundamentally from the bulk properties of the material comprising the nanoparticles themselves. The overall transport properties will reflect the interplay of the underlying properties of the nanoparticles and the coupling nanoparticles with one another. Such systems can be treated in much the same way as granular metals, in which electrons must move and interact from one domain to the next as mediated by the grain boundaries. As such, the extensive literature on transport in granular metals is often applied to study conduction in nanoparticle solids.

When considering an assembly of discrete nanoparticulate components, there are three main physical parameters that determine the conductivity: exchange coupling energy, charging energy, and disorder. Exchange coupling energy describes the degree to which individual domains are electrically coupled by overlap of electronic wavefunctions. It is determined by the height and width of the potential barrier between particles and varies dramatically with changing

interparticle separation. Charging energy is the Coulombic energy cost of removing an electron from one particle and inserting it into another and represents and intrinsic barrier that must be overcome for conduction to occur. Disorder refers to differences in the energy levels of electrons from particle to particle, often due to inhomogeneity in size, shape, doping etc. within a nanocrystal ensemble. Since the probability of hopping is maximized when energy levels are aligned, disorder tends to reduce the overall conductivity.

2.5.2 Conduction mechanisms

Several different conduction mechanisms are possible in nanoparticle arrays depending on the relative strength of these effects. In systems with low electronic coupling, charges must "hop" from one particle to another by quantum mechanical tunneling. Depending on the degree of coupling, charging energy, and disorder, as well as the density of states, charges will either hop directly to their nearest neighbor or, if its is energetically favorable, to a particle farther away. The latter is known at variable-range hopping and has been observed in semiconductor nanoparticle arrays of several different materials. In contrast, highly electronically coupled nanoparticle arrays can establish metallic Bloch transport through minibands formed by overlapping electronic wavefunctions. Nanoparticle arrays typically undergo this transition from insulating to metallic behavior above a certain percolation threshold for the interparticle separation (typically above a packing density of 0.3) in the array.

The difference between each of these conduction mechanisms is most apparent when considering the temperature dependence of conductivity in the nanoparticle array. In general, insulating materials display decreasing conductivity with decreasing temperature while metallic materials show the opposite behavior. Similarly, nanoparticle arrays displaying hopping conduction will have exponentially decreasing conductivity with decreasing temperature, while metallic nanoparticle arrays will have increasing conductivity with decreasing temperature. For hopping conduction, the value of the exponent relating conductivity to temperature is related to the specific type of hopping (e.g. nearest-neighbor, VRH, etc.).

Conduction in nanoparticle arrays is treated thoroughly in reviews by Talapin *et al.*[18] and Zabet-Khosousi et al.,[93] to which the reader is referred for detailed discussion of the nuances of transport in these complicated systems.

2.5.3 Conduction in ITO nanocrystal films

Measurements of the resistivity of ITO nanocrystal films prepared similarly to those studied in these films show evidence of hopping conduction, displaying increasing resistivity (decreasing conductivity) with decreasing temperatures (Figure 2.5.1) despite having high packing densities on the order 0.6.[58]This

observation is further corroborated by the modeling of the optical properties of these films, which was only successful when using a model that assumes the particles are not electrically connected.[58]
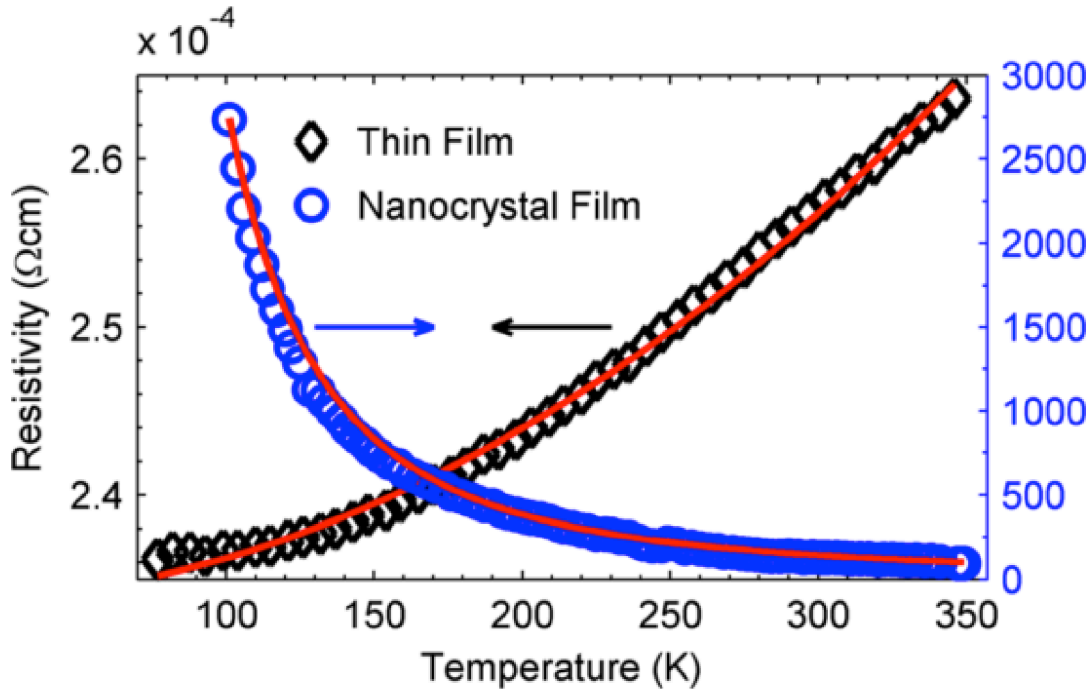
Figure 2.5.1 Resistivity of ITO nanocrystal films (blue) curve shows behavior characteristic of hopping conduction with respect to temperature, while thin film ITO shows typical metallic conduction. Reprinted from ref [58].

The observation of non-metallic hopping conduction in ITO nanocrystal films is somewhat surprising given that they have been processed to remove organic ligands, meaning the particles should be in nearly direct contact. It was hypothesized that there is some kind of insulating barrier between crystals.[58] The nature of this barrier will be explored and discussed further in Chapter 6.

3. Methodology

3.1 ITO nanocrystal synthesis and sample preparation

The colloidal synthesis of ITO nanocrystals was carried out according to adaptations of literature procedures[19,25,82] for each of the experiments discussed in this thesis. These syntheses were done by another student in the research group, and thus the details of the theory and practice of colloidal nanocrystal synthesis are beyond the scope of this work. However, the details of the chemistry involved in each specific synthesis are cataloged in the appendix.

Samples were generally prepared by either drop-casting or spin coating from solution onto flat substrates of glass or silicon. These substrates were cleaned rigorously by successive sonication in Hellmanex soap (followed by copious rinsing), acetone, and isopropanol. This substrate cleaning recipe was found to allow deposition of films of reproducible quality and properties. The details of post-deposition film processing for individual experiments are discussed within each chapter.

3.2 Primary experimental techniques

3.2.1 UV-Vis-NIR spectroscopy

Optical characterization of ITO nanocrystals across the ultraviolet, visible, and near-infrared (UV-Vis-NIR) frequency ranges is central to understanding the optoelectronic properties of ITO nanocrystals and the outcome of variations in synthetic methods and film processing procedures on the application of these materials in optical devices. Solutions and films of ITO nanocrystals were measured in transmission mode using a broadband light source and a UV-Vis-NIR spectrometer (ASD Inc/Panalytical). Data are presented as optical extinction, which is related to the transmittance, T, according to:

$$A = -log_{10}(T) \tag{3.2.1}$$

Since the reflectance of the films was not measured, the extinction captures both the absorption and scattering of light.

For solution measurements, ITO nanocrystals were suspended in tetracholoroethylene (TCE), which has high transparency in the spectral region of interest, and measured in a spectroscopic cuvette with a path length of 1 centimeter. Before measurement, the spectrometer was baselined using a cuvette filled with only TCE, so that only the extinction due to the nanocrystals was measured.

For nanocrystal film measurements, the glass substrate was positioned vertically, perpendicular to the collimated beam of light from the light source.

Again, the spectrometer was generally baselined against a blank piece of glass to eliminate extinction from the substrate.

3.2.2 Elemental depth profiling using energy-dependent x-ray photoelectron spectroscopy

X-ray photoelectron spectroscopy (XPS) is a widely used technique for the characterization of conductive materials. XPS uses the photoelectric effect, in which an incident photon leads to the ejection of an electron from a material (Figure 3.2.1), to study the energy levels of electronic states. As electrons are photoemitted, the leave the sample surface with a kinetic energy corresponding to the difference between the incident photon energy and the binding energy of the electron, minus the work function of the material. Because the core levels of individual elements have distinct electron binding energies, XPS is a probe with a high degree of elemental selectivity, allowing detailed characterization of the composition of a material within the probed volume.
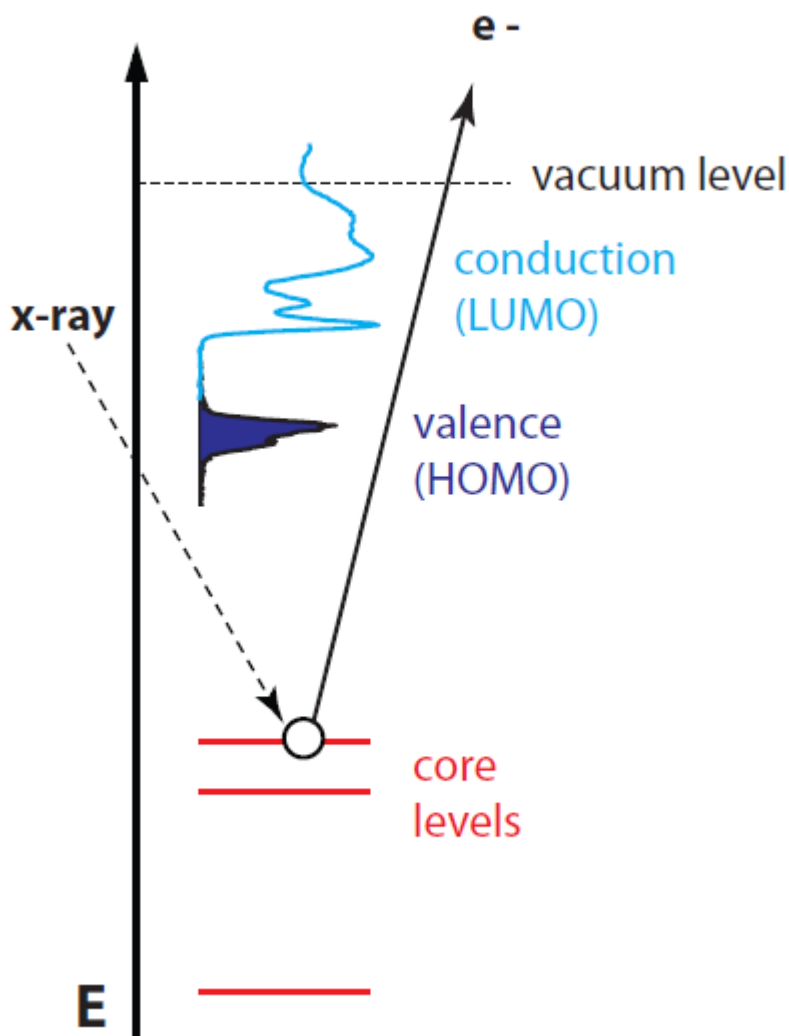
Figure 3.2.1 X-ray photoelectron spectroscopy involved photoexcitation of electrons occupying atomic core levels.

In addition to being sensitive to elemental composition, XPS is a highly surface sensitive probe. While soft x-ray photons penetrate hundreds of nanometers into a material, the probe depth is limited by the escape depth of electrons, which is orders of magnitude smaller. The escape depth is dependent on the kinetic energy imparted to the electron and follows the universal curve for electron mean free path (Figure 3.2.2a), with a minimum around 20 – 60 eV. Because of this dependence, photon energy can be used to tune the depth sensitivity of XPS, allowing depth-resolved characterization of elemental composition. (Figure 3.2.2b) For the photon energies used in this work, electron mean free paths were on the order of 0.7 – 1.5 nm.
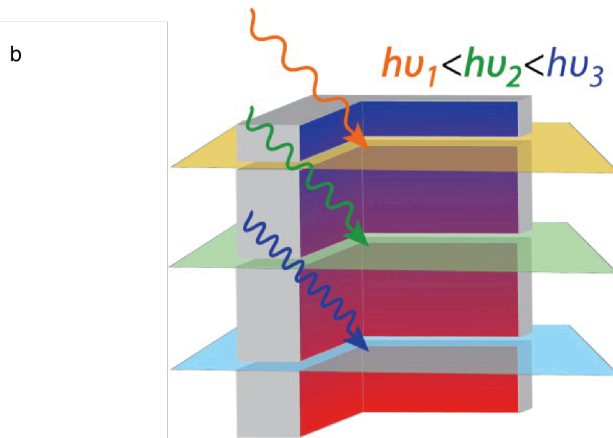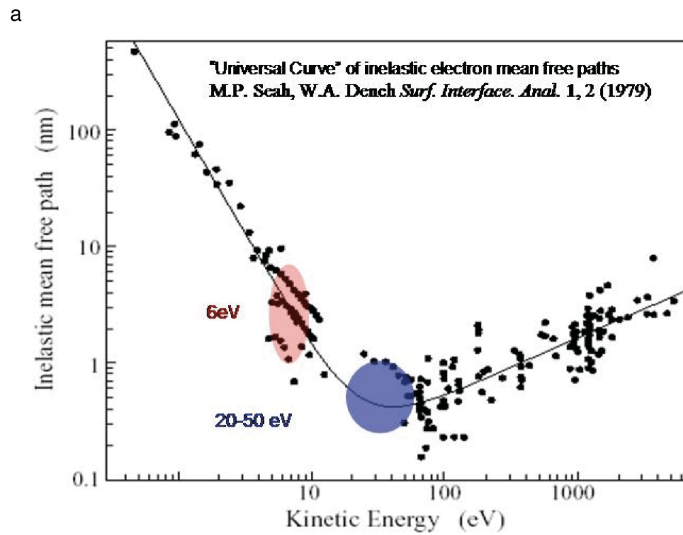
Figure 3.2.2 (a) Universal curve for the mean free path of photoexcited electrons [94] (b) Varying the photon energy allows selective depth profiling of materials using x-ray photoelectron spectroscopy. [95]

3.2.3 Van der Pauw resistivity measurements

Resistivity of ITO nanocrystals films was measured using a Hall effect measurement system (Ecopia) in a 4-point van der Pauw geometry. This geometry is useful for eliminating both the effect of contact and wiring resistance and in its ability to measure samples of arbitrary shape without precise knowledge of the sample geometry and location of the contacts.

In the Van der Pauw geometry, four contacts are placed on the perimeter of a sample of uniform thickness and the resistance is measured across eight different permutations of contact pairings (Figure 3.2.3). In this way, the internal consistency of the resistance measurement can be checked and any inhomogeneity in the sample is averaged out. Contacts should be as small as possible and should be placed directly on the perimeter of the sample.
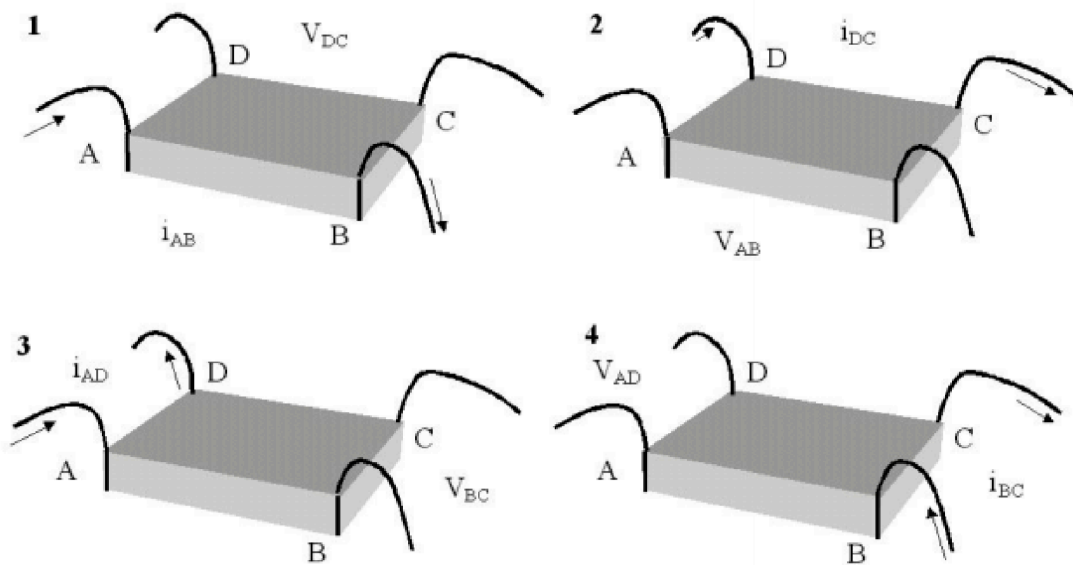
Figure 3.2.3 Four terminal contact permutations in the Van der Pauw geometry for resistance measurements. The remaining four permutations are simply reversals of the polarity of those pictured. Reproduced from ref. [96]

Since the Van der Pauw measurement return the sheet resistance of the film, accurate measurement of the film thickness is required to determine the resistivity of the film.

3.3 Additional Characterization Techniques

3.3.1 Inductively-coupled plasma optical emission spectroscopy

In order to effectively interpret observations of the structural properties of ITO nanocrystals, accurate knowledge of the elemental composition is needed to assess the degree of tin doping. Throughout this thesis, inductively-coupled plasma optical emission spectroscopy (ICP-OES) was used to perform detailed elemental analysis of ITO nanocrystal samples. In ICP-OES, the relative intensities of the atomic emission lines of specific elements are measured against known standards to determine the elemental composition to a high degree of accuracy.

To measure ICP-OES, samples are digested in concentrated acid to isolate their elemental components. The digested sample is then diluted with deionized water, nebulized, and excited with by a radio-frequency argon gas plasma. Atoms and ions in the sample will then emit radiation at characteristic frequencies with intensities proportional to their concentration in the sample.

Digestion of ITO samples was traditionally done in concentrated nitric acid. However, it was discovered during the course of this work that samples digested in nitric acid give somewhat erratic results that often underestimate the tin content in the sample, likely due to the formation of a tin nitrate complex that precipitates out of solution and is not captured by the instrument. After this discovery, digestion was carried out in hydrochloric acid, which was demonstrated to give repeatable results consistent with the expected doping levels based on the ratios of indium and tin precursors in the nanocrystal growth solution.

3.3.2 X-ray diffraction

X-ray diffraction (XRD) is a commonly used characterization technique that can be used to determine the crystalline phase and structure of a material of interest based on Bragg's law for diffraction of electromagnetic radiation from lattice planes. Conductive ITO is known to crystalize in the cubic bixbyite phase (Figure 3.3.1 a), which gives a characteristic diffraction pattern (Figure 3.3.1 b). All samples used in this study were verified to be bixbyite ITO. These measurements were conducted by another student in the group and detailed discussion of the theory of XRD is beyond the scope of this thesis.
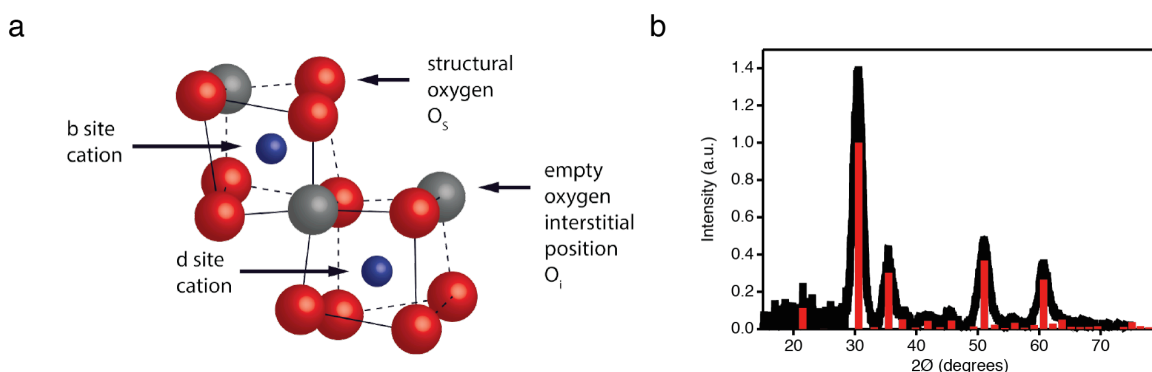
Figure 3.3.1 (a) Bixbyite crystal structure of indium oxide and (b) corresponding x-ray diffraction pattern.

3.3.3 Transmission electron microscopy and scanning electron microscopy

Electron microscopies are powerful tools to study the structure and morphology of nanomaterials. Transmission electron microscopy (TEM) was used to determine the size and shape of ITO nanocrystals, and to provide a secondary verification of their crystalinity in addition to XRD. Scanning electron microscopy (SEM) was used to characterize ITO nanocrystal film morphology and thickness, the latter in cross sectional mode. Beyond these basic characterizations, TEM and SEM were not used for more detailed studies, though this work has been reported elsewhere.

3.3.4 Fourier transform infrared spectroscopy

Due to its sensitivity into the mid and far infrared, beyond the range of most conventional optical spectrometers, Fourier transform infrared spectroscopy (FTIR) is a commonly used characterization method for identifying molecular vibrations and other infrared spectroscopic signatures. In this work, FTIR was used to verify the removal of organic ligands from ITO nanocrystal films by ligand exchange, ligand stripping, and low temperature annealing by observing the behavior of the C-H stretching mode at 2800 cm-1, which disappears after treating the ITO with these techniques (Figure 3.3.2)
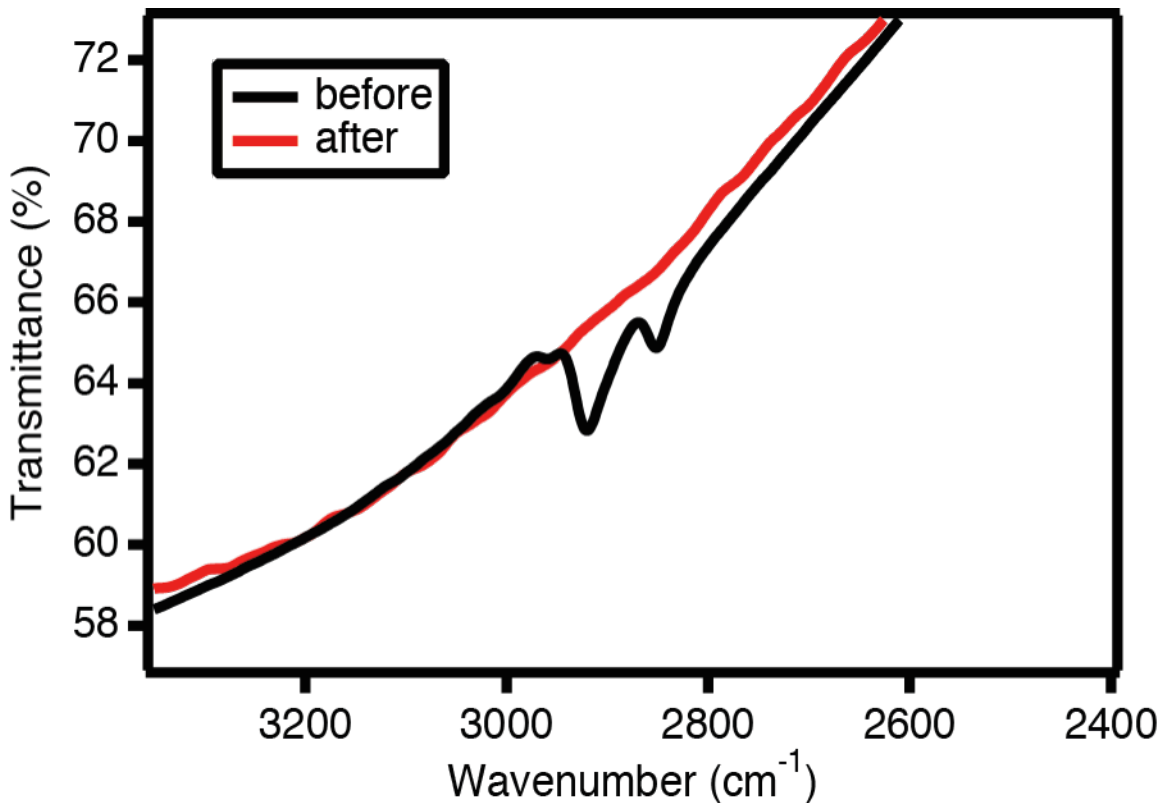
Figure 3.3.2 FTIR spectrum showing removal of ligands based on the C-H stretching mode at ~2850 cm^{-1}

3.4 Drude fitting and simulation of optical spectra with MATLAB

Optical extinction due to localized surface plasmon resonance (LSPR) in ITO nanocrystals was fit by the Drude model (See Section 2.3.2) using a MATLAB code that was developed by our group[85] and expanded for this work. The complete MATLAB fitting functions are supplied in the appendix.

The code utilizes a function that calculates the free electron absorbance based on the Drude dielectric function for ITO and can be readily adapted to employ the simple Drude model (frequency-independent damping) or the extended Drude model (frequency-dependent damping), and to treat core-shell geometries and sample inhomogeneity.[85] Based on the Drude dielectric function for individual particles, the overall dielectric function of the system is calculated within either the Mie theory or the Maxwell-Garnett effective medium approximation (See section 2.4.3). In general the code is versatile and easily adaptable to various fitting and simulation tasks.

The MATLAB function for the Drude absorbance can be used to either fit real data or to plot simulated data for a given set of parameters. Prior to fitting, one must supply the code with a set of initial guesses. In order to remove bias from the selection of initial guesses and explore a broad parameter space, a script was designed to generate random initial guesses within an assigned set of boundary conditions, which were selected based on physically reasonable limits. For simulation purposes, the code can be scripted to run through a large range of parameter values in order to study the sensitivity of the optical absorbance to changes in underlying properties like damping and carrier concentration.

4. Low temperature behavior of the LSPR in ITO nanocrystals

4.1 Temperature dependence of electrical resistivity

Electrical resistivity (ρ) is a measure of the ease with which electrical current can flow in a material. The resistivity of a solid is given by the formula:

$$\rho = \frac{1}{ne\mu} \qquad\qquad (4.1.1)$$

where *n* is the free carrier (electron or hole) concentration, *e* is the charge of an electron, and *μ* is the electronic mobility. Among these terms, both *n* and *μ* can depend on temperature. Because these quantities are directly related to the frequency and shape of the LSPR in a nanocrystal through the plasma frequency and damping parameter (See section 2.4.3), their temperature dependence must me considered when understanding the temperature dependence of the LSPR behavior. In both cases, the fact that ITO is a degenerately doped semiconductor is crucial to understanding its expected behavior with respect to temperature and how it contrasts with that in a conventional semiconductor.

4.1.1 Carrier concentration

The free carrier concentration will have very different behavior with respect to temperature in a metal when compared to a semiconductor or insulator.

By definition, an insulator or semiconductor will have an empty conduction band at zero Kelvin, corresponding to *n* = 0 and zero conduction. As the temperature is increased, thermal energy can give electrons enough energy to surmount the forbidden energy gap and populate the conduction band, allowing electronic conduction. This effect will depend on the size of the forbidden gap, as well as whether the material is doped or not, creating shallow defect levels just below the conduction band edge that are easily thermally populated.

By contrast, metals and degenerately doped semiconductors will retain the same carrier concentration in their conduction band at all temperatures, including at zero Kelvin. This is because the Fermi level in these materials sits within the band, which is only partly filled. However, more subtle effects must also be considered for both metals and insulators. In particular, as the temperature decreases, the lattice of a crystalline solid will contract, reducing its total volume. As the carrier concentration is a volumetric quantity, this phenomenon will increase the effective carrier concentration for a given number of electrons in the solid.[97]

4.1.2 Mobility

Electronic mobility is defined as the proportionality constant between a small external electric field and the steady-state velocity of a charge carrier in a solid. It

is classically determined by the rate of collisions experienced by an electron (or hole) that arrest, or "scatter", its forward momentum, described by the equation:

$$\mu = \frac{q\langle\tau\rangle}{m^*}$$

(4.1.2)

where μ is the mobility, q is the charge carried by the charge carrier, $\langle\tau\rangle$ is the average time between scattering events, and m^* is the effective mass of the charge carrier.

Scattering of charge-carriers in a semiconductor like ITO arises primarily due to phonon scattering and impurity scattering. Phonons are quantized lattice vibrations in a crystalline solid. These vibrations locally distort the potential energy landscape through which a mobile charge carrier is moving, changing its momentum. As temperature increases from zero, the population of phonons increases as the thermal energy in the solid grows. Thus, phonon scattering has a strong temperature dependence. In semiconductors, where electrons follow Maxwell-Boltzman statistics, the rate of phonon scattering is proportional to $T^{3/2}$ for the most common scattering mechanism.[98,99] In metals and degenerate semiconductors, which follow Fermi-Dirac statistics, the rate of phonon scattering is proportional to T^1.[98]

Impurity scattering occurs when a charge carrier interacts with an ion or atom that is not part of the original host material. In semiconductors, such impurities are most commonly the dopant ions that are deliberately inserted in the host lattice in order to introduce excess charge carriers. Because they are charged impurities, ionized dopants can interact with charge-carriers through the Coulomb force. Here, again, the temperature dependence of scattering depends on thermodynamics: in conventional semiconductors, ionized impurity scattering takes on a $T^{3/2}$ dependence, while in degenerately-doped semiconductors ionized impurity scattering is temperature independent.[98]

In the case of nanomaterials, one must additionally consider the influence of surfaces as scattering centers for electron motion, particularly when the dimensions of the nanoparticle are on the order of, or smaller than, the bulk mean free path of charge carriers. For the nanocrystals studied in this thesis, which are all smaller than ~12nm in diameter, this is certainly a relevant regime as bulk ITO typically displays mean free paths on the order of several tens of nanometers. In a metal or degenerately doped semiconductor, electron-surface scattering can be approximated using a simple semiclassical relation based on the Fermi velocity of electrons:[60]

$$\tau_S^{-1} = A\frac{v_F S}{4V}$$

(4.1.3)

where τ_S is the average surface scattering time, v_F is the Fermi velocity, and S and V are the surface area and volume of the nanoparticle, respectively. This equation can be understood simply as the average time with which a given electron will traverse the particle and collide with the surface. Surface scattering of this kind is also temperature independent.

In addition to phonon scattering, ionized impurity scattering, and surface scattering at the nanoscale, several other scattering mechanisms contribute to the electronic mobility of a material. These include scattering from neutral impurities and other point defects like dislocations, electron-electron scattering, intervalley scattering and radiative relaxation. As these are processes are known to be of negligible importance in determining electronic mobility in ITO, they will not be discussed in detail here, except in reference to specific examples below.

4.1.3 A note on Mattheissen's Rule and resistivity

Mattheissen's rule, developed by Augustus Mattheissen in 1864, states that the influence of multiple scattering processes on overall electrical mobility can be well approximated by equating the inverse of the overall mobility with the inverses of each individual contribution. For example, the total mobility μ_{tot} for a material with contributions from phonon scattering, μ_{phonon}, and ionized impurity scattering, μ_{ion}, can be computed according to:

$$\frac{1}{\mu_{tot}} = \frac{1}{\mu_{phonon}} + \frac{1}{\mu_{ion}} \tag{4.1.3}$$

For this reason, resistivity, which has an inverse relationship to mobility, is a convenient quantity for comparing the combined influence of various scattering mechanisms along with free carrier concentration. For the case of the example above, the resistivity would follow the relationship:

$$\rho_{tot} = \rho_{phonon} + \rho_{ion} \tag{4.1.4}$$

4.1.3 The Bloch-Gruneisen equation and temperature dependence of resistivity in bulk and thin film ITO

Based on the temperature dependence of carrier concentration and electrical mobility discussed above, the temperature dependence of resistivity due to phonon-scattering in metals and degenerately doped semiconductors can be described by the Bloch-Gruneisen equation:[98]

$$\rho(T) = \frac{AT^5}{M\theta_D^6} \int_0^{\theta_{D/T}} \frac{x^5 dx}{(e^x - 1)(1 - e^{-x})} \tag{4.1.5}$$

48

where T is the temperature, A is a constant, M is the atomic mass of the metal or degenerately doped semiconductor, and Θ_D is its Debye temperature. Physically, the Debye temperature can be understood as the temperature below which all phonon modes are "frozen out," *i.e.* the thermal energy present in the system is smaller than the lowest energy phonon mode. For typical metals the Debye temperature ranges from ~200 K to ~450 K, while in ITO it is around 1000 K.[100]

In its thin film and bulk forms, ITO typically behaves like a metal according to the Bloch-Gruneisen equation. At low temperature, the resistivity is nearly constant. As the temperature rises, the resistivity begins to increase around 100 K, eventually reaching a regime of linear increase around 200K (Figure 4.1.1 a). This increase in resistivity is due to the T^{1} decrease in mobility, while the carrier concentration remains constant throughout this regime (Figure 4.1.1 b). Between 100K and 300K, very close to the temperature range relevant for the experiment discussed below, the thin film resistivity changes by ~ 5-15% relative to its value at room temperature. It should also be noted that behavior anomalous to that expected from Bloch-Gruneisen conduction has been observed in both ITO thin films (Figure 4.1.1 c)[101] and nanowires (Figure 4.1.1 d, inset),[100] and attributed to localization effects and scattering off dynamic defect states due to the non-magnetic Kondo effect, respectively. The former observation occurs below 150K, while the latter only occurs below ~10 K. In both cases, the observed increase in resistivity is on the order of 1% relative to the room temperature resistivity.
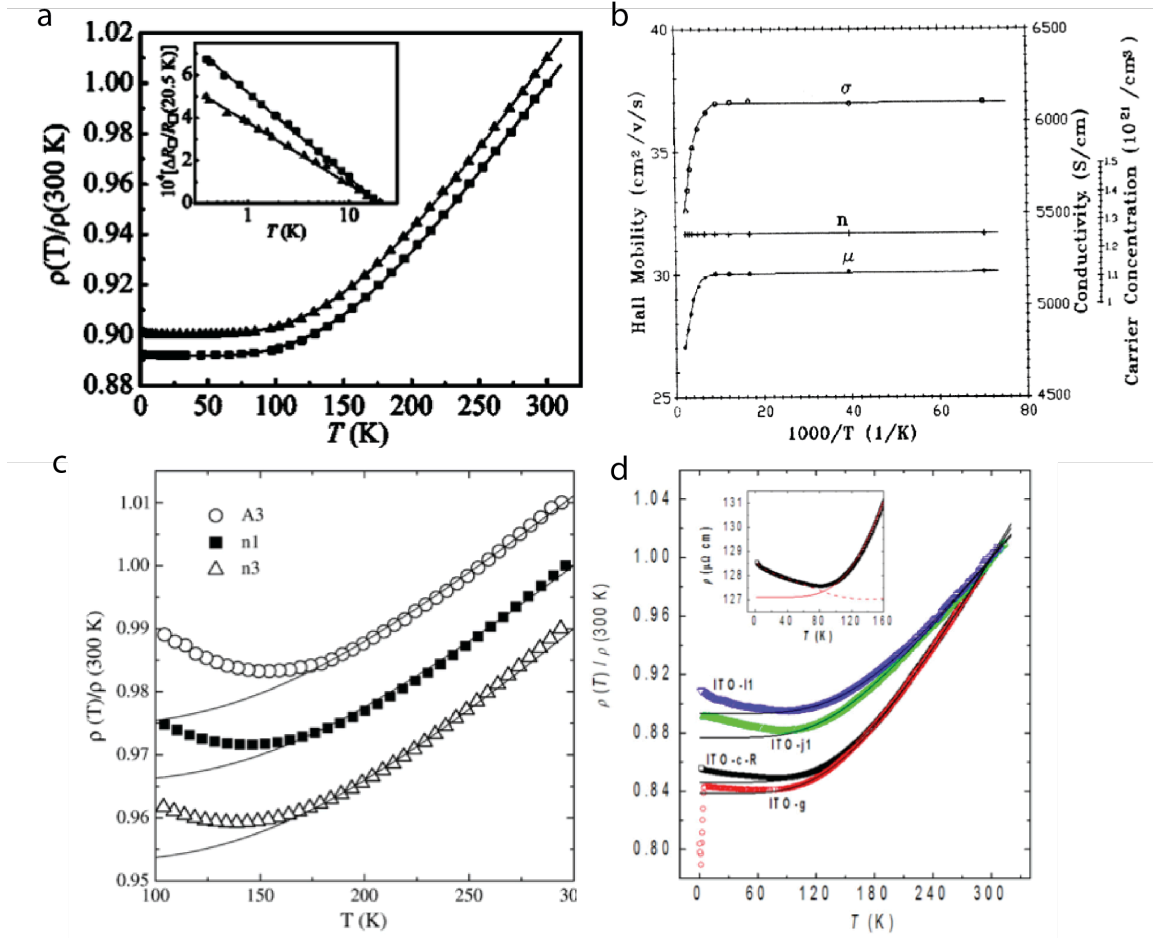
Figure 4.1.1. Temperature dependence of resistivity in thin film ITO. (a) Resistivity of 125 nm (squares) and 240 nm (triangles) ITO thin films vs temperature and (b) temperature dependence of conductivity (σ), carrier concentration (n), and mobility (μ) for a 125 nm ITO thin film. Reprinted from refs [98,100–102]

4.1.4 Temperature dependence of LSPR in metal nanocrystals

Several theoretical and experimental studies have been conducted in recent years on the temperature dependence of LSPRs.[57,60,97,103–106] Often, the goal of these works is to better understand the physical mechanisms underlying plasmon *dephasing* in metal nanocrystals, i.e. by what processes are is the resonant oscillation of the electron cloud perturbed and on what time scales. *Dephasing* can be thought of as the quantum corollary of *damping* in a classical resonant process and can be quantified based on the optical linewidth of the LSPR. Generally speaking, most metals show a narrowing of the plasmon linewidth (Figure 4.1.2 a and b) associated with reduced damping (*i.e.* slowed dephasing) due to electron-phonon and electron-electron scattering at lower temperatures, in correspondence with the expected trends in electron mobility and resistivity.

No such study has been conducted on LSPRs in plasmonic nanocrystals of ITO, however, based on the transport behavior of bulk, thin film, and nanowire ITO, one would expect to observe Bloch-Gruneisen behavior at higher temperatures (above ~150K), with decreasing LSPR linewidths as temperature decreases. As described above, the reported behavior of ITO at lower temperatures is less consistent.
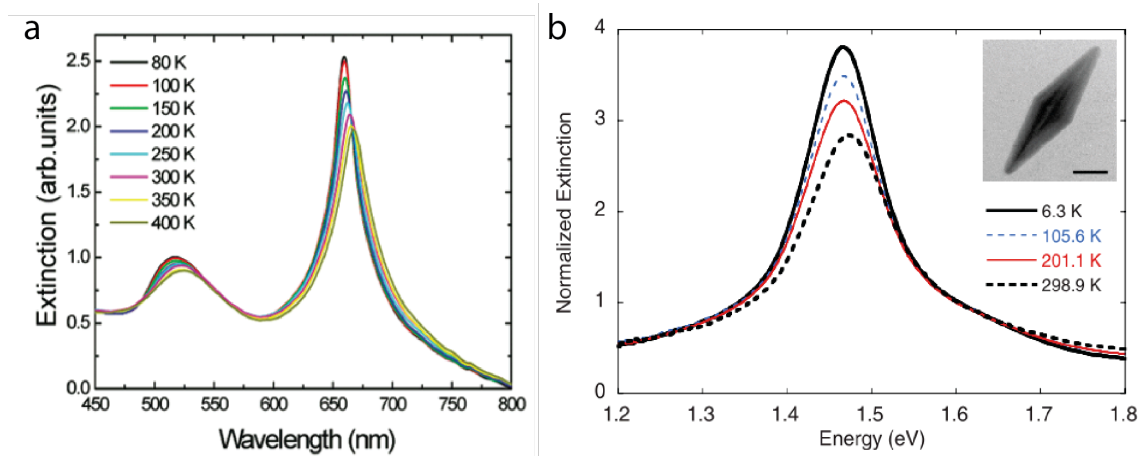
Figure 4.1.2 Temperature dependence of LSPRs in metal nanostructures. Both gold nanorod arrays (a) and nanopyramids (b) show decreasing linewidth and increasing intensity at lower temperatures. [permissions]

4.2 Methods

Typically, the optical properties of plasmonic nanocrystals are studied in one of two forms: in solution at dilute concentrations or in a dense film deposited on a transparent substrate. However, neither of these arrangements is suitable for low temperature optical measurements of the inherent plasmonic properties of the nanocrystals. In solution, one is limited by the freezing point of the solvent used. For the most common solvents, the freezing point is greater than 150K, preventing measurement at sufficiently low temperature. In the case of a dense film, one must contend with the effects of coupling between the dipolar LSPRs of the nanocrystals, which will alter the shape of the LSPR and potentially introduce additional temperature-dependent effects, complicating the interpretation of data.

In order to best conduct the experiments at hand, one requires a transparent medium that allows for a dilute concentration of nanoparticles, but does not change its optical, dielectric, or mechanical properties over the temperature range of interest. To accomplish this, nanocrystals were dispersed at low concentrations in transparent polymers.

4.2.1 NC dispersion in polymer

Several polymers that meet the optical and mechanical requirements described above are also soluble in the same solvents typically used to dissolve ITO nanocrystals (capped with organic ligands). These include, but are not limited to, polyvinyl butryal(PVB), ethylene vinyl acetate (EVA), and poly(methyl methacrylate) (PMMA). After some optimization, PVB was chosen for the best combination of optical transparency over the visible to near infrared (vis-NIR) range of the spectrum, low-temperature stability, and mechanical properties.

To create samples for the measurement, 4.5 nm diameter ITO nanocrystals capped with oleylamine or oleic acid ligands were transferred from hexane to toluene. PVB was then added to the toluene until it was well dissolved, giving a semi-viscous liquid. The solution of nanocrystals and PVB was then dropcast on a level surface onto thin circular glass substrates and allowed to dry overnight in a fume hood. The resulting product was a thin (~40 μm), flexible, and transparent disc of PVB with a low concentration of ITO nanocrystals suspended within (Figure 4.2.1 a). The underlying glass substrate was removed by bending the PVB disc until the glass broke and peeling the glass away from the polymer. These PVB discs showed greater than 90% transparency over most of the vis-NIR range, with a small amount of absorption above 2400nm (Figure 4.2.1 b)

a

b
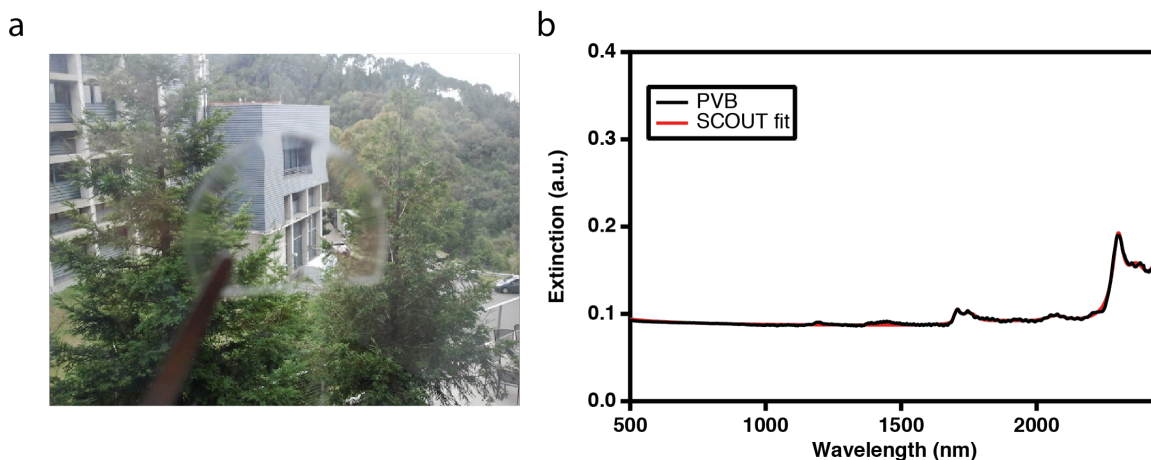
Figure 4.2.1 Properties of PVB-nanocrystal samples. (a) ITO nanocrystals were suspended in highly-transparent PVB discs and (b) showed limited optical extinction over the vis-NIR specral region.

4.2.2 Linkam Cell optical transmission set up

The temperature-dependent optical properties of ITO nanocrystals in PVB were measured in transmission mode using a variable temperature stage designed for use with optical microscopes (Linkam).The Linkam cell allows measurement between liquid Nitrogen (77K) and 450 °C (723 K), though the measurements were limited to 373 K at the high temperature end by the melting point of PVB.

Samples were placed horizontally on the stage within the cell, which was mounted on fixed rails (Figure 4.2.2 a). Light from the lamp was directed vertically through the sample through a small opening in the Linkam cell using fiber optic cables and plano-convex lenses (Figure 4.2.2 b).
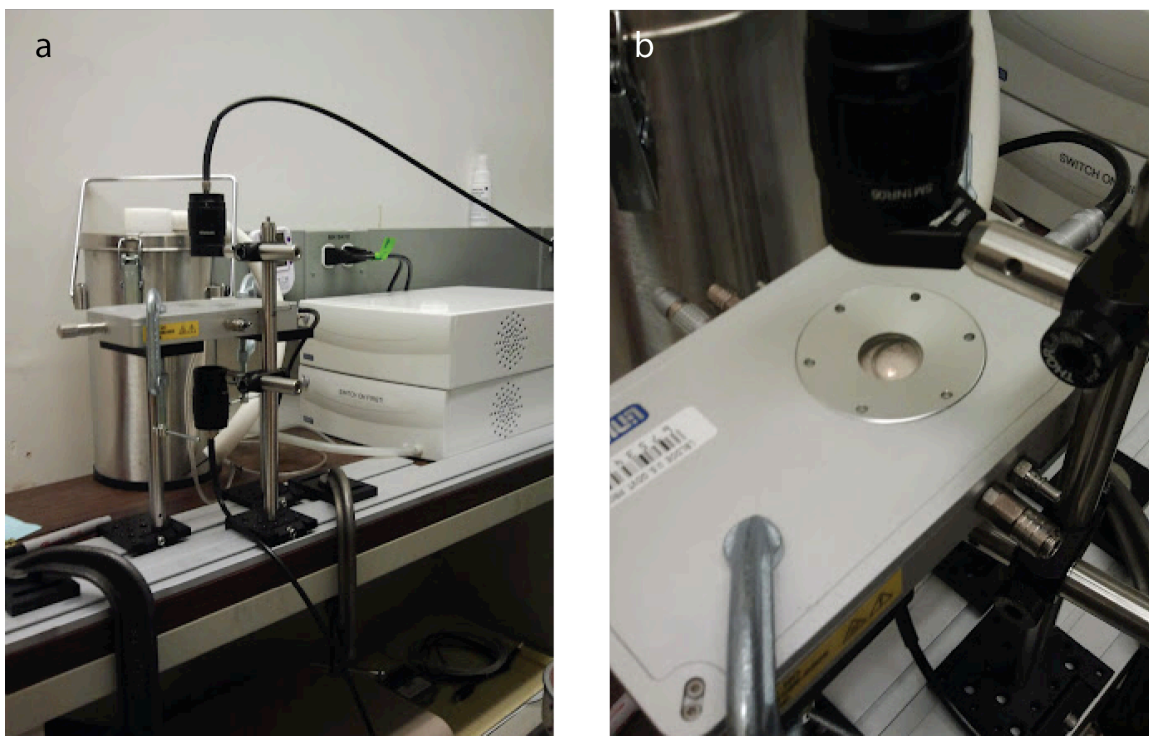
Figure 4.2.2 Experimental setup for temperature dependent optical measurements.

4.2.3 Background subtraction and issues with condensation of water

In order to attain spectra appropriate for full-stack modeling using SCOUT, the instrument was baselined with the beam traveling through the stage without a sample. Then, separate spectra were recorded for blank PVB and ITO nanocrystals in PVB.

During the course of measurements, it was discovered that there were serious issues with condensation of water on the glass windows of the Linkam cell, causing severe broadband scattering of light below 180 °C. Due to the fact that the cell is intended for use in microscopes, it is designed to only mitigate condensation on the top window, through which a microscope objective would observe the sample. This is accomplished by directing a stream of dry, room-temperature nitrogen gas emanating from the liquid nitrogen dewar at the window. The bottom window, which is intended only for backlighting a

microscope sample, has no such system in place, and was visibly coated with a thick layer of condensation and, eventually, frost, at low temperatures.

In order to rectify this flaw, the tubing directing nitrogen at the top window was split and a second stream was directed at the bottom window, including a makeshift chamber for containing the low humidity nitrogen atmosphere (Figure 4.2.3 a). However, though the condensation was significantly reduced with both windows set up in this way, it still increased the baseline absorbance of the cell at low temperatures; while the windows looked visibly clear, sufficient for use with microscopes, there was still some scattering of light by a small amount of condensed water (4.2.3 b). For this reason, it became necessary to measure the extinction of the PVB blank at all measured temperatures and use these spectra for background subtraction. These fully background subtracted spectra could then be modeled in MATLAB instead of SCOUT (See Section 3.4). In this way, the spectra could be fit successfully, despite the influence of condensation.
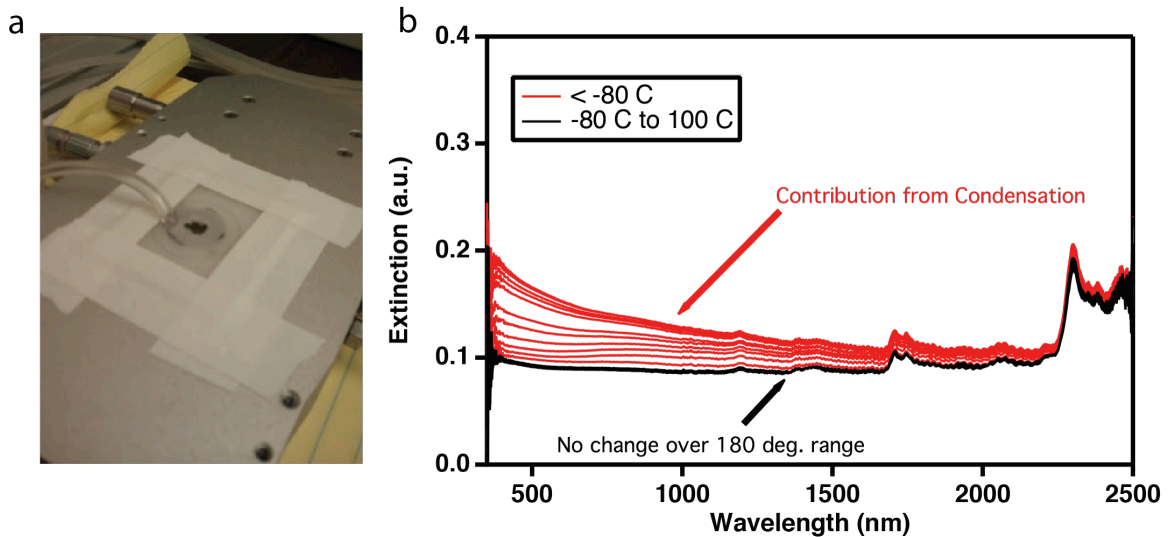
Figure 4.2.3 (a) Chamber attached to bottom of Linkam cell to mitigate condensation. Dry nitrogen gas enters the chamber through the tube on the left. Light passes through the small opening in the center. (b) Contribution to the optical extinction from condensation below – 80 °C depicted in red. These spectra were subtracted from the ITO nanocrystal extinction data at each temperature to obtain background subtracted spectra for fitting with SCOUT.

4.2.4 Drude modeling using MATLAB

Optical spectra for ITO nanocrystals were fit at each temperature using MATLAB (See section 3.4.2) using an optical model derived from refs [58,85], based on frequency dependent damping of ITO in a Maxwell-Garnett effective medium approximation. Fits were conducted using a minimum of 5 randomly generated sets of initial guess parameters.

4.3 Results and discussion

4.3.1 Vis-NIR results

The ITO nanocrystals dispersed in PVB showed subtle changes consistent with the expected behavior as temperature was decreased from 100 °C (373 K) to -190 °C (83K) (Figure 4.3.1). The LSPR peak amplitude increased and blueshifted by approximately 10 nm over the temperature range studied. However, as can been seen in the inset to figure 4.3.1, which plots the normalized extinction, the peak width did not change noticeably.
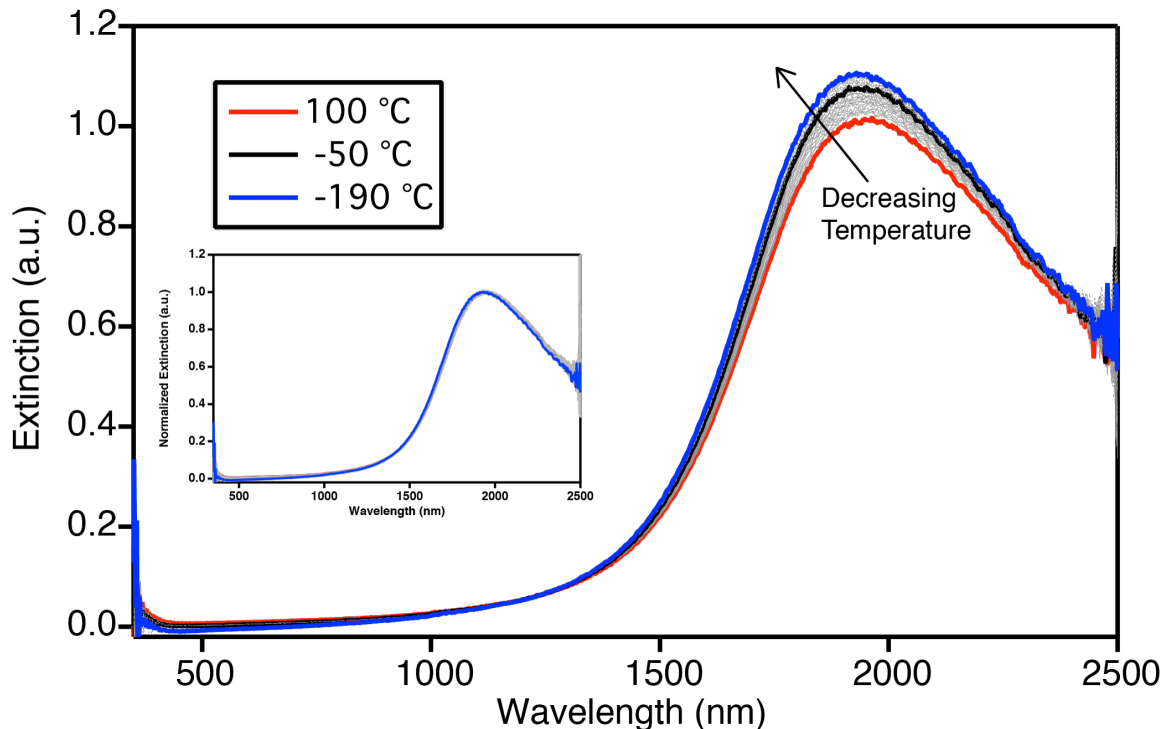
Figure 4.3.1 Temperature dependence of the LSPR in ITO nanocrystals.

4.3.2 Drude modeling results and comparison to thin film ITO

The changes described in section 4.3.2 were quantified using the drude model. The LSPR peak position, amplitude, and width are all related to the plasma frequency and damping parameter in the Drude model. Thus, free carrier concentration and mobility, which can be extracted from these quantities in the model, can be used to discuss the subtle changed in peak shape.

Over the temperature range studied, the electron concentration (Figure 4.3.2, black squares) showed a slight increase with decreasing temperature. This change is attributed to thermal contraction of the lattice: as the lattice shrinks with decreasing temperature, the overall carrier density increases accordingly. One

can quantify the influence of thermal contraction on the carrier concentration according to the formula:[97]

$$\omega_P(T) = \frac{\omega_P(T_0)}{\sqrt{1 + 3\gamma(T - T_0)}} \tag{4.3.1}$$

where ω_P is the plasma frequency, T is the temperature of interest, T_0 is room temperature, and γ is the thermal expansion coefficient. Since ω_P^2 is proportional to n, the carrier concentration will scale by $1/(1+3\gamma(T-T_0))$ relative to the value at room temperature. Based on the observed trend, this formula give a thermal expansion coefficient of 17.3×10^{-6} K^{-1} for the ITO nanocrystals below, which is slightly higher than the result reported for thin film ITO. This result also confirms that our ITO nanocrystals are well-behaved degenerate semiconductors, showing no effect of "freeze out" at low temperatures.
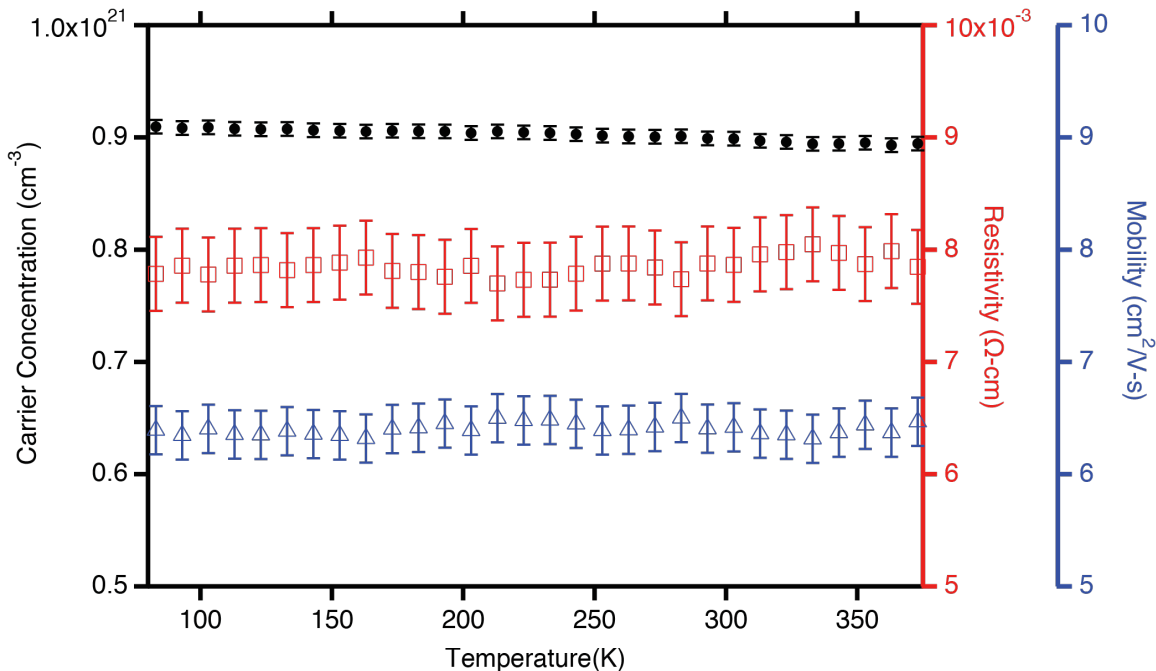
Figure 4.3.2 Drude results for the electron concentration (black squares), electron mobility (blue triangles), and resistivity (red squares). Error bars were calculated based on fitting to spectra measured on multiple different days and likely arises due to subtle differences in background subtraction caused by the condensation of water discussed above.

In contrast to the electron concentration, the electronic mobility shows no appreciable trend within the error bars for this measurement (Figure 4.3.2, blue triangles). This result indicates that the strength of phonon-scattering in these nanocrystals is below or on the lower end of what is expected for ITO. Given that the error bars for mobility are ~6% of the total value, one would expect to see a

change in mobility on the order of what is typically observed for ITO (see Section 4.1.3), should it exist.

The weak or non-existent influence of phonon scattering in the temperature range investigated could be due to the strong influence of surface scattering in particles of this size. For thin film ITO, one can calculate the mean free path for phonon scattering at a given temperature based on the difference between the total resistivity and the resistivity at low temperature, where there are no phonons, using the formula:

$$d = \frac{m^* v_F}{ne^2 \rho}$$

(4.3.2)

where d is the mean free path, m^* is the effective mass of the electron in the crystal ($0.4m_e$ in ITO[84]), v_F is the Fermi velocity, n is the electron concentration, e is the elementary charge, and p is the resistivity.

Based on the literature, for ITO at 100 °C, the phonon-derived resistivity is ~0.2 to 0.5 x 10^{-4} Ω-cm, corresponding to mean free paths ranging from ~65 nm to ~25nm. Given that our particles are 4.5 nm in diameter, one would thus expect the probability of scattering from phonons to be greatly reduced relative to thin film or bulk ITO, with temperature independent scattering mechanisms like surface scattering and ionized impurity scattering being dominant.

4.4 Conclusion

4.4.1 Validation of connection between bulk and nano properties

Studying the underlying optoelectronic properties of ITO nanocrystals by measuring and modeling their plasmonic optical properties with respect to temperature, has allowed direct comparison to the bulk and thin film phases. Based on the results obtained in the experiments above, one can conclude that ITO nanocrystals have properties similar to thin film ITO and are well-behaved degenerate semiconductors. The ITO nanocrystals have internal resistivities that are about one order of magnitude lower than those found in the highest quality thin film ITO. This difference is likely due to the influence of surface scattering of electrons in the nanocrystals, which have a high surface to volume ratio.

4.4.2. Limitations and suggestions for future work

This experiment was fundamentally hampered by the influence of condensation of water on the window of the temperature cell, which was likely responsible for the size of the error bars in the resistivity measurement. One could reduce these error bars by designing a better system for mitigating the effect of condensation on the window, allowing more detailed study of the trends in the temperature

dependence of mobility and resistivity. By doing so, one could potentially quantify the degree to which phonon scattering is reduced or suppressed in these nanocrystals.

In addition, this experiment would benefit from expansion of the temperature range studied at both the high and low temperature ends. At high temperature, one would expect any phonon scattering to eventual contribute appreciable increase in the electron mobility, especially when approaching the Debye temperature of ~1000K. This measurement will require a transparent substrate with a significantly higher melting point than the PVB used here. Alternatively, one could measure ITO nanocrystal films on quartz substrates to higher temperatures (The Linkam cell is capable of heating to 450 °C), though one would then have to contend with the additional dielectric effects present in a densely packed film. However, despite this additional complication, this may be the best route to a higher temperature measurement.

Measuring at low temperature, particularly at liquid helium cryogenic temperature, would further confirm the degenerate behavior of the ITO nanocrystals. One would expect that the carrier concentration, and hence the frequency for the LSPR would remain largely the same down to absolute zero. In addition, these temperatures would allow observation of the low-temperature scattering effects that have been observed in other ITO nanomaterials (see section 4.1.3 above), opening these phenomena to studies with respect to doping level, doping distribution, nanocrystal shape and size, etc.

5. The influence of dopant distribution on the plasmonic properties of indium tin oxide nanocrystals

5.1 Introduction

Colloidal synthesis of nanostructures based on doped oxides has emerged in recent years as a route toward highly tunable plasmonics.[5,6,11,13,19,20,29,83,107] However, in contrast to their metal counterparts, there is little fundamental understanding of the optoelectronic properties of plasmonic semiconductor nanomaterials.[10–12,108] In particular, the ability to reliably control doping and, in turn, free charge-carrier concentration, remains a challenge in these materials and is essential to their functionality as systems with modulable optical and electronic properties, including strong absorption and field enhancement due to localized surface plasmon resonances (LSPRs), optical transparency, and high electrical conductivity.

Of particular interest among the doped metal oxides is tin-doped indium oxide (ITO). Several colloidal syntheses have been developed for spherical ITO nanocrystals ranging in size from 3 nm to 15 nm and demonstrating chemically and electrochemically tunable LSPRs in the near infrared (NIR).[19,25,82,109,110] Because of its commercial relevance as a material used in displays, thin-film solar cells, and organic electronics, thin-film ITO has been the subject of intensive applications-oriented research for decades. However, little is known about the underlying mechanisms of doping and defect formation in colloidal ITO nanocrystals, and the relationship between structural properties like dopant distribution and compensation with the optical and electronic properties of these materials has not been explored. In addition, while detailed models have been developed to describe defect chemistry in thin film ITO,[31,35,36,48] these have not been verified in colloidally synthesized nanocrystals and are still debated even in the bulk and thin-film literature.

Herein, we investigate the relationship between the radial distribution of dopants and nanocrystal optoelectronic properties, including plasmon damping and dopant activation (*i.e.* the number of free electrons per tin ion). Using x-ray photoelectron spectroscopy (XPS) combined with careful characterization of the composition and optical properties of ITO nanocrystals, we demonstrate that nanocrystals with tin-rich surfaces exhibit reduced dopant activation. We suggest that this trend is due to the formation of electronic trap states, including those due to diffusion of compensating oxygen interstitial atoms, which can more readily form neutral complexes with tin that is situated near the nanocrystal surface. Based on fitting of the LSPR using the Drude model we also demonstrate that dopant distribution has an important effect on plasmon damping in this system, leading to symmetric, narrowed LSPR lineshapes in the case of surface segregated tin.

5.2   Experimental section

ITO nanocrystals were synthesized using adaptations of methods reported in the literature. Two series of samples were made: a doping series based on ref [19] comprising crystals with fixed size and varying doping levels (See Table I) and an activation series based on ref [25] comprising crystals with fixed size and doping, but demonstrating different degrees of dopant activation (See Table II). The salient differences between these two synthetic methods are in the precursors (indium acetate and tin ethylhexanoate v. indium acetylacetonate and tin bis(acetylacetonate) dichloride) and ligands (oleylamine and octanoic acid vs. only oleylamine), respectively. We observed large variances in dopant activation for the latter synthesis recipe.

Table 5.2.1. Sample details for doping series prepared by synthetic method from ref [19].

Sample	Size (nm)	Doping (Sn at%)	n_e x 10^{21} (cm^{-3})	Activation (n_e/C_{Sn})
D1	6.2	0.12 ± 0.1	0	-
D2	6.1	2.73 ± 0.03	-	-
D3	6.8	4.53 ± 0.55	0.913	0.67
D4	6	5.10 ± 0.57	1.03	0.67
D5	5.5	6.45 ± 0.90	1.12	0.57
D6	4.9	7.60 ± 0.80	1.0	0.43

Table 5.2.2. Sample details for activation series prepared by synthetic method from ref [25].

Sample	Size (nm)	Doping (Sn cat. %)	n_e x 10^{21} (cm^{-3}) from Drude	Activation (n_e/C_{Sn})
A1	9.6	5.63 ± 0.72	0.612	0.36
A2	8.7	6.97 ± 0.61	1.03	0.49
A3	10.8	6.40 ± 0.82	1.25	0.65
A4	8.5	5.34 ± 0.69	1.14	0.71

Particle size and structure were verified by transmission electron microscopy (TEM, See Figure 5.2.1a and Appendix 2) and x-ray diffraction (XRD, See Figure 1b and A2), while dopant incorporation was measured using inductively coupled plasma atomic emission spectroscopy (ICP-AES). For XPS measurements, the nanocrystals were spin-coated from a concentrated solution of 1:1 hexane:octane onto silicon substrates, yielding ~100nm thick films. In order to facilitate quantitative interpretation of surface-sensitive spectra and limit charging, the bulky organic capping ligands on these films were then exchanged with formic acid,[111] followed by a 30 minute anneal in flowing argon gas to decompose the remaining organic matter.
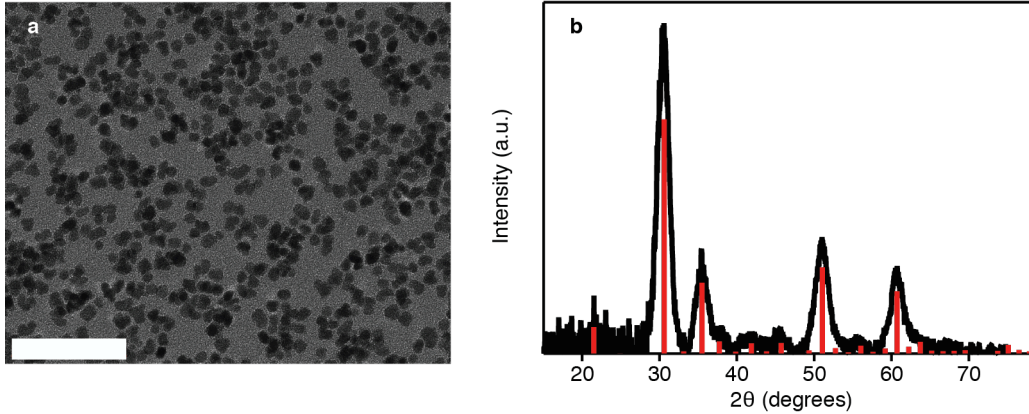
Figure 5.2.1. (a) Transmission electron micrograph (TEM) confirming pseudo-spherical morphology (scale bar is 50 nm) and (b) x-ray diffraction pattern confirming cubic bixbyite structure (reference pattern JCPDS 06-0416 is shown in red, data are from sample D6).

Optical measurements were made on dilute solutions of each series in tetrachloroethylene using a UV-VIS-NIR spectrometer (ASD Inc./PANalytical). All spectra were measured in transmission mode and are presented as optical extinction. These spectra were fit within a MATLAB code developed by our group[55] using an extended Drude model employing the Maxwell-Garnett effective medium approximation. This model allows extraction of free electron concentrations within each sample based on the Drude formula:

$$\omega_P{}^2 = \frac{ne^2}{m^*\varepsilon_0} \tag{5.2.1}$$

where ω_P is the bulk plasma frequency, n is the free carrier concentration, e is the elementary charge, m^* is the carrier effective mass ($0.4 m_e$ for ITO[84]), and ε_0 is the permittivity of free space. The extracted electron concentration was in turn used to determine the dopant activation in each sample by taking the ratio of the electron concentration to the tin dopant concentration. Tin concentration was calculated based on the density of ITO using the formula $C_{Sn} = 3[Sn] \times 10^{20}$ cm^{-3}, where [Sn] is the tin cation percentage, determined here by ICP-AES. Care was taken to perform Drude fitting using several randomly generated initial guesses to ensure convergence on reliable values with known error.[58]

XPS data were collected on beamline 10-1 at the Stanford Synchrotron Radiation Lightsource (SSRL). XPS samples were stored in a nitrogen glove box at all times except briefly during transfer to the ultra-high vacuum chamber for

measurement. Energy calibration was performed relative to residual carbon 1s signal found in all samples, which was set to a binding energy of 285 eV. Background subtraction was performed using macros that were developed at SSRL within the data analysis software IGOR Pro.
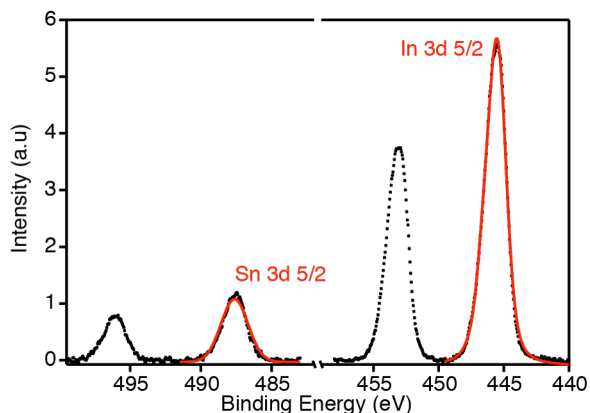
Figure 5.2.2. XPS peaks used for depth profiling (from sample D6 at 650 eV photon energy). Voigt profile fits to the data are shown in red. The area ratio of the Sn $3d_{5/2}$ peak to the total $3d_{5/2}$ signal, extracted from the fit for each peak, was used to quantify surface tin content.

Surface segregation of tin was investigated by comparing the integrated area under the background subtracted In and Sn $3d_{5/2}$ XPS peaks (Figure 5.2.2). To determine the relative tin content, the ratio of the Sn $3d_{5/2}$ peak area to the total area of both peaks was taken, scaled by the relative XPS scattering cross-section for each element at the given photon energy.[112] For the activation series, tin signal was also normalized by the measured doping level from ICP-AES for each individual sample, allowing direct comparison of the dopant profile despite a small variance in doping across the series. Since the $3d_{5/2}$ peaks for both elements are close in binding energy, the error introduced by differences in the escape depth of photoemitted electrons is negligible.

Due to the dependence of electron escape depth on the incident photon energy, energy-dependent XPS is an effective tool for probing the depth-dependence of elemental composition near surfaces.[95] For this reason, three photon energies, 650 eV, 920 eV, and 1150 eV, were used for each sample to probe the dopant depth profile. For clarity, only the results for 650 eV and 1150 eV, representing the most surface-sensitive and least surface-sensitive cases, respectively, are shown here. These are compared to the average compositions determined by ICP-AES.

5.3   Results and discussion

The electron concentrations and surface composition of the doping series are consistent with the reported doping behavior of thin-film ITO. As doping is increased, a strong extinction feature due to the LSPR grows in intensity, first blueshifting into the NIR and then redshifting above ~7 cat. % Sn (Figure 5.3.1a). The extracted electron concentration for nanocrystals with LSPRs peaking in the range of the spectrometer show a trend consistent with that observed for bulk and thin-film ITO, with maximum concentration in the range of 5 – 7 cat. % Sn. This trend can be explained by the increasing formation of irreducible Sn complexes with oxygen interstitial atoms at higher Sn concentration.[31]

The doping series shows uniform dopant distribution for low doping levels and surface segregation of tin at higher doping levels (Figure 5.3.1b). Between 0.1 and 5.1 cat. % Sn there is a linear relationship of doping with the near-surface tin content measured by XPS, with both photon energies giving approximately the same value. This indicates a uniform dopant profile, with Sn distributed evenly throughout the nanocrystal. By contrast, at 6.5 and 7.6 cat. % Sn, there is a marked increase in surface tin content, with values nearly twice the values measured by ICP-AES. At these doping levels, the measured tin content is also higher for 650 eV photons than for 1150 eV photons. These results indicate surface segregation of tin at higher doping levels, consistent with the formation of Sn-rich surfaces that has been widely documented in bulk and thin-film ITO;[113–115] similarly, aluminum-rich surfaces have been found in thin films[116] and colloidally prepared nanocrystals[13] of aluminum-doped zinc oxide.
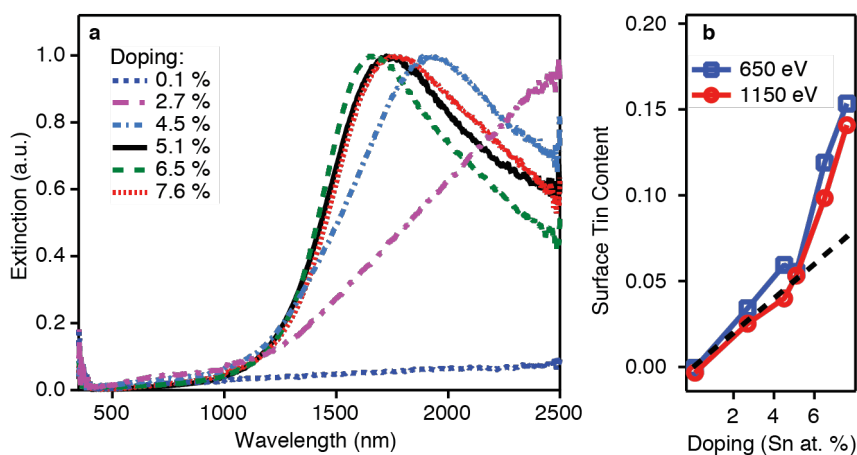

Figure 5.3.1. (a) Optical extinction and (b) XPS depth profiling vs. doping for the doping series. The dotted black line in panel (b) shows expected Sn/(In + Sn) ratio for a uniform doping profile.
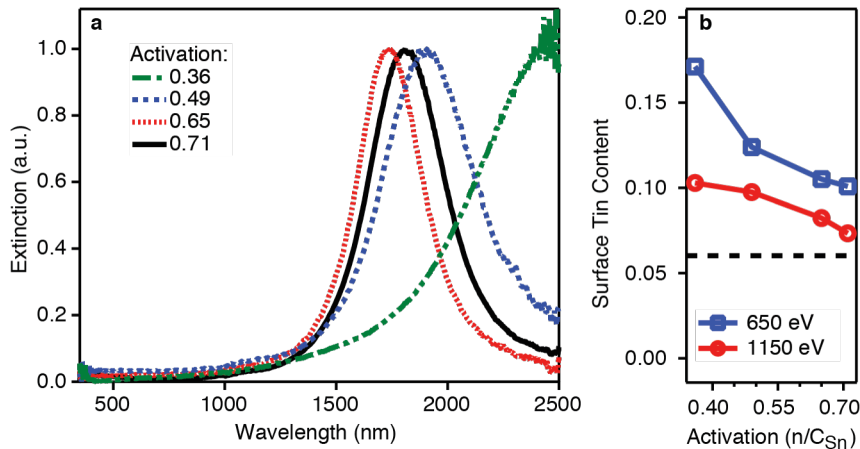
Figure 5.3.2. (a) Optical extinction and (b) XPS depth profiling vs. activation for the activation series. The dashed black line in panel (b) corresponds to the average doping level for nanocrystals in this series.

Very similar elemental doping can also result in a wide range of free electron concentrations in ITO nanocrystals, indicating sample-to-sample differences in dopant activation. This variation can be qualitatively appreciated by the noting the large spread in LSPR frequencies observed for the activation series (Figure 5.3.2a). While these samples have approximately equal doping levels of 6.09 ± 0.64 cat. % Sn, the LSPRs show a spread of >700 nm in wavelength, exceeding any expected difference due to the small variance in doping across the sample set. Moreover, the observed shifts in the LSPR do not follow the sample-to-sample variation in doping levels, suggesting the differences in electron concentration arise instead from a compensation mechanism at work in these nanocrystals.

The dopant distribution profile of the activation series provides insight to this compensation mechanism (Figure 5.3.2b). A decreasing monotonic relationship is seen between dopant activation and surface tin content at both photon energies and more tin signal is measured at 650 eV than 1150 eV. The latter difference is significantly larger than that for the higher doped samples in the doping series (see Figure 5.3.1b), indicating stronger surface segregation in the activation series. Moreover, all samples in the activation series have a higher surface tin content than their overall doping level, demonstrating surface segregation of Sn in even the most highly activated sample. These differences in surface segregation could arise due to the different precursors and surfactants used in each synthesis method. Indium and tin have similar reactivity when coordinated by the same type of ligands, such as the carboxylates employed in the doping series. Balanced rates of indium and tin addition reactions would explain the homogeneous distribution of tin resulting from that synthetic method.

However, in the reactions used to produce the activation series, the reactivity of the tin precursor ($Sn(acac)_2Cl_2$) may be reduced relative to the indium precursor ($In(acac)_3$) by the coordination of hard chloride ligands and the absence of any carboxylic acid that could the displace these ligands. Since doping kinetics depend strongly on precursor reactivity,[11] these synthetic differences are likely responsible for altering the doping profile in each set of nanocrystals.

Several detailed studies have investigated surface defects as possible charge compensating mechanisms in ITO. Early results[113] suggested the formation of alternate tin phases including SnO, SnO_2, and Sn_3O_4 based on analysis of Sn 3d XPS peak components. More recent work[114,115,117] has suggested that a combination of Sn sp hybridized surface states acting as electron traps and near-surface oxygen interstitial diffusion forming non-reducible clusters leads to a "chemical depletion region" (i.e. reduced activation) near the ITO surface. The trapping of electrons at the surface also creates a thin space-charge region that is depleted of free carriers.

We suspect a similar combination of defects to play a role in determining the activation level of our samples. The ease of oxygen interstitial incorporation in the bixbyite lattice of ITO and the low formation energy for $Sn_{In} - O_i''$ complexes makes it likely that these defects play a role in our samples. Drude modeling of optical data on thin nanocrystal films also suggests a large potential barrier to inter-particle electronic conduction,[58] consistent with the existence of an insulating depletion region near the surfaces of our particles and indicating that surface electron traps due to tin orbital hybridization may also play a key role as a compensating mechanism in nanocrystalline ITO. Such hybridization could be due to surface oxygen species like hydroxide ions creating deep trap sites.

The existence of a depletion region due to electronic trap states near the ITO surface is further supported by preliminary observations of the electronic conductivity of films made from nanocrystals in each series. For an electron concentration of ~1.1 x 10^{21} cm^{-1}, films made from the activation series, which show significant surface segregation of tin, demonstrate conductivities that are two to three orders of magnitude greater than films made from the doping series (10^1 S/cm vs. 10^{-2} S/cm). The same variance in conductivity holds true for films prepared as described above, as well as for unannealed films prepared from particles that are ligand-stripped with nitrosonium tetrafluoroborate ($NOBF_4$),[118] indicating that this discrepancy is inherent to the nanocrystals themselves and not due merely to differences in residual surfactants. This observation is consistent with the electrostatics of a semiconductor depletion region, in which the density of ionized dopants determines the width of the depleted layer. Thus, a nanocrystal with significant surface segregation will have a narrower depletion region than a nanocrystals with uniform doping because of the higher density of tin in the near-surface region. Since the electrostatic potential barrier between

66

crystals mediates hopping conduction,[58] a narrower depletion region will correspond to exponentially higher conductivity.

Finally, in addition to influencing their electronic properties, the dopant profile in our ITO nanocrystals also has a strong effect on the optical lineshape of the LSPR, which is determined by damping of the plasmon oscillation. The nanocrystals with uniform dopant distribution exhibit an obvious asymmetry around the LSPR peak, with a steeper change in absorbance on the high-frequency side of the peak than on the low-frequency side (Figure 5.3.1a). On the other hand, the nanocrystals with surface-segregated tin have nearly symmetric Gaussian lineshape (Figure 5.3.2a).

Fitting with the Drude model allows quantitative analysis of plasmon lineshape. The optical properties of a material are determined by its frequency-dependent complex dielectric function. The Drude contribution to the frequency-dependent dielectric function is given by the formula:

$$\varepsilon_D(\omega) = \varepsilon_\infty - \frac{\omega_P{}^2}{\omega^2 - i\omega\Gamma(\omega)} \tag{5.3.1}$$

where ε_∞ is the high-frequency dielectric constant and $\Gamma(\omega)$ is a frequency-dependent damping function. This frequency-dependence arises due to scattering of electrons off ionized impurities, which is known to be the dominant scattering mechanism in the bulk of a degenerately doped semiconductor like ITO.[28,30,63,119] The frequency dependent damping can be modeled using an empirical formula[120] given by:

$$\Gamma(\omega) = \Gamma_L - \frac{\Gamma_L - \Gamma_H}{\pi}\left[\tan^{-1}\left(\frac{\Gamma_X}{\Gamma_W}\right) + \frac{\pi}{2}\right] \tag{5.3.2}$$

where Γ_L is a low-frequency damping constant, Γ_H is a high-frequency damping constant, Γ_X is the crossover frequency between the high and low regimes, and Γ_W is the width of the crossover region. Scattering off ionized impurities is characterized by the low-frequency damping constant, which is also related to the optically derived d.c. mobility of electrons within the crystals. The physics of ionized impurity scattering in metal oxide nanocrystals is reviewed in more detail in reference [39].

Asymmetry in the plasmon lineshape can therefore be attributed to frequency-dependent damping of the plasmon and can be confirmed by the damping parameters extracted by fitting our experimental spectra with the modified Drude model (Figure 5.3.3a and Table 5.3.1). All samples in the series with uniform dopant distribution have a crossover frequency near or just to the red of the

LSPR and a significantly larger Γ_L than Γ_H, consistent with the expectation for frequency dependent damping by ionized impurities.
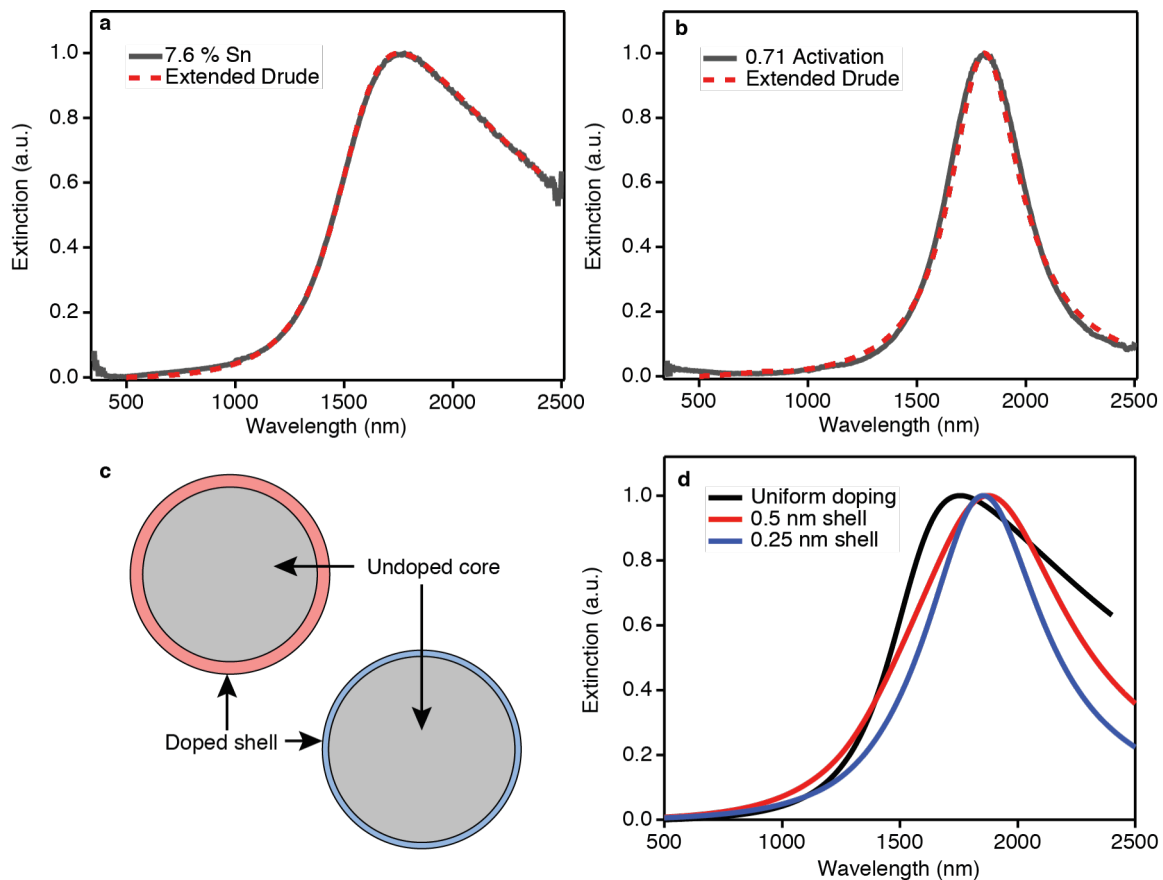
Figure 5.3.3. Optical extinction and Extended Drude fit for (a) sample D6 and (b) sample A4. (c) A core-shell model with a doped shell and undoped core was employed to simulate the optical extinction of surface segregated samples (d), reproducing an asymmetric peak profile similar to that observed.

Table 5.3.1. Relevant Drude parameters for the doping series.

Sample	ω_P (cm^{-1})		Γ_L (cm^{-1})		Γ_H (cm^{-1})		Γ_X (cm^{-1})		Γ_X (nm)	Q	Q_{Drude}
D3	13568	±	8069	±	703.96	±	4710.8	±	2123	-	0.642
	619		2571		426		938				
D4	14868	±	6973	±	0.001	±	5630	±	1776	1.77*	0.831
	229		698		0.001		167.37				
D5	15841	±	5585	±	138.9	±	6055.8	±	1651	2.09	1.08
	0.01		0.06		0.023		0.01				
D6	14932	±	5321	±	257.3	±	5971.2	±	1674	1.86	1.06
	0.01		0.03		0.014		0.01				

Table 5.3.2. Relevant Drude parameters for the activation series.

Sample	ω_P (cm^{-1})	Γ_L (cm^{-1})	Γ_H (cm^{-1})	Γ_X (cm^{-1})	Γ_X (nm)	Q	Q_{Drude}
A1	11668 ± 262	1530 ± 241.5	1589.8 ± 276	9271.6 ± 3319	1078	2.43*	2.54
A2	15202 ± 28.6	1301 ± 75.2	4020.1 ± 1406	10925 ± 2792	915	4.02	4.03
A3	16684 ± 51.4	913.3 ± 219.2	5284.1 ± 3403.5	15209 ± 3741	657	4.85	6.30
A4	16017 ± 43.7	1029.9 ± 178.1	4432.2 ± 2714.5	16348 ± 3800	611	4.41	5.64

By contrast, the symmetry of LSPRs of the nanocrystals with surface-segregated tin suggests ionized impurity scattering is somehow suppressed in these nanocrystals (Figure 5.3.3b and Table 5.3.2). The fits to these spectra result in crossover frequencies far to the blue of their LSPR peaks and a lower Γ_L (higher mobility) than found for the uniformly doped nanocrystals, indicating that the resonance is effectively damped by a frequency-independent constant. To confirm this assertion, the same data was also fit with a simple Drude model (*i.e.* with a fixed damping parameter), which also gave high-quality fits and was able to reproduce spectral lineshapes only for the surface-segregated samples (See A2).

The difference in the optical properties of nanocrystals with uniformly distributed tin dopants and those with surface-segregated tin can also be quantified in terms of the quality factor of the plasmon resonance, $Q = E/\Delta E$, where E is the LSPR energy and ΔE is its optical linewidth. We observe nanocrystals with surface segregated tin to have Q factors more than a factor of two greater than those with uniformly distributed dopants (see Tables 3 and 4). An alternative derivation of Q can be extracted from the Drude fitting, using Γ_L (in units of energy) instead of ΔE. Q_{Drude} is approximately a factor of two smaller than Q for samples with uniformly distributed dopants due to ionized impurity scattering. For samples with surface segregated tin, Q_{Drude} and Q are nearly equivalent. The Q factors for samples A2 – A4 are higher than those reported for copper chalcogenide[121] and tungsten oxide[122] nanocrystals and similar or slightly smaller in magnitude than those recently reported for indium-doped cadmium oxide nanocrystals[20]. Thus, these ITO nanocrystals with surface-segregated dopants have among the highest Q reported to date for semiconducting nanocrystals, approaching values found in noble metal nanoparticles.

We propose a simple physical model to interpret the differences in lineshape observed in the optical spectra of the two sample series based on tin dopant distribution in ITO nanocrystals. A nanocrystal with uniformly distributed ionized dopant impurities will experience frequency-dependent damping of the electron cloud similar to what is observed in thin film and bulk samples (See Figure

5.3.4a). The transition from a low-frequency regime with strong damping due to ionized impurities to a high-frequency regime with much weaker damping is expected to occur just to the red of the plasma frequency.[28] These two regimes lead to an asymmetry centered around the LSPR, as observed in the samples with uniform doping.

For a nanocrystal with tin dopants disproportionately concentrated at or near the surface, on the other hand, most of the electron cloud will elude interaction with ionized impurities at all frequencies (see Figure 5.3.4b), leading to a near-symmetric lineshape. In comparison to the values for a uniform distribution of particles, the fixed damping constant should have a value reflecting scattering in high-quality indium oxide, much smaller than the low-frequency damping constant in uniformly doped ITO. Oxygen vacancy doped indium oxide films most typically have d.c. mobilities on the order of 70 – 100 cm^2/V-s,[27,31] with values as high as 160 cm^2/V-s reported for high quality crystals. This corresponds to damping parameters less than 1000 cm^{-1}. The values extracted for Γ_L in the surface-segregated samples approach this range, indicating a damping profile for the LSPR that is closer to indium oxide than ITO.

To validate this interpretation of the relationship between dopant distribution and lineshape, we simulated the LSPR spectra for nanocrystals with different doping distribution (Figure 5.3.3c and 5.3.3d, with more description in Appendix 2). A uniform distribution yields the expected asymmetry, while nanocrystals composed of an undoped core with a heavily doped shell are predicted to have highly symmetric LSPR spectra. In essence, the surface-segregated dopants donate electrons to the defect-free core where they experience minimal damping. Furthermore, a thinner shell leads to a narrower lineshape, with a close approximation to our data for a 0.25 nm shell. This suggests that tin is segregated within the first few atomic layers of the crystal for these samples.
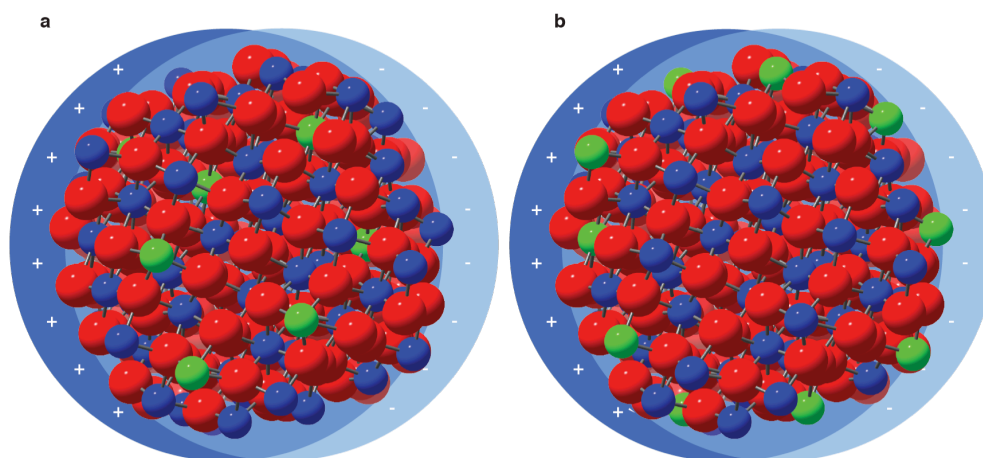
Figure 5.3.4. Schematic representation of plasmonic nanocrystals with (a) uniform and (b) surface segregated dopant distributions. When the LSPR is excited, the electron cloud oscillates in response to an external electric field. In (a), most of the electron cloud is scattered from ionized impurities, pictured in green, while in (b) most of the electron cloud is oscillating away from these impurities.

5.4   Conclusion

We have demonstrated that the dopant distribution has a strong effect on the optoelectronic properties of colloidal ITO nanocrystals. In particular, the activation of dopants and LSPR lineshape are correlated to the degree of tin surface segregation.   While we suggest based on the literature that oxygen interstitial defects and tin orbital hybridization at or near the ITO surface may be responsible for the observed trends in dopant activation, detailed further experimental and theoretical study will be needed to characterize and understand these defects. Nonetheless, our results suggest that deliberate control over dopant distributions could be used to sculpt the electrostatic landscape experienced by free electrons and thereby tune the optoelectronic properties of plasmonic ITO nanocrystals for targeted applications. For sensing applications,[2,123–125] where a high quality factor that allows precise tracking of the LSPR frequency and its sensitivity to the surrounding dielectric medium is needed, a narrower and more symmetric lineshape may be desirable. On the other hand, applications like plasmonic smart windows[24,29,40] that require manufacture of nanocrystals with consistent properties across large batches and deployment of devices for decades without performance degradation, may require nanocrystals that are less sensitive to dopant compensation in the near surface region; these requirements may be best met by uniformly distributing

dopants or even adding an undoped shell. Engineering of dopant distribution presents a new frontier of opportunity for tunable plasmonic materials that is so far accessible only in doped semiconductor nanocrystals.

6 Radial dopant distribution influences conductivity in indium tin oxide nanocrystal films

6.1   Introduction

As the popularity of using colloidal synthesis to solution-process assembled films of nanocrystals has grown in recent years,[18,93] there has been great interest in strategies to modulate the conductivity of nanocrystal solids. Most efforts in this field have focused on interchanging the organic capping ligands that are used to control the growth and solubility of colloidal nanocrystals, with other varieties of organic and inorganic ligands to facilitate charge transfer.[111] By changing the length and dielectric properties of these ligands, it is possible to dramatically change the conductivity of assembled films by altering the electrostatic barrier to hopping conduction between adjacent nanocrystals.[126] However, nanocrystal films with ligands still in place are often too resistive to be optimal for device applications. For this reason, various ligand stripping or decomposition reactions have been developed to improve the overall conductivity of these films. In doing so, the modulation provided by the ligands is nullified. Surprisingly little research has appeared on modulation of conductivity in nanocrystal films that have been processed to remove ligands, and the ways in which the underlying structural and electronic properties of the nanocrystals themselves influence conductivity are poorly understood.

Herein, we report the direct influence of radial dopant distribution on conductivity in dense films of tin-doped indium oxide (ITO) nanocrystals. By varying the synthetic methods used, we are able to reproducibly manufacture ITO nanocrystals with both surface-segregated and uniform dopant distributions that are similar in size, doping, and electron density. In addition to influencing the lineshape of the localized surface plasmon resonance (LSPR) in these nanocrystals,[92] films made from surface-segregated crystals demonstrate nearly a factor of 30 greater conductivity than those made from uniformly doped crystals. Based on detailed measurement of core level and valence band binding energies, we rule out the possibility that this improvement is due to differences in the near-surface depletion region inside the nanocrystals arising from dramatically different dopant distributions.

6.2 Experimental Section

ITO nanocrystals were synthesized using adaptations of methods reported in the literature. Previous work by our group[92] has shown that the methods described in ref [25] lead to particles with a high degree of tin surface segregation while those in ref [19] lead to uniformly doped particles. Particles similar in size, doping, and electron density were used in order to control for these parameters in interpreting relative conductivity of films made from each type (See Table 1).

Table 5.2.1 ITO sample characteristics

Sample	Dopant distribution	Size (nm)	Doping (at. % Sn)	n (cm^{-3})
ITO1	Surface segregated	7.3 ± 1.0	6.3	9.26 x 10^{20}
ITO2	Uniform	6.6 ± 1.1	5.6	9.92 x 10^{20}

Particle size and structure were verified by transmission electron microscopy (TEM, See Figure 5.2.1a) and x-ray diffraction (XRD, See Figure 5.2.1b), while dopant incorporation was measured using inductively coupled plasma atomic emission spectroscopy (ICP-AES). For XPS and conductivity measurements, the nanocrystals were spin-coated from a concentrated solution of 1:1 hexane:octane onto silicon and glass substrates, respectively, yielding several hundred nm thick films. To create a direct interface between nanocrystals for conductivity measurements and in order to facilitate quantitative interpretation of surface-sensitive XPS spectra and limit charging, the bulky organic capping ligands on these films were exchanged with formic acid,[111] followed by a 30 minute anneal in flowing argon gas to decompose the remaining organic matter. The resulting films were highly transparent at visible wavelengths. Film morphology and thickness were verified by scanning electron microscopy (SEM, Figures 5.2.1c and 5.2.1d), indicating densely packed films with direct contact between nanocrystals and minimal cracking. No evidence of particle necking was observed after annealing.
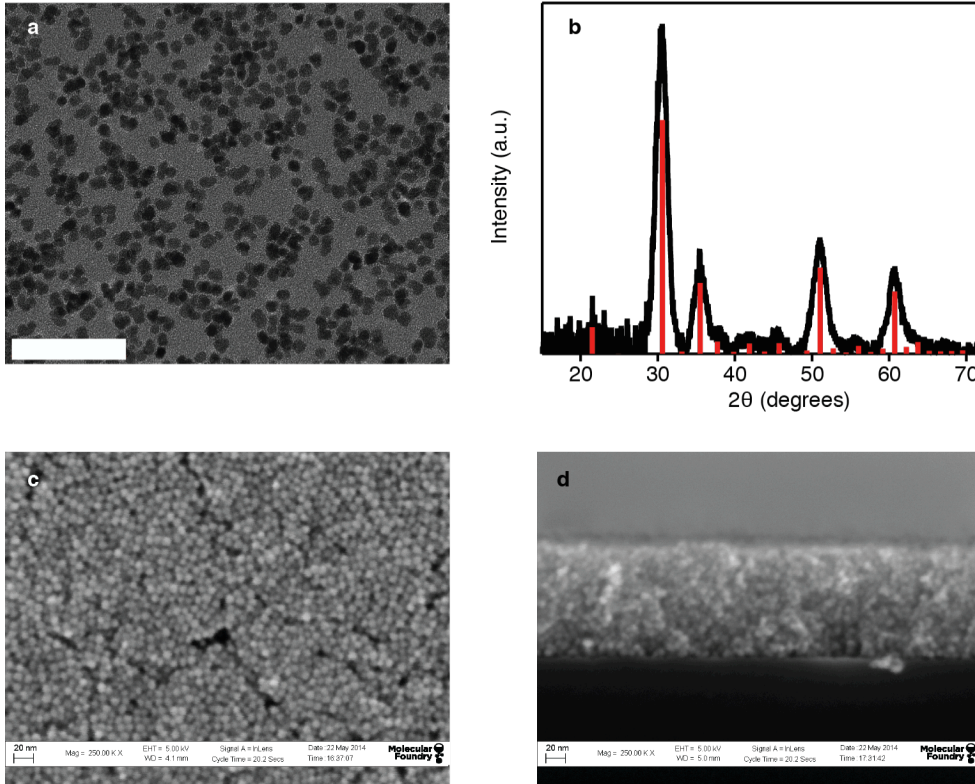
Figure 5.2.1. Characterization of ITO nanocrystals and nanocrystal films. (a) Transmission electron micrograph of ITO1. (b) X-ray diffraction pattern for ITO1, showing the bixbyite lattice characteristic of ITO1 (reference pattern JCPDS 06-0416 is shown in red). (c) Scanning electron micrograph (SEM) of film 1 showing densely packed nanocrystal film (d) Cross sectional SEM of film 1, showing a thickness of ~120nm.

Optical measurements were made on dilute solutions of each sample in tetrachloroethylene using a UV-VIS-NIR spectrometer (ASD Inc./PANalytical). All spectra were measured in transmission mode and are presented as optical extinction. These spectra were fit within a MATLAB code developed by our group[55] using an extended Drude model employing the Maxwell-Garnett effective medium approximation. This model allows extraction of free electron concentrations within each sample based on the Drude formula:

$$\omega_P{}^2 = \frac{ne^2}{m^*\varepsilon_0} \tag{6.2.1}$$

where ω_P is the bulk plasma frequency, n is the free carrier concentration, e is the elementary charge, m^* is the carrier effective mass ($0.4m_e$ for ITO[84]), and ε_0 is the permittivity of free space. Care was taken to perform Drude fitting using several randomly generated initial guesses to ensure convergence on reliable values with known error.[58]

76

XPS data were collected on beamline 10-1 at the Stanford Synchrotron Radiation Lightsource (SSRL) and using a laboratory based XPS instrument with Al K-α radiation. XPS samples were stored in a nitrogen glove box at all times except briefly during transfer to the ultra-high vacuum chamber for measurement. For band bending measurements, electron binding energy was calibrated based on the position of the Au 4f core-level, which was measured on a clean gold foil at regular intervals and set to a binding energy of 84 eV. Band bending at the surface of a material leads to rigid shifts of the valence band and electronic core levels and can be quantified by measuring their binding energy relative to a fixed reference like Au. Background subtraction was performed using macros that were developed at SSRL within the data analysis software IGOR Pro.

Surface segregation of tin was investigated by comparing the integrated area under the background subtracted In and Sn $3d_{5/2}$ XPS peaks (Figure 5.3.1a). To determine the relative tin content, the ratio of the Sn $3d_{5/2}$ peak area to the total area of both peaks was taken, scaled by the relative XPS scattering cross-section for each element at the given photon energy.[112] Since the $3d_{5/2}$ peaks for both elements are close in binding energy, the error introduced by differences in the escape depth of photoemitted electrons is negligible. Due to the dependence of electron escape depth on the incident photon energy, energy-dependent XPS is an effective tool for probing the depth-dependence of elemental composition near surfaces.[95] For this reason, six photon energies – 650 eV, 785 eV, 920 eV, 1035 eV, 1150 eV, and 1486 eV – corresponding to electron escape depths of ~0.7 to 2.0 nm, were used for each sample to probe the dopant depth profile. These were compared to the average compositions determined by ICP-AES.

Resistivity of the ITO nanocrystal films was measured in a 4-point van der Pauw geometry on an Ecopia Hall Effect measurement system. Gold spring-clip contacts were place directly on the films and edge effects were minimized by isolating a uniform region in the center of the sample using a diamond scribe. Source current was chosen carefully to fall within a regime of Ohmic contact.

6.3 Results and discussion

Sample ITO1 showed a high degree of surface segregation of tin ions, while sample ITO2 showed a more uniform distribution (Figure 5.3.1b). When compared to the doping level measured by ICP-OES (dotted lines), sample ITO1 showed elevated tin content in the near surface region, with values nearly double the average doping level. By contrast, sample ITO2 showed nearly the same level of surface tin content as the measured doping level. Anomalously, the trend in surface tin content with photon energy, and hence probe depth, was not monotonic for sample ITO1, showing a maximum value at 920 eV. This suggests the presence of a thin indium-rich surface layer just outside the highly tin doped region near the surface but further investigation is needed to understand this

behavior. However, above 920 eV, the tin content decreased with increasing photon energy, consistent with an interpretation of surface segregation.
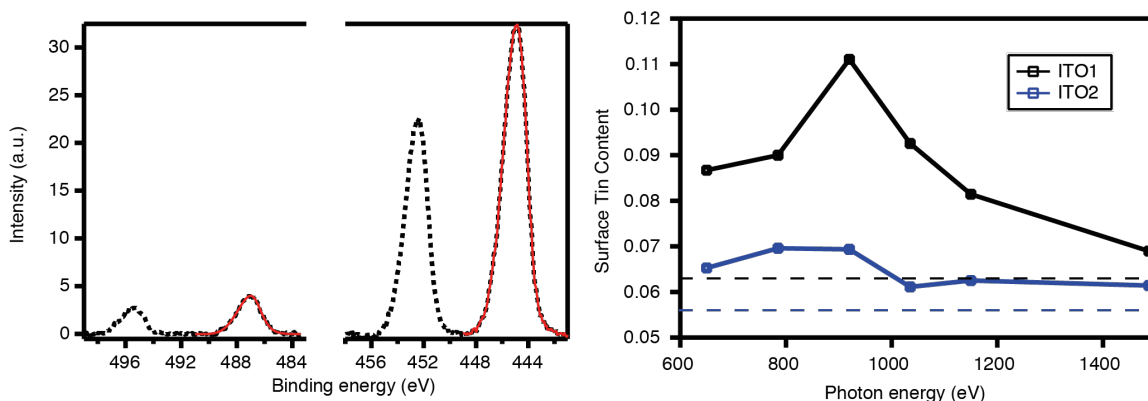

Figure 5.3.1. X-ray photoelectron spectroscopy on ITO nanocrystals. (a) To compute the surface tin content, the area under the Sn 3d$_{5/2}$ peak was compared to the total area under the Sn 3d$_{5/2}$ and the In 3d$_{5/2}$ peaks. Fits to the data are shown in red. (b) ITO1 shows elevated levels of surface tin content relative to its average doping level (black dotted line), while ITO2 shows a similar level to its average doping level (blue dotted line)

Consistent with previous work,[92] the differences in dopant distribution also lead to dramatic differences in the lineshape of the LSPR (Figure 5.3.2). Nanocrystals with surface segregated tin show a highly symmetric plasmon (Figure 5.3.2a), while those with uniform doping show a highly asymmetric plasmon (Figure 5.3.2b). These changes are attributed to the interaction of the oscillating electron cloud with ionized tin dopants, which is known to create asymmetry in the optical properties of ITO.[28,30,39,127] In the case of of surface segregated tin, the majority of the electron cloud evades interaction with these scattering centers, and the peak becomes narrower and more symmetric.
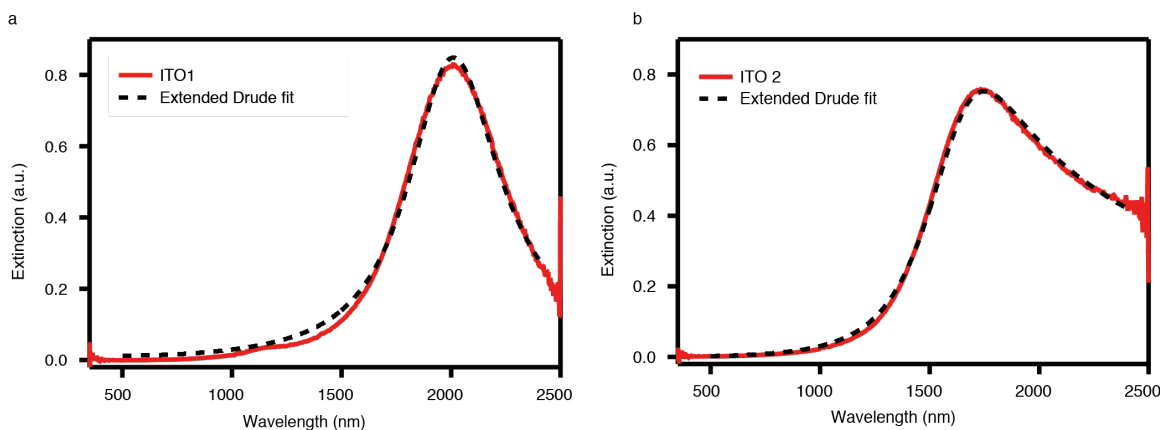

Figure 5.3.2 Optical extinction of ITO nanocrystal samples (a) ITO1 and (b) ITO2 in tetrachloroethylene (TCE) along with corresponding fit using the extended Drude model

78

Films made from ITO nanocrystals with different radial doping distributions also showed dramatically different resistivities (Table 2). Densely packed films made from nanocrystals with surface segregated tin had resistivities on the order of 10^{-1} Ω-cm, while those made from nanocrystals with uniformly distributed tin had resistitivites on the order of 10^{0} Ω-cm. The overall difference in conductivity between the two types of nanocrystal films was one order of magnitude.

Table 5.3.1.

Sample	ρ (Ω-cm)
ITO1 (eITO56)	1.5×10^{-1}
ITO2 (eITO57)	1.5×10^{0}
ρ_{ITO1}/ρ_{ITO2}	10

Previous work has demonstrated that ITO nanocrystal films conduct electrons via hopping conduction, mediated by an insulating region between nanocrystals.[58] Based on this we hypothesized a simple physical model to understand this insulating interface based on a depletion region due to band bending at the surface of the nanocrystals. (Figure 5.3.3) Such a depletion region has also been reported in thin film ITO and attributed to a negative surface charge at anion surface sites and hydroxylated cation sites, which creates a space charge region at the surface.[128] Oxygen 1s XPS demonstrates clear hydroxylation of the surface of our ITO nanocrystals, validating the plausibility of this interpretation. In a nanocrystal film, this width of this space charge region will determine the width of the barrier to electron hopping. Because of the increased density of tin ions near the surface of a surface segregated sample, a much thinner space charge region is needed to compensate a given amount of surface charge (Figure 5.3.3b) than in a uniformly doped sample (Figure 5.3.3c).
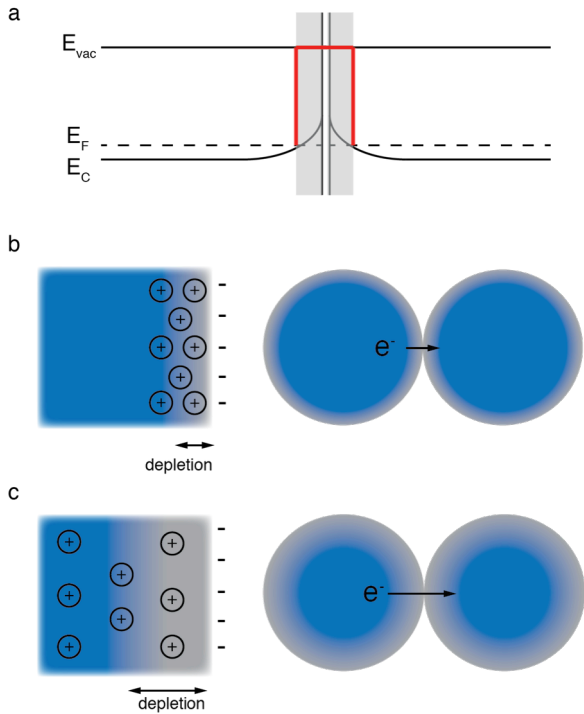
Figure 5.3.3. Hypothetical model for influence of radial dopant distribution on surface electrostatics. (a) Band bending leads to a depletion region (in grey) and defines the width of the potential barrier to electron hopping (red line). (b) For surface segregated dopants the depletion region will extend less far into the nanocrystal than for (c) uniform doping for an equivalent amount of surface charge.

However, measurements of valence band and core level binding energies do not show the expected differences in band bending at the surface (Figure 5.3.4), contradicting the proposed model. In both the valence band spectra (Figure 5.3.4a) and at the In $3d_{5/2}$ core level, there is no appreciable shift in the binding energy from one sample to the next, indicating that the band bending at the surface is similar between the two samples.
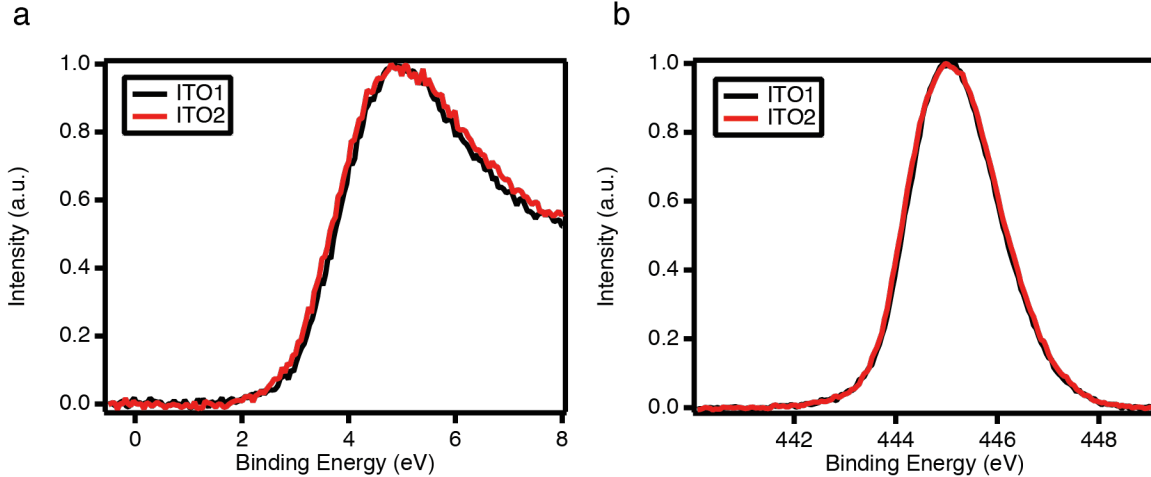
Figure 5.3.4. Binding energy of the (a) valence band and (b) In $3d_{5/2}$ core level for surface segregated (black) and uniformly doped (red) samples. Error in the binding energy calibration based on the Au 4f core level is less than 0.03 eV. Both measurements were made at photon energies corresponding to a probe depth of ~0.7nm.

6.4 Conclusion

We have demonstrated the influence of radial dopant distribution on electronic transport in ligand-free ITO nanocrystal films. Films made from nanocrystals with surface segregated dopants have a higher conductivity than those made with nanocrystals having a uniform dopant distribution by an order of magnitude. We rule out that this difference could be due to a narrowing of the width of a depletion region at the nanocrystal surface because of a higher density of dopant ions in surface segregated nanocrystals. However, further work is needed to characterize the surface chemistry and electronic structure of these nanocrystals in order to verify this model and provide more insight into the mechanism for improved conductivity. As control over doping in semiconductor nanocrystals continues to improve, these results suggest a promising route toward optimizing the conductivity of nanocrystal films processed for device applications by manipulating the distribution of dopants at an atomic scale.

7 Conclusion and Outlook

7.1 Conclusion

This thesis has investigated the influence of the radial distribution of dopants on the optoelectronic properties of indium tin oxide nanocrystals. These plasmonic nanocrystals possess properties that are of fundamental interest for the advancement of the understanding of localized surface plasmon resonance in semiconductors, as well as significant applications potential for technologies like smart-windows, solar cells, and organic LEDs. While their plasmonic properties have been investigated to a significant extent in recent years, few, if any, studies have looked at the influence of their underlying microstructure, including anisotropies in doping profiles, on their extrinsic optical and electronic properties. As demonstrated in Chapter 4, these investigations sit at the intersection of the bulk transport properties of the underlying material and the strong influence of the surface at the nanoscale.

Based on the work conducted for this thesis, it is evident that even relatively simple anisotropies such as surface segregation of dopants can have a dramatic effect on the optical response of these materials. As detailed in Chapter 5, the lineshape of LSPRs in ITO nanocrystals is fundamentally altered when moving from a surface segregated doping profile to uniformly doped nanocrystals. In the former case, the LSPR takes on a symmetric, Gaussian lineshape with a high quality factor rivaling that seen in the highest quality metal nanocrystals. In the latter case, the LSPR is strongly damped by ionized impurities, creating an asymmetric lineshape and reducing the quality factor of the oscillator by half or more. In Chapter 6, these investigations were extended to the electronic properties of nanocrystal films. While the radial dopant distribution was shown to have a significant impact on the conductivity of these films, with those made from nanocrystals with surface-segregated dopants showing an order of magnitude higher conductivity than those made from uniformly-doped nanocrystals, the underlying mechanism for this difference still remains a mystery.

Several important fundamental questions arise based on the results presented herein. First and foremost, what is the mechanism that leads to the dramatic difference in lineshape observed from one doping profile to the next? Based on the simulations presented in Chapter 5, we suggest a simple core-shell model for interpreting these results. However this model would need to be reconciled in terms of charge distribution and localization within the nanocrystals. Are the electrons, in fact, more concentrated in the core of the nanocrystals and how localized are their wavefunctions? How does this explanation reconcile with the observation of higher conductivity in films made from the same nanocrystals, which would suggest higher electrical connectivity between the films? Does the degree of surface segregation correlate to the conductivity of films in a sensible way? Can the same effects be observed in other semiconductor nanocrystals? What is the exact nature of the ionized defects in this material and how does their

role compare to that of other defects? By what defect mechanism is activation being reduced in more highly surface segregated samples? Answering, each of these questions would significantly improve our understanding of LSPRs in these nanocrystals and others.

These fundamental questions can also be extended beyond the extrinsic optical response of the nanocrystals. In particular, what do these results tell us about the physics of plasmon dephasing in ITO and other semiconductor nanocrystals? How do electrons interact collectively with ionized impurities in the different doping regimes and what is the threshold for the transition from one regime to another? In order to answer these questions, it will be necessary to precisely characterize the plasmon linewidth in order to decouple the influence of underlying structural properties from that of broadening due to inhomegneities within the nanocrystal ensemble.

Finally, the ability to manipulate the doping profile of ITO and other semiconductor nanocrystals has significant relevance for applications of these materials. In particular, the ability to synthetically optimize the nanocrystal quality factor based on radial dopant distribution could be a boon for optoeletronic devices that require low optical losses in the LSPR. Furthermore, the ability to reliably control and maximize nanocrystal film conductivity will improve the performance of devices based on these nanocrystals, potentially improving their viability in the marketplace.

7.2 Suggestions for future work

7.2.1 Detailed photoelectron spectroscopy on clean ITO nanocrystal surfaces

While XPS was used extensively in this work to perform depth profiling and characterize elemental composition within these nanocrystals, these investigations are only scratching the surface (no pun intended) of possible applications of this powerful technique. Extending this work to ultraviolet photoelectron spectroscopy (UPS) and resonant photoemission spectroscopy (RPES) could illuminate in greater detail the surface electrostatics of these nanocrystals and shed light on the nature of their electronic properties and how the depend on doping and dopant profile. In particular, in thin film ITO, extensive work has been done with XPS and UPS to characterize the nature of surface trap states and depletion regions at the surface.[115,117] Replication of these studies on ITO nanocrystal films could form an important contribution to the literature on these materials.

However, in order to perform deeper studies of the surface electrostatics in these nanocrystals, in particular studies using highly sensitive UPS measurements that have monolayer sensititivy, it will be necessary to clean the surface of the

nanocrystals to remove any remnants of organic matter or other adsorbates that would influence the results. Even though our films are normally processed to remove organic ligands according to the procedures described in chapters 5 and 6, the presence of residual carbon signal in XPS data suggest that the surface is not entirely clean.

In thin film and bulk materials, cleaning would traditionally be accomplished through either annealing or sputtering of the surface *in situ.* Most modern PES beamlines are equipped to perform both of these operations. However these methods have not yet been applied to the measurements of nanocrystal films and the utilization and optimization of these cleaning techniques could open a new area of investigation.

In particular, depth profiling using energy dependent XPS on clean ITO nanocrystals may present an opportunity to uncover more details about the nature of LSPRs by tracking the radial distribution of electron density for different doping levels and dopant distributions. It has been demonstrated that ITO thin films cleaned *in situ* with argon ion sputtering show a plasmon energy loss shoulder in their XPS signal (Figure 7.2.1).[129] By monitoring the position of this peak, it should in principle be possible to determine the local electron density at different depths within ITO nanocrystals. This knowledge could be illuminating in understanding both the scattering mechanisms and transport phenomena discussed in this work, and could be used to validate the hypothesis for reduced scattering by ionized impurities in surface-segregated ITO nanocrystals.
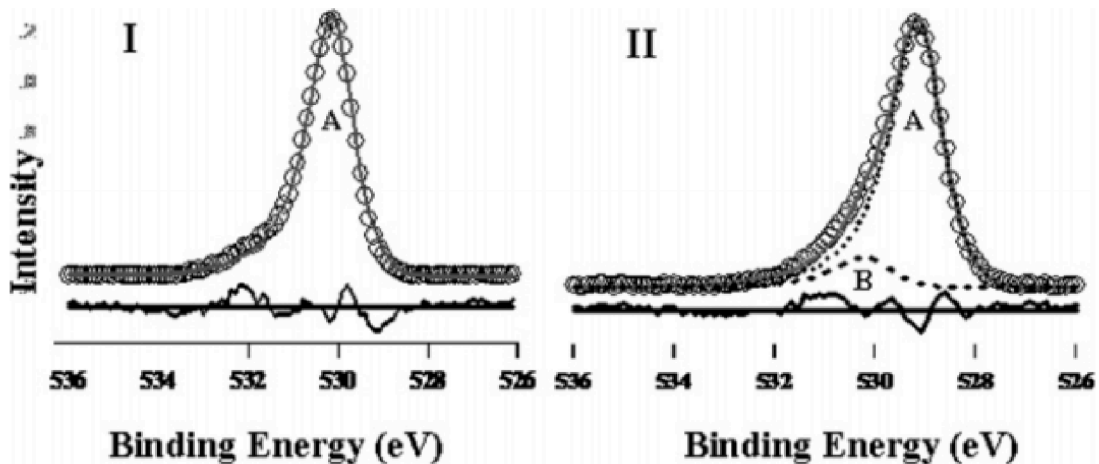

Figure 7.2.1 XPS on sputter deposited and sputter cleaned (I) indium oxide and (II) ITO thin films. In ITO, a second peak is needed to fit the data arising from photoelectron energy loss due to excitation of plasmon oscillation. Adapted from ref [129]

7.2.2 Single nanocrystal spectroscopy

As mentioned in Section 7.1, the differentiation between ensemble and intrinsic broadening effects is crucial to understanding damping and dephasing in LSPRs. The most obvious way to accomplish this is by performing single nanocrystal optical spectroscopy on individual ITO particles. However, while these measurements have been performed on noble metal nanoparticles, the spectrometers used are normally limited to measuring the visible range of the spectrum. Thus, the traditional approach to single nanoparticle LSPR measurements is inapplicable for ITO and other NIR plasmonic nanocrystals.

Recently, it has become possible to perform single nanocrystal FTIR measurements using synchrotron light at the Advanced Light Source at Lawrence Berkeley National Lab. As one of the first users of this technique, we have succeeded in measuring single nanocrystal absorbance measurements on plasmonic aluminum-doped zinc oxide (AZO) nanocrystals (Figure 7.2.2), demonstrating distinct lineshapes within an ensemble of particles – the first measurement of its kind on semiconductor nanocrystals. Further measurements, as well as detailed modeling of the dielectric response of these nanocrystals in the measurement geometry, will be central to understanding dephasing and ensemble effects in AZO, ITO and other nanocrystals.
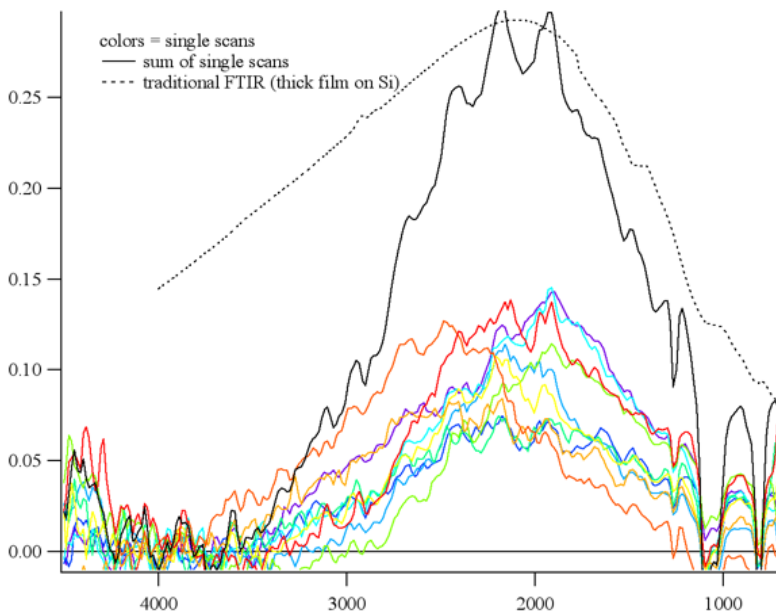

Figure 7.2.2 Single particle measurements of LSPRs in aluminum-doped zinc oxide nanocrystals demonstrate distinct individual lineshapes within an ensemble.

7.2.3 Structural studies

The defect structure of thin film and bulk ITO have been extensively studied but have not been verified in nanocrystalline ITO. Techniques including extended x-ray absorption fine structure (EXAFS), anomalous x-ray diffraction (AXRD), and neutron diffraction have proven to be powerful probes for shedding light on the nature of defects in thin film and bulk samples, particularly in their ability to shed light on the role of oxygen interstitials as compensating mechanisms, as detailed in Section 2.4.2. Extending these studies to ITO nanocrystals could be instructive in understanding the degree to which their defect chemistry mirrors that of the thin film and bulk phases, and in identifying the mechanisms for changes in dopant activation for different radial doping distributions.

7.2.4 Temperature-dependent and controlled-atmosphere resistivity

As discussed in Section 2.5.2, temperature-dependent resistivity measurements are a powerful tool for understanding the nature of conduction in nanocrystal solids. These measurements have only been conducted to a limited extent in ITO nanocrystal films. More detailed and careful measurements of this kind are essential to developing an understanding of transport effects in ITO nanocrystal films and will be important to properly understanding other results like those presented in Chapter 6.

However, in order to properly conduct such measurements, care will have to be taken to control for film morphologies and environmental exposure. For example, in the course of the work for this thesis, it was observed that the resistivity of ligan-exchanged and annealed ITO nanocrystal films increased by several orders of magnitude upon exposure to air, presumably due to the adsorption of atmospheric water molecules (Figure 7.2.2). This effect could be eliminated by storage in a nitrogen gas glove box. Measurements of resistivity in a controlled atmospheric environment would be illuminating in understanding this effect and other ways in which transport in nanocrystal solids can be manipulated by way of surface chemistry.
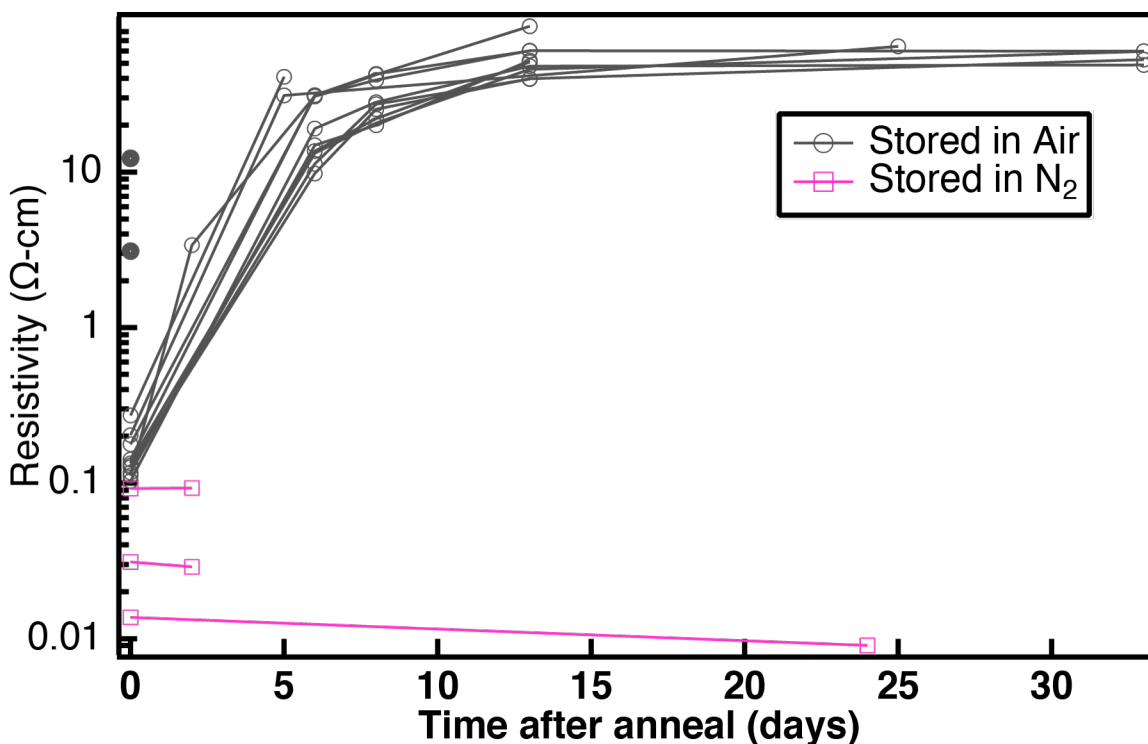
Figure 7.2.2 ITO nanocrystal film resistivity v. time for several films (individual lines). Samples exposed to air (grey) became nearly three orders of magnitude more conductive when exposed to air. When stored in a nitrogen glove box, film conductivity did not change (pink).

7.2.4 pH-dependent conductivity measurements

The properties of thin films of ITO change measurable when their surfaces are treated with various chemicals. In particular, acids and bases are known to alter the work function[130–132] and in-plane conductivity[128] of ITO thin films. Though the exact mechanism for these effects is still a matter of debate in the literature, they are generally considered to be based on ionic modifications of the surface electrostatics of ITO. Given the importance of surfaces and interfaces in determine the transport properties of nanocrystal solids (See Section 2.5), similar modifications of the surface chemistry of ITO nanocrystal films should have significant effects on their conductivity and could provide significant insight into the nature of the surface of ITO nanocrystals. In addition, successful demonstration of the modification of film conductivity by surface chemistry could be useful in replacing energy-intensive annealing processes for device applications.

Measurements of ITO surface modification with acids and bases on nanocrystal films were attempted over the course of many months during the work conducted for this thesis. In particular, treatment with native and mixed solutions of formic

88

acid and tetramethylammonium hydroxide (TMAOH) in water were used to treat films. These films were either treated, dried and measured using the Van der Pauw method or treated and measured *in situ* using impedance spectroscopy. However, though changes in conductivity were observed, they were difficult to reproduce and did not show consistent trends across multiple films. The difficulty of these measurements highlights the complicated role of surface chemistry in influencing transport in nanocrystals solids. Successful, reproducible measurement of these effects will require extreme care to create controlled and stable surface chemistries on the ITO nanocrystals prior to and during measurement, as well as detailed characterization of the surface chemistry under various treatments.

References:

(1)   *Handbook of Transparent Conductors*; Ginley, D. S., Ed.; Springer US: Boston, MA, 2011.

(2)   Willets, K. A.; Van Duyne, R. P. *Annu. Rev. Phys. Chem.* **2007**, *58*, 267–297.

(3)   Hutter, E.; Fendler, J. H. *Adv. Mater.* **2004**, *16*, 1685–1706.

(4)   Ghosh, S.; Pal, T. *Chem. Rev.* **2007**, *107*, 4797–4862.

(5)   Comin, A.; Manna, L. *Chem. Soc. Rev.* **2014**, Advance Article, DOI:10.1039/C3CS60265F.

(6)   Naik, G. V; Shalaev, V. M.; Boltasseva, A. *Adv. Mater.* **2013**, *25*, 3264–3294.

(7)   Schimpf, A. M.; Thakkar, N.; Gunthardt, C. E.; Masiello, D. J.; Gamelin, D. R. *ACS Nano* **2014**, *8*, 1065–1072.

(8)   Mikulec, F. V.; Kuno, M.; Bennati, M.; Hall, D. A.; Griffin, R. G.; Bawendi, M. G. *J. Am. Chem. Soc.* **2000**, *122*, 2532–2540.

(9)   Dalpian, G.; Chelikowsky, J. *Phys. Rev. Lett.* **2006**, *96*, 226802.

(10)   Erwin, S. C.; Zu, L.; Haftel, M. I.; Efros, A. L.; Kennedy, T. A.; Norris, D. J. *Nature* **2005**, *436*, 91–94.

(11)   Buonsanti, R.; Milliron, D. J. *Chem. Mater.* **2013**, *25*, 1305–1317.

(12)   Norris, D. J.; Efros, A. L.; Erwin, S. C. *Science* **2008**, *319*, 1776–1779.

(13)   Buonsanti, R.; Llordes, A.; Aloni, S.; Helms, B. A.; Milliron, D. J. *Nano Lett.* **2011**, *11*, 4706–4710.

(14)   Runnerstrom, E. L.; Llordés, A.; Lounis, S. D.; Milliron, D. J. *Chem. Commun. (Camb).* **2014**.

(15)   Jun, Y.; Choi, J.; Cheon, J. *Angew. Chem. Int. Ed. Engl.* **2006**, *45*, 3414–3439.

(16)   Buonsanti, R.; Grillo, V.; Carlino, E.; Giannini, C.; Kipp, T.; Cingolani, R.; Cozzoli, P. D. *J. Am. Chem. Soc.* **2008**, *130*, 11223–11233.

(17)   Yin, Y.; Alivisatos, A. P. *Nature* **2005**, *437*, 664–670.

(18)   Talapin, D. V.; Lee, J.-S.; Kovalenko, M. V.; Shevchenko, E. V. *Chem. Rev.* **2010**, *110*, 389–458.

(19)   Kanehara, M.; Koike, H.; Yoshinaga, T.; Teranishi, T. *J. Am. Chem. Soc.* **2009**, *131*, 17736–17737.

(20)   Gordon, T. R.; Paik, T.; Klein, D. R.; Naik, G. V; Caglayan, H.; Boltasseva, A.; Murray, C. B. *Nano Lett.* **2013**, *13*, 2857–2863.

(21)   Liu, X.; Swihart, M. T. *Chem. Soc. Rev.* **2014**, *43*, 3908–3920.

(22)   Mocatta, D.; Cohen, G.; Schattner, J.; Millo, O.; Rabani, E.; Banin, U. *Science* **2011**, *332*, 77–81.

(23)   Bryan, J. D.; Gamelin. In *Progress in Inorganic Chemistry*; Karlin, K. D., Ed.; Progress in Inorganic Chemistry; John Wiley & Sons, Inc.: Hoboken, NJ, USA, 2005.

(24)   Garcia, G.; Buonsanti, R.; Llordes, A.; Runnerstrom, E. L.; Bergerud, A.; Milliron, D. J. *Adv. Opt. Mater.* **2013**, *1*, 215–220.

(25)   Choi, S.-I.; Nam, K. M.; Park, B. K.; Seo, W. S.; Park, J. T. *Chem. Mater.* **2008**, *20*, 2609–2611.

(26)   De Trizio, L.; Buonsanti, R.; Schimpf, A. M.; Llordes, A.; Gamelin, D. R.; Simonutti, R.; Milliron, D. J. *Chem. Mater.* **2013**, *25*, 3383–3390.

(27)   Bel Hadj Tahar, R.; Ban, T.; Ohya, Y.; Takahashi, Y. *J. Appl. Phys.* **1998**, *83*, 2631.

(28)   Hamberg, I.; Granqvist, C. G. *J. Appl. Phys.* **1986**, *60*, 123–159.

(29)   Garcia, G.; Buonsanti, R.; Runnerstrom, E. L.; Mendelsberg, R. J.; Llordés, A.; Anders, A.; Richardson, T. J.; Milliron, D. J. *Nano Lett.* **2011**, *11*, 4415–4420.

(30)   Hamberg, I.; Granqvist, C. *Appl. Phys. Lett.* **1984**, *44*, 80721–80723.

(31)   Frank, G.; Kostlin, H. *Appl. Phys. A Solids Surfaces* **1982**, *27*, 197–206.

(32)   Parent, P.; Dexpert, H.; Tourillon, G. *J. Electrochem. Soc.* **1992**, *139*, 282.

(33) Nadaud, N.; Lequeux, N.; Nanot, M.; Jové, J.; Roisnel, T. *J. Solid State Chem.* **1998**, *135*, 140–148.

(34) Parent, P.; Dexpert, H.; Tourillon, G. *J. Electrochem. Soc.* **1992**, *139*, 276–281.

(35) Warschkow, O.; Ellis, D. E.; González, G. B.; Mason, T. O. *J. Am. Ceram. Soc.* **2003**, *86*, 1700–1706.

(36) González, G. B.; Mason, T. O.; Quintana, J. P.; Warschkow, O.; Ellis, D. E.; Hwang, J.-H.; Hodges, J. P.; Jorgensen, J. D. *J. Appl. Phys.* **2004**, *96*, 3912–3920.

(37) González, G. B. *Materials (Basel).* **2012**, *5*, 818–850.

(38) Dresselhaus, M. S. In *SOLID STATE PHYSICS PART II.*

(39) Lounis, S. D.; Runnerstrom, E. L.; Llordés, A.; Milliron, D. J. *J. Phys. Chem. Lett.* **2014**, *5*, 1564–1574.

(40) Llordés, A.; Garcia, G.; Gazquez, J.; Milliron, D. J. *Nature* **2013**, *500*, 323–326.

(41) Routzahn, A. L.; White, S. L.; Fong, L.-K.; Jain, P. K. *Isr. J. Chem.* **2012**, *52*, 983–991.

(42) Scotognella, F.; Valle, G.; Srimath Kandada, A. R.; Zavelani-Rossi, M.; Longhi, S.; Lanzani, G.; Tassone, F. *Eur. Phys. J. B* **2013**, *86*, 154.

(43) Maier, S. A. *Plasmonics: Fundamentals and Applications: Fundamentals and Applications*; Springer, 2007.

(44) Manthiram, K.; Alivisatos, A. P. *J. Am. Chem. Soc.* **2012**, *134*, 3995–3998.

(45) Mattox, T. M.; Bergerud, A.; Agrawal, A.; Milliron, D. J. *Chem. Mater.* **2014**, *26*, 1779–1784.

(46) Smyth, D. M. *Solid State Ionics* **2000**, *129*, 5–12.

(47) Huang, Q.; Hu, S.; Zhuang, J.; Wang, X. *Chemistry* **2012**, *18*, 15283–15287.

(48) Hwang, J.-H.; Edwards, D. D.; Kammler, D. R.; Mason, T. O. *Solid State Ionics* **2000**, *129*, 135–144.

(49) Sienko, M. J. In *Nonstoichiometric Compounds*; Ward, R., Ed.; Advances in Chemistry; American Chemical Society: Washington, D.C., 1963; Vol. 39, pp. 224–236.

(50) Goodenough, J. B. *Prog. Solid State Chem.* **1971**, *5*, 145–399.

(51) Green, M.; Travlos, A. *Philos. Mag. Part B* **1985**, *51*, 501–520.

(52) Takeda, H.; Adachi, K. *J. Am. Ceram. Soc.* **2007**, *90*, 4059–4061.

(53) Schimpf, A. M.; Ochsenbein, S. T.; Buonsanti, R.; Milliron, D. J.; Gamelin, D. R. *Chem. Commun.* **2012**, *48*, 9352–9354.

(54) Dalpian, G.; Chelikowsky, J. *Phys. Rev. Lett.* **2006**, *96*, 226802.

(55) Mendelsberg, R.; Garcia, G.; Li, H.; Manna, L.; Milliron, D. J. *J. Phys. Chem. C* **2012**, *116*, 12226–12231.

(56) Moores, A.; Goettmann, F. *New J. Chem.* **2006**, *30*, 1121–1132.

(57) Scotognella, F.; Della Valle, G.; Ram, A.; Kandada, S.; Dorfs, D.; Zavelani-Rossi, M.; Conforti, M.; Miszta, K.; Comin, A.; Korobchevskaya, K.; Lanzani, G.; Manna, L.; Tassone, F. *Nano Lett.* **2011**, *11*, 4711–4717.

(58) Mendelsberg, R.; Garcia, G.; Milliron, D. J. *J. Appl. Phys.* **2012**, *111*, 063515.

(59) Mendelsberg, R. J.; Anders, A.; Zhu, Y. *J. Phys. D. Appl. Phys.* **2012**, *45*, 425302.

(60) Liu, M.; Pelton, M.; Guyot-Sionnest, P. *Phys. Rev. B* **2009**, *79*, 035418.

(61) Sönnichsen, C.; Franzl, T.; Wilk, T.; von Plessen, G.; Feldmann, J. *Phys. Rev. Lett.* **2002**, *88*, 077402.

(62) Henkel, A.; Jakab, A.; Brunklaus, G.; Sönnichsen, C. *J. Phys. Chem. C* **2009**, *113*, 2200–2204.

(63) Gerlach, E. *J. Phys. C Solid State Phys.* **1986**, *19*, 4585–4603.

(64) Gerlach, E.; Grosse, P. *Festkörperprobleme 17* **1977**, 157–193.

(65) Mergel, D.; Qiao, Z. *J. Phys. D. Appl. Phys.* **2002**, *35*, 794–801.

(66) Gerlach, E. *J. Phys. C Solid State Phys.* **1986**, *4585*.

(67) Ederth, J.; Heszler, P.; Hultåker, A.; Niklasson, G. A.; Granqvist, C. G. *Thin Solid Films* **2003**, *445*, 199–206.

(68) Kiriakidis, G.; Ruske, F.; Pflug, A.; Sittinger, V.; Szyszka, B.; Greiner, D.; Rech, B. *Thin Solid Films* **2009**, *518*, 1289–1293.

(69) Jin, Z.-C.; Hamberg, I.; Granqvist, C. G. *J. Appl. Phys.* **1988**, *64*, 5117.

(70) Mulvaney, P. *Langmuir* **1996**, *12*, 788–800.

(71) Mie, G. *Ann. Phys.* **1908**, *330*, 377–445.

(72) Genzel, L.; Martin, T. P.; Kreibig, U. *Zeitschrift fur Phys. B Condens. Matter Quanta* **1975**, *21*, 339–346.

(73) Kraus, W. A.; Schatz, G. C. *J. Chem. Phys.* **1983**, *79*, 6130.

(74) Scholl, J. A.; Koh, A. L.; Dionne, J. A. *Nature* **2012**, *483*, 421–427.

(75) Purcell, E. M.; Pennypacker, C. R. *Astrophys. J.* **1973**, *186*, 705.

(76) Draine, B. T.; Flatau, P. J. *J. Opt. Soc. Am. A* **1994**, *11*, 1491–1499.

(77) Draine, B. T.; Goodman, J. *Astrophys. J.* **1993**, *405*, 685.

(78) Kelly, K. L.; Coronado, E.; Zhao, L. L.; Schatz, G. C. *J. Phys. Chem. B* **2003**, *107*, 668–677.

(79) Noguez, C. *J. Phys. Chem. C* **2007**, *111*, 3806–3819.

(80) Kriegel, I.; Rodríguez-Fernández, J.; Wisnet, A.; Zhang, H.; Waurisch, C.; Eychmüller, A.; Dubavik, A.; Govorov, A. O.; Feldmann, J. *ACS Nano* **2013**, *7*, 4367–4377.

(81) Chou, L.-W.; Near, R. D.; Boyuk, D. S.; Filler, M. A. *J. Phys. Chem. C* **2014**, *118*, 5494–5500.

(82) Gilstrap, R. A.; Capozzi, C. J.; Carson, C. G.; Gerhardt, R. A.; Summers, C. J. *Adv. Mater.* **2008**, *20*, 4163–4166.

(83) Felde, U. Zum; Haase, M.; Weller, H. *J. Phys. Chem. B* **2000**, *104*, 9388–9395.

(84) Edwards, P.; Porch, A.; Jones, M. *Dalt. Trans.* **2004**, 2995–3002.

(85) Mendelsberg, R. J.; Garcia, G.; Li, H.; Manna, L.; Milliron, D. J. *J. Phys. Chem. C* **2012**, *116*, 12226–12231.

(86) Garnett, J. C. M. *Philos. Trans. R. Soc. A Math. Phys. Eng. Sci.* **1906**, *205*, 237–288.

(87) Bruggeman, D. A. G. *Ann. Phys.* **1935**, *416*, 636–664.

(88) Choi, J.; Kang, N.; Yang, H. Y.; Kim, H. J.; Son, S. U. *Chem. Mater.* **2010**, *22*, 3586–3588.

(89) Hsu, S.-W.; On, K.; Tao, A. R. *J. Am. Chem. Soc.* **2011**, *133*, 19072–19075.

(90) Xie, Y.; Carbone, L.; Nobile, C.; Grillo, V.; D'Agostino, S.; Della Sala, F.; Giannini, C.; Altamura, D.; Oelsner, C.; Kryschi, C.; Cozzoli, P. D. *ACS Nano* **2013**, *7*, 7352–7369.

(91) Owen, J.; Teegarden, K.; Shanks, H. *Phys. Rev. B* **1978**, *18*, 3827–3837.

(92) Lounis, S. D.; Runnerstrom, E. L.; Bergerud, A.; Nordlund, D.; Milliron, D. J. *J. Am. Chem. Soc.* **2014**, *136*, 7110–7116.

(93) Zabet-Khosousi, A.; Dhirani, A.-A. *Chem. Rev.* **2008**, *108*, 4072–4124.

(94) Seah, M. P.; Dench, W. A. *Surf. Interface Anal.* **1979**, *1*, 2–11.

(95) Sarma, D.; Santra, P.; Mukherjee, S.; Nag, A. *Chem. Mater.* **2013**, *25*, 1222–1232.

(96) Daghero, D. Resistivity measurements: the conventional and van der Pauw techniques http://areeweb.polito.it/ricerca/latest/Articoli/vdPauw.pdf (accessed Jun 30, 2014).

(97) Bouillard, J.-S. G.; Dickson, W.; O'Connor, D. P.; Wurtz, G. a; Zayats, A. V. *Nano Lett.* **2012**, *12*, 1561–1565.

(98) Zhang, D. H.; Ma, H. L. **1996**, *492*, 487–493.

(99) Yu, P. Y.; Cardona, M. In *Fundamentals of Semiconductors*; Graduate Texts in Physics; Springer Berlin Heidelberg: Berlin, Heidelberg, 2010; pp. 203–241.

(100) Chiu, S.-P.; Chung, H.-F.; Lin, Y.-H.; Kai, J.-J.; Chen, F.-R.; Lin, J.-J. *Nanotechnology* **2009**, *20*, 105203.

(101) Lin, B.-T.; Chen, Y.-F.; Lin, J.-J.; Wu, C.-Y. *Thin Solid Films* **2010**, *518*, 6997–7001.

(102) Li, Z. Q.; Lin, J. J. *J. Appl. Phys.* **2004**, *96*, 5918.

(103) Bosbach, J.; Hendrich, C.; Stietz, F.; Vartanyan, T.; Träger, F. *Phys. Rev. Lett.* **2002**, *89*, 257404.

(104) Ozdemir, S. K.; Turhan-Sayan, G. *J. Light. Technol.* **2003**, *21*, 805–814.

(105) Kamisaka, H.; Kilina, S. V; Yamashita, K.; Prezhdo, O. V. *Nano Lett.* **2006**, *6*, 2295–2300.

(106) Guo, Z.; Habenicht, B. F.; Liang, W.-Z.; Prezhdo, O. V. *Phys. Rev. B* **2010**, *81*, 125415.

(107) Radovanovic, P. V. In *Functional Metal Oxides: New Science and Novel Applications*; Ogale, S. B.; Venkatesan, T. V.; Blamire, M. G., Eds.; Wiley-VCH Verlag GmbH & Co. KGaA: Weinheim, Germany, 2013; Vol. 2013, pp. 163–194.

(108) Radovanovic, P. V. *Nat. Nanotechnol.* **2009**, *4*, 282–283.

(109) Wang, T.; Radovanovic, P. V. *J. Phys. Chem. C* **2011**, *115*, 406–413.

(110) Lee, J.; Lee, S.; Li, G.; Petruska, M. A.; Paine, D. C.; Sun, S. *J. Am. Chem. Soc.* **2012**, *134*, 13410–13414.

(111) Zarghami, M. H.; Liu, Y.; Gibbs, M.; Gebremichael, E.; Webster, C.; Law, M. *ACS Nano* **2010**, *4*, 2475–2485.

(112) Yeh, J. J.; Lindau, I. *At. Data Nucl. Data Tables* **1985**, *32*, 1–155.

(113) Fan, J. C. C.; Goodenough, J. B. *J. Appl. Phys.* **1977**, *4*, 3524–3531.

(114) Cox, P. A.; Flavell, W. R.; Egdell, R. G. *J. Solid State Chem.* **1987**, *68*, 340–350.

(115) Gassenbauer, Y.; Schafranek, R.; Klein, a.; Zafeiratos, S.; Hävecker, M.; Knop-Gericke, a.; Schlögl, R. *Phys. Rev. B* **2006**, *73*, 245312.

(116) Chen, M.; Pei, Z. L.; Sun, C.; Wen, L. S.; Wang, X. *J. Cryst. Growth* **2000**, *220*, 254–262.

(117) Gassenbauer, Y.; Klein, A. *Solid State Ionics* **2004**, *173*, 141–145.

(118) Dong, A.; Ye, X.; Chen, J.; Kang, Y.; Gordon, T.; Kikkawa, J. M.; Murray, C. B. *J. Am. Chem. Soc.* **2011**, *133*, 998–1006.

(119) Rech, B.; Ruske, F.; Pflug, a.; Szyszka, B.; Greiner, D.; Sittinger, V. *Thin Solid Films* **2009**, *518*, 1289–1293.

(120) Mergel, D.; Qiao, Z. *J. Phys. D. Appl. Phys.* **2002**, *35*, 794–801.

(121) Luther, J. M.; Jain, P. K.; Ewers, T.; Alivisatos, A. P. *Nat. Mater.* **2011**, *10*, 361–366.

(122) Manthiram, K.; Alivisatos, A. *J. Am. Chem. …* **2012**, *8*, 8–11.

(123) Elghanian, R.; Storhoff, J. J.; Mucic, R. C.; Letsinger, R. L.; Mirkin, C. A. *Science* **1997**, *277*, 1078–1081.

(124) Larsson, E. M.; Langhammer, C.; Zorić, I.; Kasemo, B. *Science* **2009**, *326*, 1091–1094.

(125) Liu, N.; Tang, M. L.; Hentschel, M.; Giessen, H.; Alivisatos, A. P. *Nat. Mater.* **2011**, *10*, 631–636.

(126) Talapin, D. V; Murray, C. B. *Science* **2005**, *310*, 86–89.

(127) Gerlach, E.; Grosse, P. In *Festkorperprobleme 17*; Treusch, J., Ed.; Advances in Solid State Physics; Springer Berlin Heidelberg: Berlin, Heidelberg, 1977; Vol. 17.

(128) Swint, A. L.; Bohn, P. W. *Langmuir* **2004**, *20*, 4076–4084.

(129) Brumbach, M.; Veneman, P. A.; Marrikar, F. S.; Schulmeyer, T.; Simmonds, A.; Xia, W.; Lee, P.; Armstrong, N. R. *Langmuir* **2007**, *23*, 11089–11099.

(130) Kim, J. S.; Ho, P. K. H.; Thomas, D. S.; Friend, R. H.; Cacialli, F.; Bao, G.-W.; Li, S. F. Y. *Chem. Phys. Lett.* **1999**, *315*, 307–312.

(131) Nüesch, F.; Rothberg, L. J.; Forsythe, E. W.; Le, Q. T.; Gao, Y. *Appl. Phys. Lett.* **1999**, *74*, 880.

(132) Koh, S. E.; McDonald, K. D.; Holt, D. H.; Dulcey, C. S.; Chaney, J. A.; Pehrsson, P. E. *Langmuir* **2006**, *22*, 6249–6255.

Appendix I: MATLAB Script for Drude Simulation and Fitting

A1.1 Fitting Script

function [ ] = Drude(file_input)

%%%%%%%%%%%%%%%%%%%%%%%%%%%%%%%%%%%%%%Drude%%%%%%%%%%%%%%
%%%%%%%%%%%%%%%%%%%%%%%%%%%%%%

%This function takes input data from a single background-subtracted absorbance measurement
of nanoparticles in solution and performs an Extended
%Drude Approximation fit with a frequency dependent dampning constant. This script is
%based on work by R.J. Mendelsberg. See, for example:

% [1] RJ Mendelsberg, et al. "Extracting reliable electronic properties
% from transmission spectra of indium tin oxide thin films and nanocrystal
% films by careful application of the Drude Theory." 1ournal of Applied
% Physics 111, 063515 (2012)
% [2] RJ Mendelsberg, et al. "Understanding the Plasmon Resonance in
% Ensembles of Degenerately Doped Semiconductor Nanocrystals"

%   INPUTS:
%   file_input - this is the name of a file within the directory
%   'Optical Data in CSV\TCE' that contains the data to
%   be fit by the model. Data must be in a text file
%   with wavelength in the first column and absorbance
%   in the second column, separated by a space.

%%
%%%%%%%%%%%%%%%%%%%%%%%%%%%%%%%%

%INITIALIZE

folder_base='Optical Data in CSV/TCE'; %Folder within the current MATLAB directory that
contains files to be analyzed in CSV format

%the time and date when the fit was initiated will be appended to the fit
%file for record keeping

```matlab
c = clock;
c = num2str(c);
c(c==' ')='';
c(13:end)='';

%Set global variables

global ep_B ep_H L %These varibles must be global, they represent the parameters in the
models which are not free
ep_B=4.2; % Dielectric background constant of ITO
ep_H=2.38; %Dielectric constant of the solvent from Wikipedia
L=1; %Optical path length in cm

%Set fitting constraints

c_ITO=500; %short wavelength (nm) cutoff of fitting region (one must not include bandgap
contributions to the absorbance)
c_ITO2=2400;%long wavelength (nm) cutoff of the fitting region
lambdaITO=linspace(c_ITO,c_ITO2,1024)'; %creates linear space in nanometers between short
and long wavelength cutoff
omegaITO=1e7./lambdaITO; %Frequency variable (wave number)

%Physical constants used in calculations below

mstar=0.4*9.109e-31; %effective mass in kg
echarge=1.6022e-19; %electron charge in coulombs
ep0=8.85e-12; %permittivity of free space

Results = zeros(1,20); %Creates a matrix that will hold the average results of the fits
var = zeros(1,6); % Creates a matrix that will hold variances for the 6 fit parameters

counter = 0; %sets the counter variable to zero (see below)

%GET DATA


    disp('Fitting')
    file_name = file_input
    path_name = [folder_base,'/',file_name];

    %A_measITO=dlmread(path_name,' ',1,0); %Reads the file in DLM format
    A_measITO=csvread(path_name,1,0); %Reads the file in CSV format
    W_measITO=A_measITO(:,1); %Creates wavelength array
    A_measITO=A_measITO(:,2); %Creates absorbance array

    %Get index of elements used in the fitting - i.e. those above the low
    %wavelength cutoff

    kkITO=find(W_measITO>c_ITO & W_measITO<c_ITO2);
    omegaITO_W=1e7./W_measITO(kkITO);
```

```matlab
%EXTENDED DRUDE FIT - run a loop through the loaded files

    %For each file, run the model with a number of different initial
    %guesses, set by the counter number

    while counter < 3

    %Set options for the fitChiSquare function (see the .m file)

        %These can be left alone
        op=optimset;
        op.Display='off';
        op.Plot=1;
        op.ErrorsUnknown = 1;
        op.MaxFunEvals=1e10;
        op.FitUncertainty = [0 0 0 0 0 0];

        %These set the upper and lower bounds for the initial guesses for
        %each parameter [vF,wP,GL,GH,GX,GW]
        op.LowerBound = [5e-7 10000 1     1      1     1];%
        op.UpperBound = [1e-2 20000 10000 10000  20000 5000];

    MSE_guess = 1; %creates the mean squared error variable

    %Generate random initial guesses within the specified bounds to
    %automate initial guesses and eliminate bias

        while MSE_guess>3e-2 %Filter for initial guesses that are decent

            guess_gen=rand(1,6);

            for j = 1:6
                initGuess(j) = op.LowerBound(j)+ guess_gen(j)*(op.UpperBound(j)-op.LowerBound(j));
            end

            MSE_guess=mean((A_measITO(kkITO)-EDA_MG(initGuess,omegaITO_W)).^2);
        end

    %Fit the data for the initial guess


[paramsITO_ed,dParamsITO_ed,gofITO_ed,stddevITO_ed]=fitChiSquare(1e7./W_measITO(kkIT
O),A_measITO(kkITO),@EDA_MG,initGuess,[],[],op);

    MSE_ito_ed=mean((A_measITO(kkITO)-EDA_MG(paramsITO_ed,omegaITO_W)).^2);
%Compute the mean squared error

    if MSE_ito_ed < 1e-3 %Input to the results into columns 2-7 of the array when the fit is good
(also arbitrary).
```

```
%creates a delimited text file with the accepted fit (e.g. for plotting)
yyITO_ED=EDA_MG(paramsITO_ed,omegaITO_W);
fit_output = [c '_fit_' file_input '_' num2str(counter)];
file_output = [c '_params_' file_input '_' num2str(counter)];
dlmwrite(fit_output,yyITO_ED);
dlmwrite(file_output,paramsITO_ed);

counter = counter+1 %advance the counter
disp('Mean squared error');
MSE_ito_ed

if counter == 1  %compute the mean based on current and previous data in the array using
recursive averaging
Results(1,2:7) = paramsITO_ed;
else
Results(1,2:7) = Results(1,2:7) + (1/counter)*(paramsITO_ed - Results(1,2:7));
end

if counter>1 %calculate the recursive variance and input the standard deviation into
column 8 of the results array
var(1:6) = ((counter-1)/counter)*(var(1:6)) + (1/(counter-1))*((paramsITO_ed-
Results(1,2:7)).^2);
Results(1,8:13)= sqrt(var);
end

file_output = ['params_' file_input '_' counter];

    end
  end

  disp('crossover frequency:')
  Results(1,6)

  %Compute the electronic parameters of interest based on fit results

  Results(1,14) = Results(1,4)-((Results(1,4)-Results(1,5))/pi)*(atan(-Results(1,6)/Results(1,7)) +
pi/2); %Compute gamma(0)
  Results(1,15) = (echarge/(mstar*3e10*Results(1,14)*2*pi))*1e4; %compute mobility (mu) in
cm^2/V-s
  Results(1,16) = ((mstar*ep0*(3e10*Results(1,3)*2*pi)^2)/(echarge^2))/1000000; %Compute
carrier concentration (n) in cm^-3
  Results(1,17) = 1/(Results(1,15)*Results(1,16)*echarge); %Compute resistivity

  %error propagation for each of the electronic parameters based on
  %variance in the fit

  w(1) = atan(-Results(1,6)/Results(1,7)) + pi/2;
  z(1) = (Results(1,4)-Results(1,5))/pi;
  q(1) = w(1)*z(1);
  sigf(1) =
```

```matlab
(Results(1,6)./Results(1,7))*sqrt((Results(1,12)./Results(1,6)).^2+(Results(1,13)./Results(1,7)).^2)
;
    sigw(1) = sigf(1)/(1+(Results(1,6)/Results(1,7)).^2);
    sigz(1) = Results(1,10)/pi;
    sigq(1) = q(1)*sqrt((sigz(1)/z(1)).^2+(sigw(1)/w(1)).^2);
    siggam0(1) = sqrt(Results(1,10).^2 + sigq(1).^2);

    %final standard deviation of the electronic parameters

    Results(1,18) = Results(1,15).*siggam0(1)./Results(1,14); %compute standard devation of
mobility
    Results(1,19) = 2*Results(1,16).*Results(1,9)./Results(1,3); %compute standard devation of
carrier concentration
    Results(1,20) =
Results(1,17).*sqrt((Results(1,18)./Results(1,15)).^2+(Results(1,19)./Results(1,16)).^2);
%compute standard devation of resistivity

%create truncated array that contains the last six columns of the results

Results_exp = zeros(1,6);
Results_exp = Results(1,15:20);

%evaluates the absorbance based on the average parameter values
avg_paramsITO_ed = Results(1,2:7);
yyITO_ED=EDA_MG(avg_paramsITO_ed,omegaITO_W);

lambdaITO=1e7./omegaITO_W;

figure(87)
set(gcf,'units','points','position',[300 100 500 500/1.618])
clf
h=[0 0 0 0 0 0 0 0];
hold on
h(1)=plot(W_measITO,A_measITO,'k','linewidth',3);
h(2)=plot(lambdaITO,yyITO_ED,'b-','linewidth',2);

%writes the average fit and results to delimited text files
fit_output = [c '_fit_' file_input '_avg'];
file_output = [c '_results_' file_input '_avg'];
dlmwrite(fit_output,yyITO_ED)
dlmwrite(file_output,Results) %Write the results to a comma delimited file that can be processed
by IGOR

end

%The columns of the Results vector correspond to the following:
%
% (1) - empty
% (2) - volume fraction (vol NCs/total vol)
% (3) - plasma frequency (cm-1)
% (4) - low freq. damping constant (cm-1)
```

% (5) - high freq. damping constant (cm-1)
% (6) - crossover freq. (cm-1)
% (7) - crossover width (cm-1)
% (8) - stdev of (2)
% (9) - stdev of (3)
% (10) - stdev of (4)
% (11) - stdev of (5)
% (12) - stdev of (6)
% (13) - stdev of (7)
% (14) - gamma(0) (cm-1) - see rueben's JAP paper
% (15) - mobility (cm2/V-s)
% (16) - carrier concentration (cm-3)
% (17) - resistivity (ohm-cm)
% (18) - stdev of (15)
% (19) - stdev of (16)
% (20) - stdev of (17)

A1.2 Extended Drude Approximation Dielectric function script

```
function A=EDA_MG(a,xm)
%This function is used to calculate the Absorbance using only the extended
%drude theory
%
%Drude theory with the MG-EMA
%
% Input variables
%   xm -- frequency variable in cm^-1
%   a -- parameters:
%       a(1) -- volume fraction
%       a(2) -- plasma frequency cm^-1
%       a(3) -- low frequency damping constant cm^-1
%       a(4) -- high frequency damping constant cm^-1
%       a(5) -- crossover frequency cm^-1
%       a(6) -- width cm^{-1}
%
%
% Output variables
%   A -- absorbance of the layer

global ep_B ep_H L

%Calculate damping function
GAMMA=a(3)-(a(3)-a(4))/pi*(atan((xm-a(5))/a(6))+pi/2);

%Particle dielectric function
ep_P=ep_B-a(2)^2./(xm.^2+1i*xm.*GAMMA);

% Effective dielectric function
C=a(1)*(ep_P-ep_H)./(ep_P+2*ep_H);
ep_eff=ep_H.*(1+2*C)./(1-C);
%Calculate Absorbance
A=(4*pi*xm.*imag(sqrt(ep_eff)))*L/log(10);
```

Appendix 2: Supporting information for Chapters 5

A2.1 Synthetic Methods

Materials: All chemicals were used as received. Indium acetylacetonate (In(acac)$_3$, 99.99%), indium acetate (In(ac)$_3$, 99.99%) tin bis(acetylacetonate) dichloride (Sn(acac)$_2$Cl$_2$ 98 %), tin acetate (Sn(Ac)$_4$ 99.99%), tin ethylhexanoate (Sn(Oct)$_2$ 95%) myristic acid (MA, ≥ 98%), 1- octadecene (ODE, 90%), oleic acid (OLAC, 90%), octanoic acid (OctAC, 99%), and octyl ether (99%) were purchased from Aldrich and used without further purification. Oleylamine (OLAM, 90%) was obtained from Acros.

Methods: ITO nanocrystals were synthesized using slight modifications of literature procedures. All synthetic protocols were carried out using magnetic stirring under inert atmosphere using standard Schlenk line techniques.

Doping series:

Sample D1, 6.2 nm ITO with 0% Sn: In(ac)$_3$ (1.2 mmol), OctAC (3.6 mmol), and OLAM (10 mmol) were mixed with 10 mL of octyl ether in a 50 mL 3-neck flask and degassed at 80°C for 30 minutes. The temperature of the mixture was then raised to 150°C under nitrogen and held at that temperature for 1 hour. The solution was then heated to 280°C for 2 hours. During the heating step, starting at around 200°C, the solution gradually turned light yellow, then light green, then finally light blue as the solution temperature continued to rise.

Sample D2, 6.1 nm ITO with 2.73% Sn: In(ac)$_3$ (1.164 mmol), Sn(Oct)$_2$ (0.046 mmol), OctAC (3.6 mmol), and OLAM (10 mmol) were mixed with 10 mL of octyl ether and degassed at 80°C for 30 minutes. The temperature of the mixture was then raised to 150°C under nitrogen and held at that temperature for 1 hour. The solution was then heated to 280°C for 2 hours. During the heating step, starting at around 200°C-220°C, the solution gradually turned yellow, then orange/amber, then finally a very dark green/blue as the solution temperature continued to rise.

Sample D3, 6.8 nm ITO with 4.53% Sn: The same procedure was followed as for Sample D2, using 1.14 mmol In(ac)$_3$ and 0.06 mmol Sn(Oct)$_2$.

Sample D4, 6 nm ITO with 5.10% Sn: The same procedure was followed as for Sample D2, using 1.12 mmol In(ac)$_3$ and 0.08 mmol Sn(Oct)$_2$.

Sample D5, 5.5 nm ITO with 6.45% Sn: The same procedure was followed as for Sample D2, using 1.08 mmol In(ac)$_3$ and 0.12 mmol Sn(Oct)$_2$.

Sample D6, 4.9 nm ITO with 7.60% Sn: The same procedure was followed as for Sample D2, using 1.02 mmol In(ac)$_3$ and 0.18 mmol Sn(Oct)$_2$.

Activation series:

Sample A1: 9.6 nm ITO with 5.63% Sn: In(acac)$_3$ (0.508 mmol), Sn(acac)$_2$Cl$_2$ (0.039 mmol), and 2.3 g OLAM were mixed in a 25 mL 3-neck flask. The solution was heated to 110°C for 10 minutes under nitrogen, then heated to 250°C for 5 hours.

Sample A2: 8.7 nm ITO with 6.97% Sn: The same procedure was followed as for Sample A1, using 0.044 mmol Sn(acac)$_2$Cl$_2$, a 50 mL 3-neck flask, and increasing the OLAM to 7.01 g.

Sample A3: 10.8 nm ITO with 6.40% Sn: The same procedure was followed as for Sample A2, using 0.041 mmol Sn(acac)$_2$Cl$_2$.

Sample A4: 8.5 nm ITO with 5.34% Sn: The same procedure was followed as for Sample A1, using a 50 mL 3-neck flask and increasing the OLAM to 7.01 g.

A2.2 Sample Characterization

X-ray diffraction (XRD) and transmission electron microscopy (TEM) were used to characterize the crystalline phase, size, and shape of our nanocrystals. XRD was collected on a Bruker D8 Discover X-ray diffractometer equipped with a GADDS area detector and operated at 40 kV and 20 mA at the Cu Kα wavelength, 1.54 Å (Figures A2.1 and A2.2). TEM characterization was performed on a Zeiss Libra 120 TEM operated at 120 kV accelerating voltage. TEM samples were prepared by diluting 10 µL of the purified ITO nanocrystal suspension in 1 mL of hexane, and dropping 10 µL of the diluted suspension onto a copper TEM grid (Figures A2.3 and A2.4).
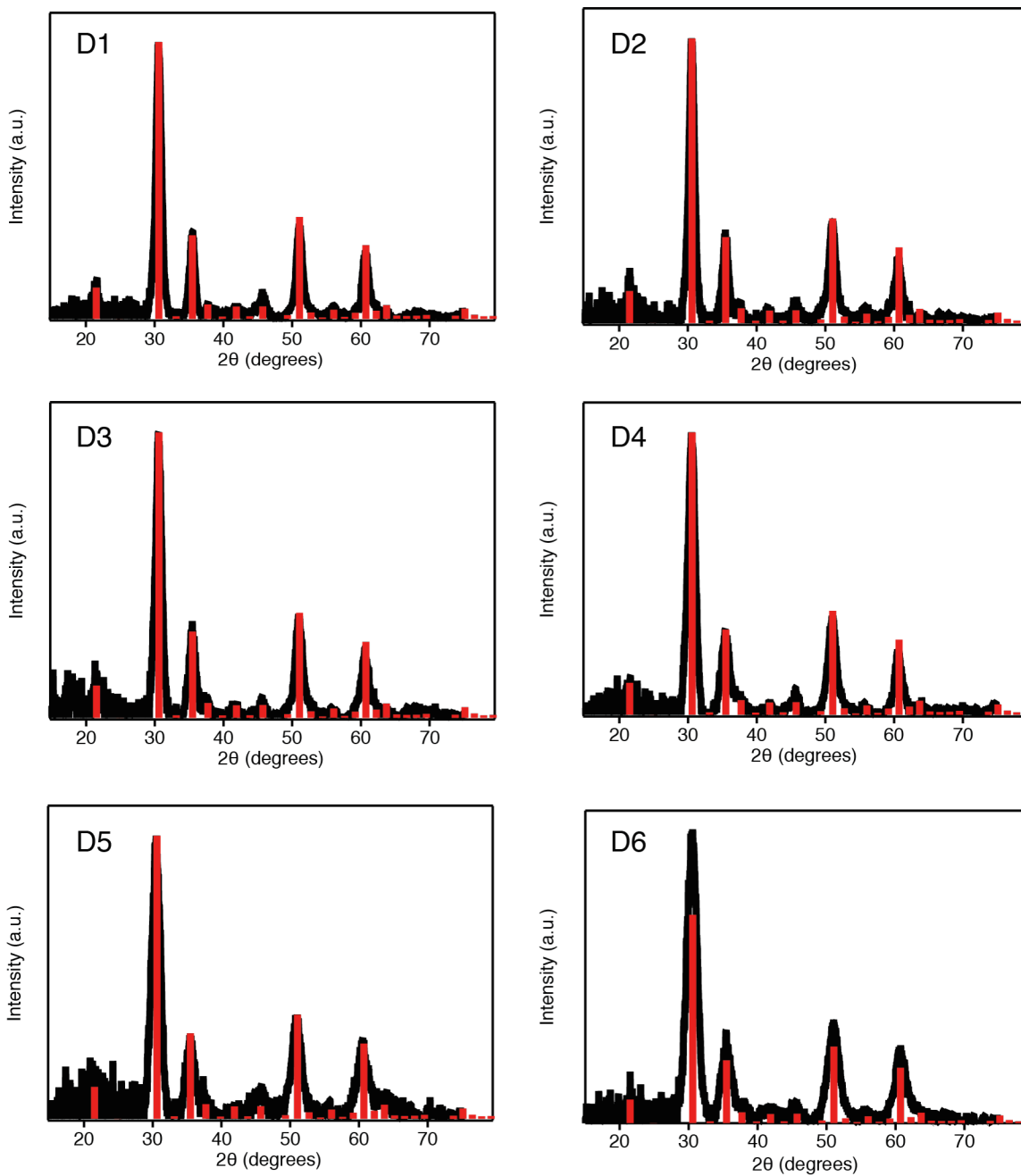
Figure A2.1. X-ray diffraction patterns for each sample in the doping series, confirming cubic bixbyite structure (reference pattern JCPDS 06-0416 is shown in red).
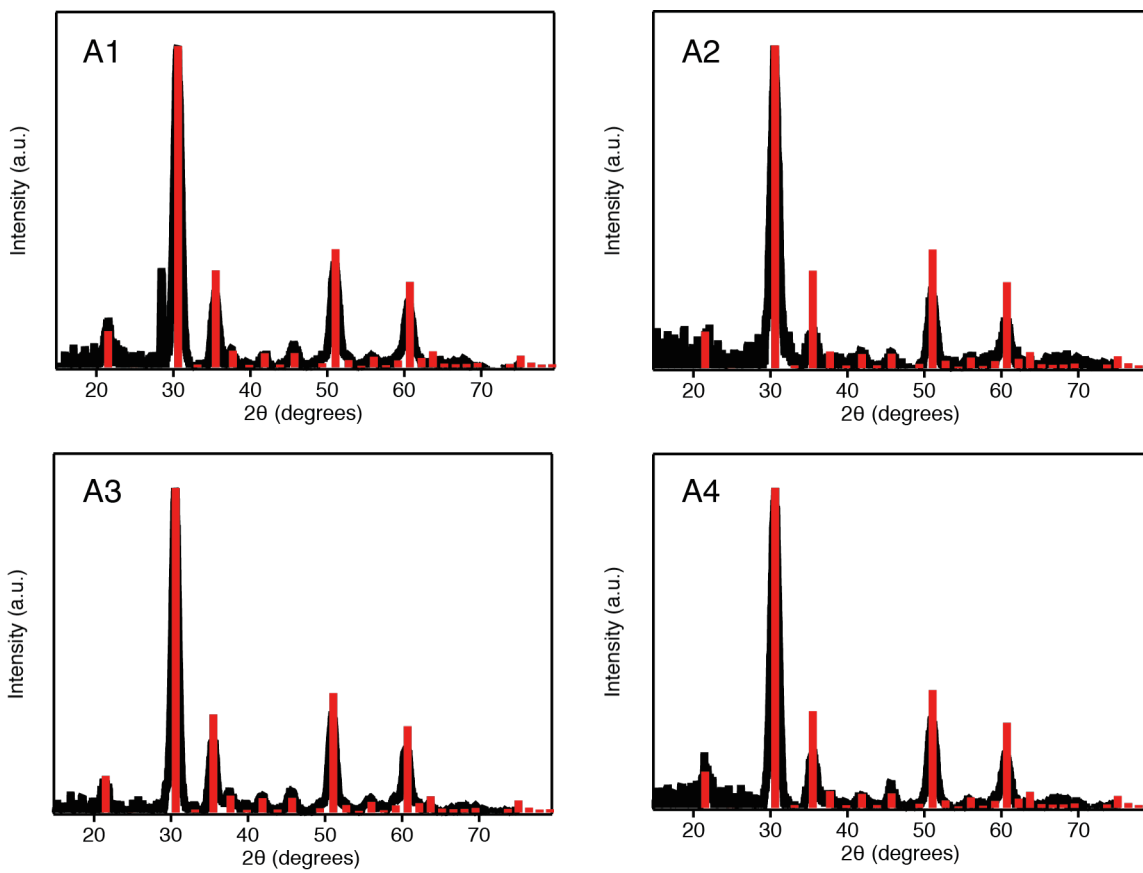
Figure A2.2. X-ray diffraction patterns for each sample in the activation series, confirming cubic bixbyite structure (reference pattern JCPDS 06-0416 is shown in red). The unmarked peak in the diffraction pattern for sample A1 is an artifact due to the silicon substrate.
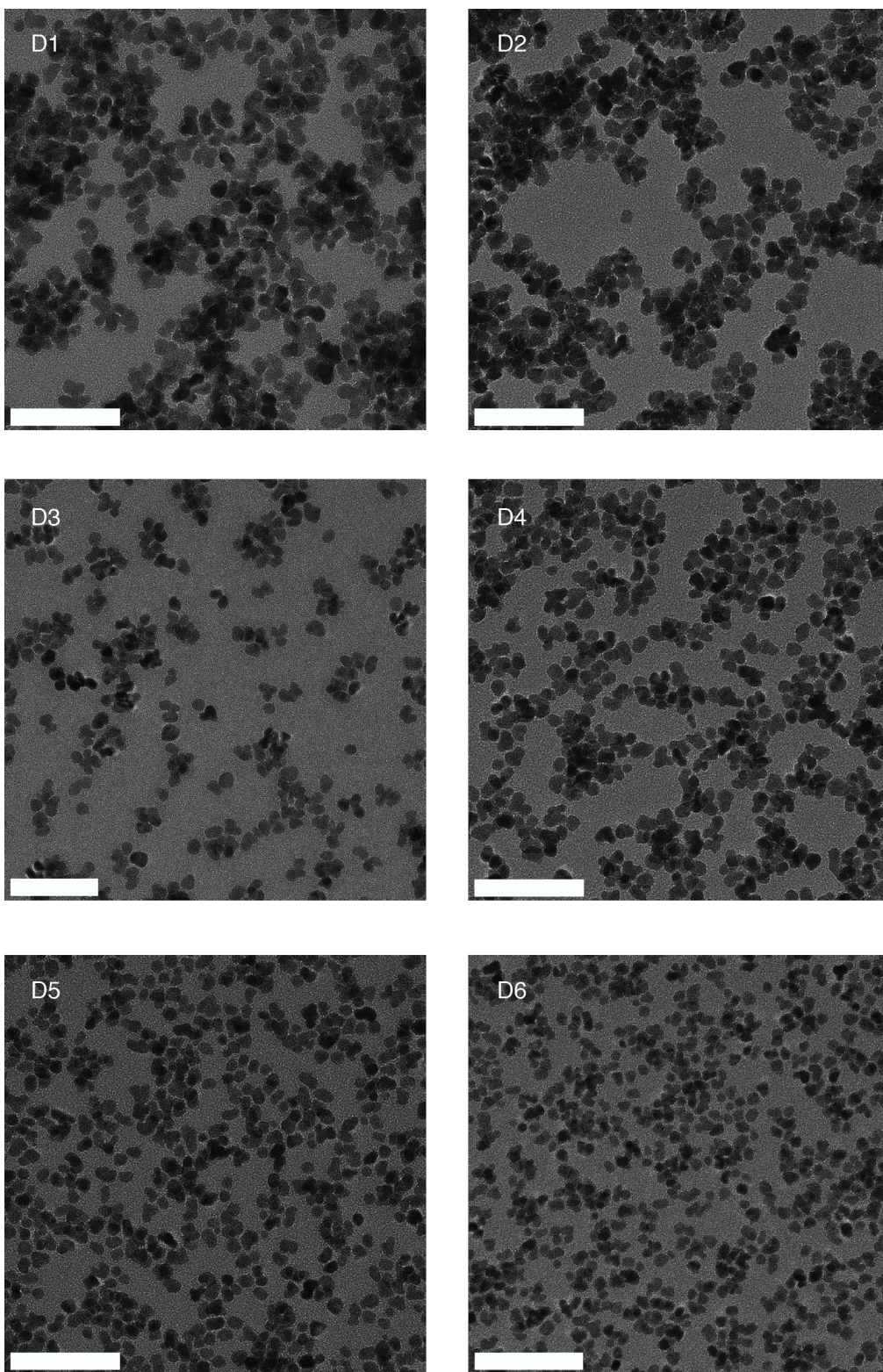
Figure A2.3. Transmission electron microscope images of nanocrystals in the doping series. Scale bars are 50 nm.
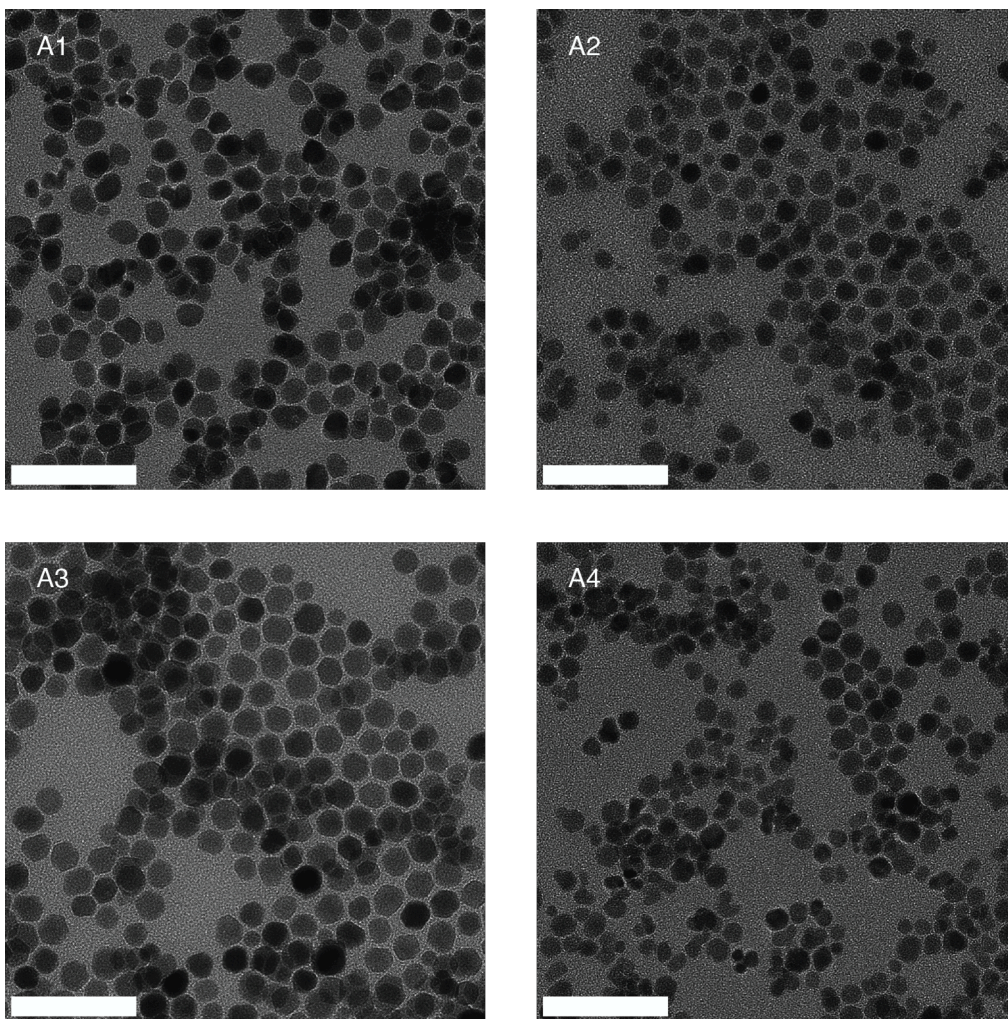
Figure A2.4. Transmission electron microscope images of nanocrystals in the activation series. Scale bars are 50 nm.

A2.3 **Additional** **XPS** **Analysis**

XPS measurements made at a photon energy of 920 eV showed behavior consistent with the trends relative to doping and activation reported in the main text but anomalous in terms of the photon energy dependent probe depth of the measurement (Figure A2.5). For the doping series, the surface tin content at 920 eV shows a similar linear trend below 6% doping, indicating a uniform dopant distribution, followed by an increase in the surface tin content above this value, indicating surface segregation (Figure A2.5a). However, above 5% doping, the

measured surface tin content at 920 eV is slightly higher than that measured at both 650 eV and 1150 eV. Similarly, for the activation series, the measured surface tin content at 920 eV is nearly identical to that for 650 eV. These results are seemingly inconsistent with the expected trend for a clean surface based on the probe-depths at each photon energy. Such a discrepancy could be due to the accumulation of a thin layer of adsorbates on the nanocrystal surfaces, which could cause Indium and Tin signal at 650 eV, the most surface-sensitive photon energy, to be effectively reduced. Further energy-dependent XPS depth profiling on these materials, including higher and lower photon energies than those used here, could provide insight into this anomaly.
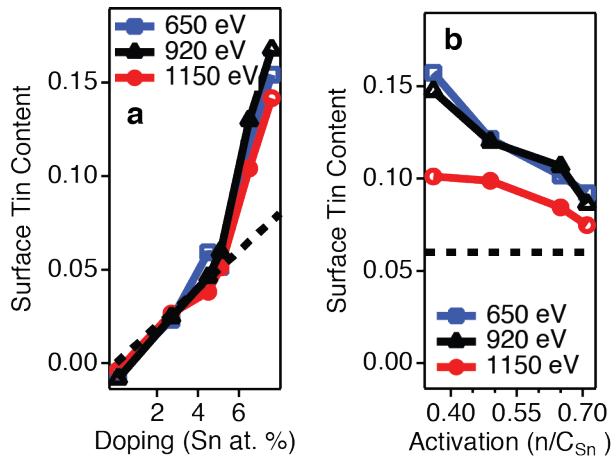

Figure A2.5. XPS depth profiling including 920 eV photon energy for (a) the doping series and (b) the activation series.

A2.4 Simple Drude Fitting

A simple Drude model with a fixed damping constant was used to fit optical extinction data for comparison to fits performed with an extended Drude model employing frequency-dependent damping constant. The simple Drude model was unable to reproduced high-quality fits for samples having a uniform doping profile (A2.6a). By contrast, the simple Drude model was able to reproduce high quality

fits with similar parameter values to the extended model for samples with surface segregated tin (Figure A2.6b and Table A2.1), indicating that ionized impurity scattering weak or negligible in these samples.
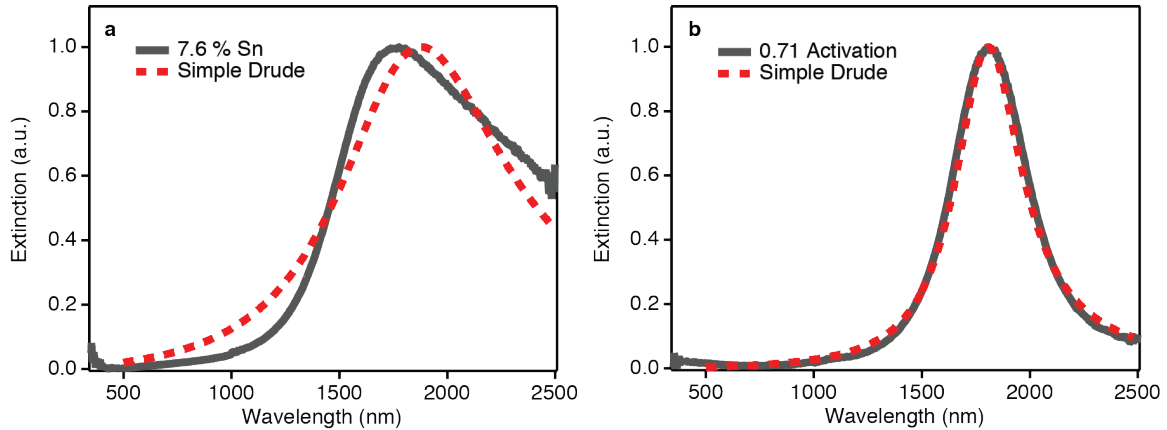

Figure A2.6. Simple Drude fitting of optical extinction spectra for (a) sample D6 and (b) sample A4.

Table A2.1. Comparison of simple and extended Drude fit parameters for sample A4. For the simple Drude model, $\Gamma = \Gamma_L$ in the table.

Fit model	ω_P (cm^{-1})	Γ_L (cm^{-1})	Γ_H (cm^{-1})	Γ_X (cm^{-1})
Simple Drude	16005	1165	N/A	N/A
Extended Drude	16017 ± 43.7	1029.9 ± 178.1	4432.2 ± 2714.5	16348 ± 3800

A2.5 Core-shell simulation

An extension of the Mie solution to Maxwell's equations was employed in order to simulate a nanocrystal with a heavily doped shell and an undoped core, with inner radius R_1 and outer radius R_2 (See Figure A2.7). Based on the work of Zhu, the following expression for the absorption cross section of a core-shell structure was used,

$$\sigma_{abs} = \frac{8\pi^2\sqrt{\varepsilon_3}R_2^3}{\lambda}Im\left(\frac{\varepsilon_2\varepsilon_a - \varepsilon_3\varepsilon_b}{\varepsilon_2\varepsilon_a + 2\varepsilon_3\varepsilon_b}\right)$$

where,

$$\varepsilon_a = \varepsilon_1(3 - 2P) + 2\varepsilon_2 P$$

$$\varepsilon_b = \varepsilon_1 P + \varepsilon_2(3 - P)$$

and ε_1 and ε_2 are the dielectric functions of the core and shell, respectively, and ε_3 is the dielectric constant of the surrounding medium. ε_1 was modeled using the simple Drude model, with a fixed damping parameter Γ. The damping parameter for the core was determined based on the literature values reported for the d.c. electron mobility of indium oxide. ε_2 was modeled using the extended Drude model with frequency-dependent damping using the same empirical expression as that reported in the main text.
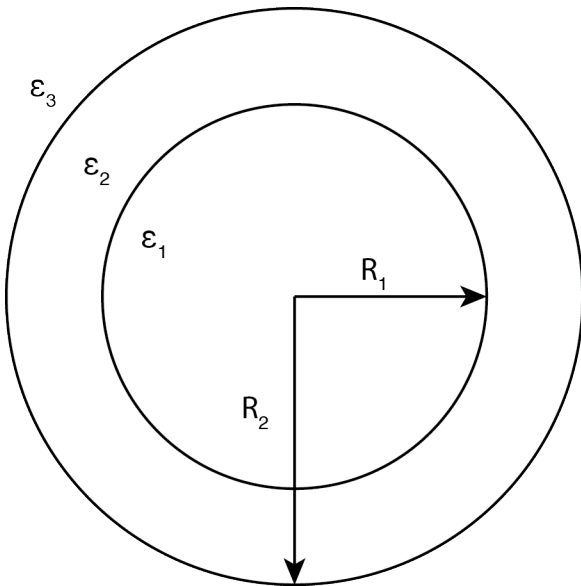

Figure A2.7. Geometry used for core-shell simulation

Actual values used for the simulation reflected those of the real samples from in the main text. The free electron concentration, n, was assumed to be

constant throughout the volume of the entire structure. In order to account for the increased density of dopant ions in the shell for a given average doping level, the low-frequency damping constant was scaled by the fraction of the total volume subsumed by the shell.